

Arraying of single cells for high throughput elemental analysis using LA-ICP-MS

Dissertation
zur Erlangung des akademischen Grades
doctor rerum naturalium
Dr. rer. nat.
im Fach Chemie

eingereicht an der
Mathematisch-Naturwissenschaftliche Fakultät
der Humboldt-Universität zu Berlin

von
M.Sc. Konrad Löhr

Präsidentin: Prof. Dr.-Ing. Dr. Sabine Kunst

Dekan: Prof. Dr. Elmar Kulke

Gutachter: 1. Prof. Ulrich Panne
 2. Prof. Michael Linscheid

Tag der mündlichen Prüfung: 19.09.2019

Die experimentellen Arbeiten in dieser Promotion wurden von Oktober 2014 bis Juni 2019 als kooperatives Projekt an der Bundesanstalt für Materialforschung und -prüfung (BAM), der ETH Zürich und der HU Berlin im Rahmen der Graduiertenschule School of Analytical Sciences Adlershof (SALSA) angefertigt.

Reproduced in part from K. Löhr et al., *J. Anal. At. Spectrom.*, 2018, 33, 1579-1587 with permission from the Royal Society of Chemistry, and with permission from K. Löhr et al., *Anal. Chem.*, 2019, 91, 18, 11520-11528, Copyright American Chemical Society.

Zusammenfassung

Die induktiv gekoppelte Plasma-Massenspektrometrie (ICP-MS) kann aufgrund ihrer hohen Empfindlichkeit, ihres großen linearen Messbereichs und ihrer Multielementfähigkeit für die Einzelzellanalyse eingesetzt werden. Es gibt zwei Möglichkeiten, einzelne Zellen in den ICP einzuführen, entweder durch pneumatische Zerstäubung von Zellsuspensionen oder durch Laserablation (LA) von auf einem Träger getrockneten Zellen. LA-ICP-MS ist vorteilhaft aufgrund seiner zellgrößenunabhängigen Transporteffizienz zum ICP, sowie aufgrund besserer Kalibrierungskonzepte. Eine weit verbreitete Verwendung von LA-ICP-MS in der Einzelzellanalyse wird jedoch durch deren geringen Durchsatz behindert. Daher wurde in dieser Arbeit der Durchsatz von Einzelzellen-LA-ICP-MS untersucht und verbessert.

Die Zwei möglichen Ablationsmodi, die Bildgebung von Zellen mit subzellulärer Auflösung und die Einzelpunktanalyse (Single Spot Analysis, SSA) von einzelnen Zellen mit einem großen Laserspot werden hinsichtlich ihrer analytischen Gütezahlen (Signal-Rausch-Verhältnis, Präzision, Genauigkeit, Durchsatz) sowie hinsichtlich Bedienungsfreundlichkeit und Effizienz der Datenauswertung verglichen. Hierfür wurden adhärente 3T3-Fibroblastenzellen mit zwei Metallfarbstoffen (mDOTA-Ho, Ir-DNA-Interkalator) angefärbt und mit beiden Modi mehrere Dutzend Zellen vermessen. SSA zeigte einen besseren Durchsatz und bessere Nachweisgrenzen. Außerdem wurde gezeigt, dass > 400 Zellen analysiert werden müssen, um eine zufriedenstellende Statistik für einen quantitativen Vergleich zu erhalten. LA-ICP-MS wurde als zu aufwendig für die Analyse einer derart großen Zellzahl befunden. Daher wurde ein Arraying-Schritt zur Probenvorbereitung integriert, um eine automatisierte LA-ICP-MS-Analyse zu ermöglichen. Zunächst wurde das Arraying mittels hydrodynamischer Fallen mittels eines mikrofluidischen Chips getestet. Leider verhinderte der Chipbetrieb unter Druck in einer Klemmvorrichtung ein erfolgreiches Arraying, so dass eine größere Überarbeitung des Chipdesigns notwendig gewesen wäre. Außerdem wurde eine neuartige Technologie getestet, die sich auf piezoakustisches Mikrotröpfchen-Arraying in Verbindung mit der Bilderkennung von Zellen stützt, und es wurde ein guter Arrayingdurchsatz (550 Zellen h⁻¹) und eine beispiellose Einzelzellengenauigkeit (> 99%) erreicht. In einem Proof-of-Principle-Experiment wurde ein Zellarray von THP-1-Suspensionszellen mittels LA-ICP-TOF-MS analysiert und erstmals gleichzeitig endogene und exogene Isotope einzelner Zellen als Isotopen-Fingerabdrücke mit Nachweisgrenzen von nur wenigen hundert Attogramm gemessen. Abschließend wurden diese Ergebnisse mit dem derzeit gebräuchlichsten Ansatz zur Single-Cell (sc) -ICP-MS verglichen.

Abstract

Inductively coupled plasma mass spectrometry (ICP-MS) is increasingly used for single-cell analysis due to its high sensitivity, wide linear dynamic range, and multielement capabilities. There are two ways to introduce single cells into the ICP, either by pneumatic nebulization of cell suspensions, or by laser ablation (LA) of cells dried on a carrier slide. LA-ICP-MS is advantageous due to its cell-size independent transport efficiency, as well as due to the existence of superior calibration concepts. However, a more widespread use of LA-ICP-MS in single cell analysis is hampered by its low throughput. Hence, in this work the throughput of single cell LA-ICP-MS was studied and improved.

First, the two possible ablation modes, i. e. imaging of cells at subcellular resolution, and single spot analysis (SSA) of single cells using a large laser spot are compared regarding their analytical figures of merit (signal to noise, precision, accuracy, throughput), as well as regarding ease of operation and data evaluation. For that, adherent 3T3 fibroblast cells were stained with two metal dyes (mDOTA-Ho, Ir-DNA-intercalator) and several dozen cells were measured using both modes. SSA showed superior characteristics regarding throughput and detection limits. Moreover, it was shown that >400 cells must be analyzed to reach satisfactory statistics for a quantitative comparison of results and LA-ICP-MS was found to be too laborious for the analysis of such large numbers of cells. Thus, it was decided to integrate a single cell arraying step to enable automated LA-ICP-MS analysis. Two different arraying methods were evaluated: First, arraying via hydrodynamic front trapping of cells using a microfluidic device was tested. Unfortunately, chip operation under pressure in a clamping device prevented successful arraying, such that a major revision of the chip design would have been necessary. Secondly, and a novel technology relying on a piezo acoustic microdroplet arrayer in conjunction with image recognition of cells was tested and a moderate arraying throughput (550 cells h⁻¹) and an unprecedented single-cell accuracy (>99%) was found. In a proof of principle experiment, a cell array of THP-1 suspension cells was analyzed using LA-ICP-TOF-MS and endogenic and exogenic isotopes of individual cells were detected for the first time simultaneously as isotopic fingerprints of cells with detection limits as low as hundred attogram. Finally, these results were compared to the currently more commonly used analysis method single-cell (sc)-ICP-MS.

Table of Contents

Zusammenfassung	III
Abstract	IV
Table of Contents	V
List of Abbreviations	VII
1. Introduction	1
2. Fundamentals	3
2.1 Inductively Coupled Plasma Mass Spectrometry (ICP-MS) for cell analysis	3
2.1.1 Conventional ICP-MS analysis of liquid samples	4
2.1.2 Analysis of single cells using ICP-MS	4
2.2 Single-cell arraying technologies	12
2.2.1 Microfluidic arraying via hydrodynamic front trapping of cells	13
2.2.2 Piezo-acoustic droplet arraying in conjunction with image recognition of cells	15
3. Scope of work	16
4. Experimental	18
4.1 Comparison of LA-ICP-MS imaging and single spot analysis of single cells	18
4.1.1 Cell culture	18
4.1.2 Staining with Ir-DNA-intercalator and mDOTA-Ho	18
4.1.3 Calibration using standards arrayed on nitrocellulose membrane	18
4.1.4 LA-ICP-MS operation	19
4.1.5 Digestion of cell samples for liquid ICP-MS	25
4.2 Hydrodynamic front trapping of cells in microchambers	26
4.3 Establishing sc-ICP-MS and testing of cell tagging protocols	27
4.3.1 Cell Culture	27
4.3.2 Cell tagging	28
4.3.3 sc-ICP-MS	28
4.3.4 MALDI-TOF-MS to control complexing behavior of mDOTA and Ho	29
4.4 High throughput LA-ICP-TOF-MS and isotopic fingerprinting	29
4.4.1 Arraying of calibration standards	29
4.4.2 Arraying of single cells and beads	30
4.4.3 LA-ICP-TOF-MS	30
5. Results and Discussion	32
5.1 Quantification of metals in single cells by LA-ICP-MS: Comparison of single spot analysis and imaging	32
5.1.1 Imaging analysis of single fibroblast (3T3) cells	32
5.1.2 Single Spot analysis	35

5.1.3	Comparison of different measurement modes	36
5.1.4	Quantification of LA-ICP-MS measurements and validation via liquid ICP-MS after digestion	39
5.1.5	Conclusion	41
5.2	Single-cell arraying for automated LA-ICP-MS	43
5.2.1	Microfluidic single-cell arraying	45
5.2.2	Piezo acoustic single-cell arraying approach in conjunction with image recognition of cells	57
5.3	Establishing sc-ICP-MS methods and testing of cell tagging protocols	64
5.3.1	A sample introduction system with high transport efficiency for sc-ICP-MS	67
5.3.2	Testing of cell tagging protocols	73
5.3.3	Conclusion	77
5.4	High throughput Laser Ablation ICP-TOF-MS and isotopic fingerprinting	78
5.4.1	Single-cell arraying	78
5.4.2	LA-ICP-TOF-MS measurement	79
5.4.3	Blank correction	80
5.4.4	Quantification of cell dyes	81
5.4.5	Detection of endogenous isotopes in single cells	83
5.4.6	Correlation of isotope intensities	85
5.4.7	Conclusion	87
5.5	Comparison of LA-ICP-TOF-MS and sc-ICP-SF-MS	89
6.	Summary and Outlook	92
7.	Appendix	94
7.1	Comparison of different LA modes: single-element measurements	94
7.2	Establishing of sc-ICP-MS using the HECIS	98
7.2.1	sc-ICP-MS using HECIS standard operation procedure	98
7.2.2	sc-ICP-MS data acquisition	99
7.3	High throughput Laser Ablation ICP-TOF-MS and isotopic fingerprinting	101
7.3.1	Background correction	102
7.3.2	Quantification of cell dyes	107
	Acknowledgements	118
	Selbstständigkeitserklärung	108
	Literature	108

List of Abbreviations

ARIS	aerosol rapid introduction system
BAM	Bundesanstalt für Materialforschung und -prüfung
cAMP	cyclic adenosine monophosphate
CD	cluster of differentiation
cps	counts per second
DMEM	Dulbecco's modified eagle medium
DOTA	tetraazacyclododecane-tetraacetic acid
ELISA	enzyme linked immuno sorbent assay
ETH	Eidgenössische Technische Hochschule
FBS	fetal bovine serum
G6PDH	glucose-6-phosphate dehydrogenase
HECIS	high-efficiency cell introduction system
HEPES	Hydroxyethyl-piperaziny-ethansulfonsäure
ICE	image composite editor (Microsoft)
ICP-MS	Inductively coupled plasma mass spectrometry
LA	laser ablation
Ln	lanthanide
LOD	limit of detection
LOQ	limit of quantification
MALDI	matrix assisted laser desorption / ionization
mDOTA	maleimido-mono-amide-DOTA
PBS	phosphate buffered saline
PDC	piezo dispense capillary
PDMS	polydimethylsiloxane
PFA	paraformaldehyde
PMMA	Polymethylmethacrylat
Q	quadrupole
rcf	relative centrifugal force
RSD	relative standard deviation
RT	room temperature
sc	single cell

SD	standard deviation
SEM	standard error of the mean
SF	sector field
sp	single particle
SSA	single spot analysis
TOF	time of flight

1. Introduction

Cells are the basic unit of all living organisms and are often called “the building blocks of life”. It is not surprising that the study of cells is one of the central topics in the life sciences. Ensemble analysis of cells and their constituents can already help to answer many important questions, but there are as well many cases where only the study of each individual cell provides crucial information. The quantitative study of single cells, also called cytometry, plays an essential role in medical sciences and diagnostics. For example, every complete blood count encompasses a measurement of white and red blood cell concentration, which is used as indicator for health and disease. Historically this test had to be performed manually by counting the number of cells in a specific volume under a microscope, using a hemocytometer as counting chamber. Nowadays, technological advances have reduced the manual work to perform such a cell count significantly. The first automated device became available in the 1950s with the commercial introduction of the coulter counter, which relied on electrical impedance measurement to determine cell count and size. Measurement devices for single-cell analysis are commonly known under the term *flow cytometer*. In flow cytometry, a flow of cells through a detector is used to generate a time-dependent signal of a specific parameter. Today, most flow cytometer instruments rely on optical measurements. Optical measurements enable fast and inexpensive access to a wide range of cell parameters. Cells passing through a light beam scatter light, which is exploited in cytometry: while forward scattered light can be used to count and size cells, side scattered light can be used to gain information about structural complexity of cells. Despite similar optical appearance and same genetic information, cells have a huge variety of phenotypes, which is reflected by expressed proteins. Gaining quantitative information about the cellular proteome on a single-cell level is a quite challenging task, considering the low copy numbers of proteins (10^0 to 10^6 per cell).¹ By the introduction of fluorescence-based flow cytometry in the 1960s, a whole new range of information became accessible bit by bit. Fluorochrome labeled binding reagents (e.g. antibodies) enable the quantitative determination of biomarkers with copy numbers as low as 10^2 per cell.² Quantitative information about cellular biomarkers can be used e.g. for cell type classification in basic research, but has as well found numerous applications in clinical diagnostics, e.g. it is most commonly indicated for hematologic cancers.³ Classification of cells is a multidimensional problem. As an example, the different cell classes of the immune system possess 371 different surface proteins. For immunophenotyping (i.e. classification of immune system cells), usually multiple of these surface proteins of the so-called cluster of differentiation

family (CD) need to be measured for each cell. Simultaneous measurement of different fluorescent tags can only be achieved for about 10 different fluorescent tags because of their spectral overlap.⁴ This is not sufficient to reveal the whole complexity of cell types. To enable the study of more than 10 biomarkers at once, a suitable detector was found in inductively coupled plasma mass spectrometry (ICP-MS), where the usually fluorochrome labeled binding reagents are replaced with metal isotope labeled binding reagents.^{5, 6} ICP-MS is the gold standard in inorganic elemental trace analysis and became popular for biological and biochemical applications due to its multi-element coverage and high sensitivity which is a prerequisite for the detection of metals in single cells.^{7, 8} Accordingly, ICP-MS can be used for the analysis of endogenous elements of the cell. The endogenous elemental content of a cell is also referred to as the cellular metallome.⁹ “Metallomics” is a relatively new scientific field which was proposed by Haraguchi in 2004 in order to integrate all research fields related to biometals and complement the -omics field of biological sciences (genomics, proteomics, ...).⁶ Moreover, Haraguchi formulated the challenge of an all-elements analysis of one biological cell in order to obtain metal-fingerprints for the biological species, similar to genetic codes in genes and the amino acids sequence in proteins.⁹ Metal-fingerprint information was considered useful for e.g. medical diagnosis of health and disease. Moreover, single-cell ICP-MS is a promising tool for in vitro (nano-) toxicity studies, drug testing and cancer research. Because of this great interest in single-cell analysis by ICP-MS, significant research was already carried out over the past decade which was recently reviewed.^{7, 8} The two major techniques used to introduce single cells into the ICP are either direct introduction of complete single cells, or a laser is used to ablate cells to form a fine aerosol which is then transported into the ICP. While significant technological progress has been made within the past decade regarding single-cell sample introduction into the ICP and the MS detection techniques, there are still great challenges ahead. The advantages of laser ablation (LA) as sample introduction method are opposed by its low throughput which was considered as the major bottleneck preventing more widespread use. Moreover, the all-elements analysis of a single cell is still an open challenge. It is the goal of this work to increase the throughput of LA-ICP-MS based single-cell analysis. For that, first, the two possibilities to analyze single cells using LA-ICP-MS, imaging¹⁰ and single spot analysis,¹¹ need to be compared. Secondly, to overcome the tedious manual targeting of single cells, an additional sample preparation step to array single cells to enable automated high throughput analysis is considered as very promising. Finally, the elaborated technique should be applied to engage in the challenge of detecting isotopic fingerprints of single cells, i.e. the cellular metallome.

2. Fundamentals

2.1 Inductively Coupled Plasma Mass Spectrometry (ICP-MS) for cell analysis

Inductively coupled plasma mass spectrometry (ICP-MS) is often considered as the gold standard in elemental analysis for (ultra-) trace determination with various applications in industry and academia. Especially in the life sciences, this technique is used more and more.¹² Pioneered by Houk in the 1980s,¹³ its success can be explained by a wide linear dynamic working range of 8-12 orders of magnitude, low detection limits in the range of 0.1 to 1 pg g⁻¹, its multi-element capabilities and its ability to determine almost all elements of the periodic table.¹⁴ These characteristics make ICP-MS the measurement technique of choice for elemental analysis of single cells. For the different aspects of ICP-MS history, instrumentation and methodologies, excellent reviews and books exist.^{14, 15} Thus, after a brief introduction to conventional ICP-MS, this theoretical part is focused on the critical technical aspects for single-cell analysis using ICP-MS.

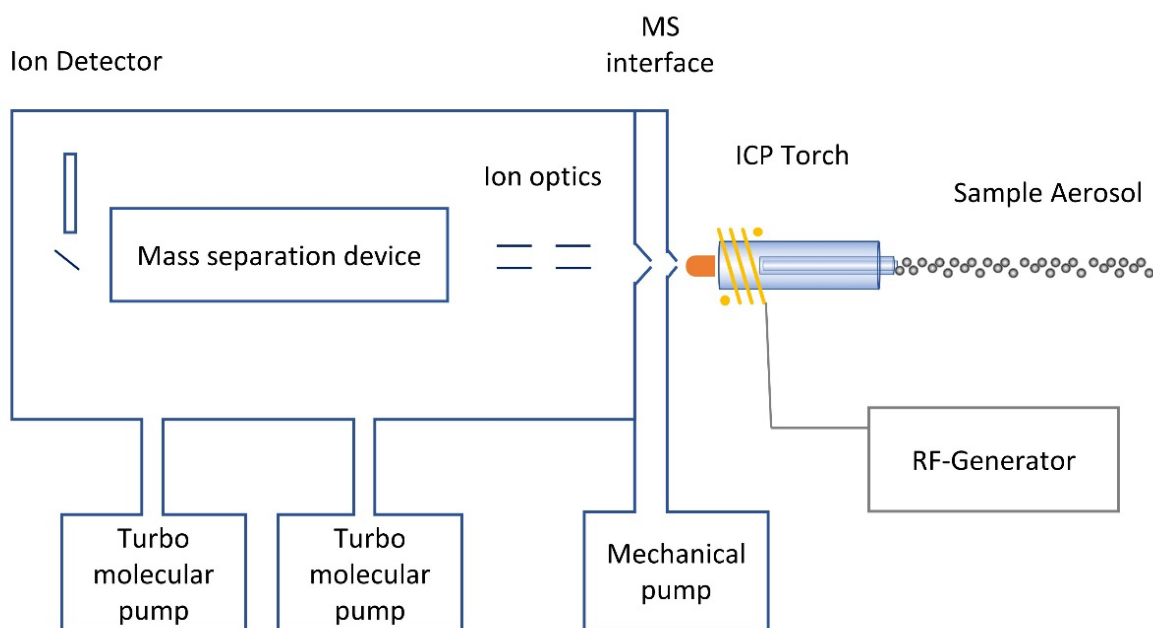


Figure 1 Basic components of an ICP-MS after Thomas *et al.*¹⁵

An overview of the basic components of an ICP-MS is shown in Figure 1. The sample is usually converted into a fine aerosol which is introduced into the ICP torch. The inductively coupled plasma is maintained by a steady argon and energy supply, whereby the energy is provided by the RF generator via a copper coil and consumed by the plasma via electromagnetic interaction.

After the aerosol enters the plasma, the sample is vaporized, atomized and finally ionized. The ions are directed via the MS interface and ion optics as a focused ion beam into the mass separation device. The mass separation device separates ions according to their mass-to-charge ratio and guides them to the detector. The detector converts arriving atoms quantitatively to a measurable current, which is typically translated into the commonly used unit counts per second (cps).

2.1.1 Conventional ICP-MS analysis of liquid samples

ICP-MS is usually used with liquid samples which are transformed into a fine aerosol using a nebulizer. This fine aerosol is sprayed into a spray chamber which is connected to the injector of the ICP torch. Spray chambers are usually designed to sort out bigger droplets ($d > 10\ \mu\text{m}$) due to their inertial force using single- or double-pass and cyclonic spray chambers. This is done for two reasons: first, because big droplets might be incompletely atomized and ionized within the plasma and secondly, big droplets result in a less precise signal. Only a small fraction of the total sample enters the plasma as a fine aerosol. Transport efficiencies of conventional systems are in the order of $\sim 1\%$.¹⁵ For more details on conventional sample introduction systems extensive reviews are available.^{16, 17} In conventional liquid ICP-MS, samples are digested using strong acids in order to dissolve all solids including the analyte. After dilution to lower acid contents (typically 1-2% nitric acid), these liquids can be measured by ICP-MS. The resulting signal intensity (typically given in counts per second, cps) can be quantified, most commonly an external calibration is used, i.e. comparing the sample analyte intensity to analyte intensities of calibration standards. ICP-MS analysis of liquid samples is most accurate and thus preferably used if enough analyte is available, e.g. for ensemble analysis of cells (typically $>10^6$ cells) to unravel mean analyte contents per cell.

2.1.2 Analysis of single cells using ICP-MS

The conventional analysis approach by digestion and liquid ICP-MS is not well suited for the analysis of individual single cells. Besides being very tedious, digestion of single cells and subsequent dilution of the analyte content would likely result in very low concentrations and measurement of aliquots thereof would be below the detection limit. Therefore, in single-cell analysis the analyte, i.e. the whole cell, is measured at once to obtain measurable intensities. This results in the measurement of a time-resolved peak for each cell, which must be integrated to obtain quantitative information. To lower detection limits, it is a convenient measure to reduce the peak duration. This can be done because the noise level used to calculate the

detection limit (standard deviation (SD) of the peak blank) is connected to its peak duration in case of normally distributed noise:

$$SD = \frac{SD_{indiv}}{\sqrt{n_{indiv}}} = SEM \quad (1)$$

with

SD_{indiv} = Standard deviation observed for individual measurement

n_{indiv} = Number of individual data points needed to integrate the transient signal

SEM = Standard error of the mean

Accordingly, as a rule of thumb, reducing peak duration by factor 10 lowers detection limits by 68%. The two major techniques used to analyze the whole amount of analyte in single cells by ICP-MS are either introduction of complete single cells into the ICP, or a laser is used to ablate cells to form a fine aerosol which is transported into the ICP. The strengths and drawbacks of both methods will be discussed in the following chapters.

2.1.2.1 Introduction of complete cells into the ICP-MS

If particles are introduced into the ICP this leads to a very short transient signal lasting 200 to 500 μ s. In case of very dilute particle suspensions, these particles enter the plasma statistically one by one and can be separated time resolved. The intensity of such a flash of ions is proportional to the analyte mass of the particle and the frequency is proportional to the concentration of the particles.^{18, 19} This analysis technique became especially important for studying nanometer-sized materials using conventional pneumatic nebulizers and the measurement methodology was coined as “single particle” (sp)-ICP-MS. This approach was extended to measure cells which are simply regarded as relatively large particles. The resulting measurement mode was coined as “single-cell” (sc)-ICP-MS.

To introduce complete cells into the plasma, the cells must be encapsulated within fine droplets and transported into the ICP. Most eukaryotic animal cells have a diameter of about 8-30 μ m and thus are eliminated in conventional spray chambers, as they are designed to sort out droplets with a diameter larger than ~ 10 μ m.¹⁴ Accordingly, the already relatively poor transport efficiency of $\sim 1\%$ usually decreases further, sometimes until no cells can be detected at all.

Already in 1994, the calcium content in single mammalian cells was studied, whereby a transport efficiency of about 0.1% was reached.²⁰ To improve the transport efficiency for single cells, different customized sample introduction systems were developed. The commercial CyTOF™ system (Fluidigm) uses a conventional pneumatic nebulizer and an especially designed on-axis low volume spray chamber which employs a heated make-up gas to evaporate solvent from produced droplets and increase the cell introduction efficiency to 20-30%.²¹ A high-efficiency cell introduction system (HECIS) was developed by Groombridge *et al.*²² and a transport efficiency of 100% was reached for microbes smaller 3 µm, which decreased to 86% for microbes with a diameter of 6.4 µm. However, for larger mammalian cells the transport efficiency was expected to decrease further according to their diameter. Recently, a total consumption nebulizer and spray chamber were used to introduce mammalian cells into the ICP with a transport efficiency of 25%, without the need for additional heating or make up gas.²³ Moreover, a commercial single-cell analysis kit was recently presented by PerkinElmer,²⁴ including a direct pass spray chamber which employs a make-up gas (Asperon™) with a transport efficiency up to 30%, whereby polystyrene particles served as a cell model which had a relatively small diameter ($d = 2.5 \mu\text{m}$) if compared to mammalian cells.²⁵

In addition, there are approaches where cells are encapsulated within microdroplets of uniform size. Such microdroplets were produced using either commercial microdroplet generators or microfluidic chips, whereby such techniques offer the advantage that they provide a readily available approach for quantification of cellular metal contents.^{26, 27} Shigeta *et al.* used a piezo acoustic micro-droplet dispenser in conjunction with a desolvation system to introduce single selenized yeast cells ($d = 3\text{-}5 \mu\text{m}$) into the ICP with a transport efficiency of 100%. However, so far this approach could not be transferred to larger cells. Microfluidic polydimethylsiloxane (PDMS)-based chips were used to encapsulate cells into aqueous droplets within an organic phase prior to analysis via time-resolved ICP-MS. Transport efficiencies of >50% for red blood cells (8 µm) were reached using a liquid-assisted droplet ejection chip and a custom-built transport system including a membrane desolvator for removal of the organic phase.²⁶ In a simpler approach a conventional nebulizer and spray chamber were used and transport efficiencies of ~2% were obtained.²⁸ Microfluidics-based approaches are especially attractive as in the future they could be combined with microfluidic sample pretreatment modules such as separation, dilution or cell sorting, etc.²⁶

The transport efficiency of intact single cells into the ICP is strongly cell size dependent,²² which is a disadvantage as this might lead to a non-representative sampling of smaller cells.

Furthermore, sc-ICP-MS so far focuses more on multiplex assays but calibration methods for quantification are not yet well established,²⁹ despite first promising results were achieved recently.^{23, 30} Quantitative analysis of cells is complicated by the fact that the degree of ionization in the ICP is dependent on cell size and larger cells might not be completely ionized.³¹

2.1.2.2 Laser Ablation for analysis of cells using ICP-MS

Laser Ablation (LA) for solid sample introduction is a technique which circumvents some of the shortcomings described in the previous chapter elegantly. LA-ICP-MS is more and more applied as a sample introduction technique in the life sciences, most importantly because it enables imaging of analyte distribution e.g. within tissue sections and single cells.³²⁻³⁴ A schematic representation of an LA system is shown in Figure 2. To perform an LA analysis of a solid sample, the sample is placed into the airtight ablation chamber¹ mounted on an x-y-z stage. Using a microscope with a CCD camera, the optics must be focused on the sample which subsequently can be explored to set an ablation pattern in the LA system software. During ablation, the focused laser beam interacts with the sample and in the resulting plasma of atoms, ions, and particles an aerosol is formed. The ablated sample aerosol is transported into the ICP using a steady flow of helium. Usually, an ablation cup is used to reduce the washout time of the large ablation chamber (this setup is coined as “two-volume ablation chamber”).

For LA, the transport efficiency of cells is not cell size dependent, because a fine aerosol is formed after ablation with particle diameters typically <200 nm.³⁵ Moreover, this aerosol is easier to ionize completely compared to whole cells and thus, quantitative work becomes possible.³¹ LA is prevalently used for imaging of cells and tissues. Spot sizes down to 4 µm are available in modern LA instruments,^{II} and spot sizes down to 1 µm and below were recently reached.³⁶⁻³⁹ By lowering the spot size, the time required for imaging a defined area increases quadratically while the signal intensity decreases proportionally. To reduce the analysis time and improve the signal to noise ratio, the washout time of ablation chambers was significantly improved.⁴⁰ However, the throughput of LA-imaging is too low to gain data for cytometry studies. A possibility to increase the throughput of LA cell analysis is the ablation of complete

¹ The more commonly used term ‘ablation cell’ will herein be replaced by ‘ablation chamber’ to prevent ambiguity.

^{II} NWR213, (2009, ESI); J100Series, (2010, Applied Spectra); GeoLasPro, (2008, Coherent); and LSX213 G2+ (Cetac) allow 4µm

cells using a large laser spot size in a mode coined as single spot analysis (SSA). SSA is useful if the distribution of elements on a single-cell basis is the main research question and presents a promising and readily available alternative to obtain statistically robust cytometry data for cells of any size in a moderate time frame. This approach has been recently used to track single gadolinium labeled CD4⁺ T cells,¹¹ to quantify nanoparticle uptake of single 264.7 cells,⁴¹ to quantify the gold nanoparticle labeled protein integrin on single HEL cells,⁴² and to quantify Cu in single algae cells.²⁹

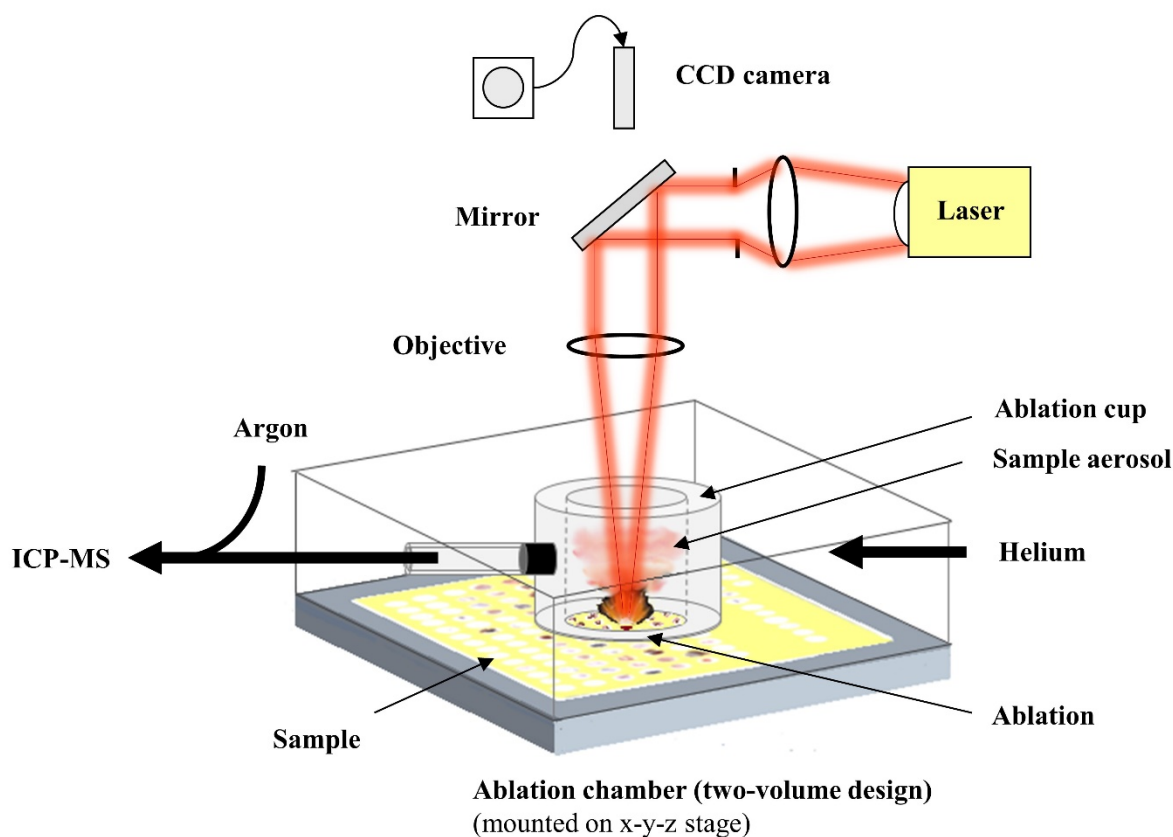


Figure 2 Laser Ablation sample introduction scheme. Figure courtesy of S. Hösl.

The commonly applied LA parameters differ between imaging and SSA of single cells. In case of imaging, the laser spot size is usually a trade-off between desired resolution, sensitivity, and analyte content, as well as the required analysis time. The laser irradiance (fluence^{III}) must be

^{III} Fluence is more commonly used in the LA community, despite irradiance could provide a more meaningful measure for the applied laser energy per surface.

selected carefully, such that several requirements are fulfilled: i) complete ablation of the sample, ii) no ablation of target substrate material to prevent additional background, iii) no translocation of neighboring sections by the laser plume or shock wave. For SSA, every cell must be completely included within the corresponding laser spot, whose size must be chosen accordingly. To be able to ablate a complete cell with only one laser pulse, the irradiance (fluence) is usually chosen considerably higher, although this is a tradeoff due to rising background signals from the substrate.

2.1.2.3 Mass analyzers, detector time resolution and multiplexing

The mass separation device separates ions according to their mass-to-charge ratio (m/z) and guides them to the detector. Depending on the type of mass separation device, ions of a specific m/z can be detected either sequentially (quadrupole and single collector instruments) or quasi-simultaneously (time-of-flight instruments, multicollector instruments) at instrument specific sampling frequencies. In single-cell analysis, transient signals of one or several elements of interest have to be evaluated.

In case complete cells are introduced into the plasma, transient signals have a length of only 200 to 500 μs . Such short signals prevent multiplexing for mass analyzers with sequential detection of different masses. Thus, only instruments with simultaneous data collection can be used for multiplexing. Moreover, the time resolution of the data acquisition is an important factor with implications for the possible throughput and detection limits. Conventional ICP-MS systems allow for integration times down to 1 to 5 ms, which prevents the resolution of transient signals from single cells or particles. Figure 3 depicts the four possible scenarios of several particles (a), exactly one particle (b), fractions of ion clouds from a particle (c, d) or no particle (e). Accordingly, wrongly chosen cell concentration and integration time may alter the obtained distribution of analyte content in the cell population. While a long integration time and high cell concentration may lead to an overestimation of cellular analyte content ((a) favored), short integration times may lead to an underestimation ((c, d) favored). Moreover, in case a long integration time is chosen, detection limits may increase significantly in presence of a background signal.

Newer generation ICP-MS systems allow for very short acquisition times as fast as 10^5 Hz. Using short integration times ($<50 \mu\text{s}$), transient signals of ion clouds from single particles can be completely resolved. Such systems enable analysis with the highest throughput and lowest

detection limits.⁴³ Most prominently, in mass cytometry up to 1,000 cells per second can be analyzed time-resolved using an ICP-TOF-MS detector which enables the analysis of all element masses >100 Da (>75 Da with the last instrument generation, HELIOS®).^{44, 45}

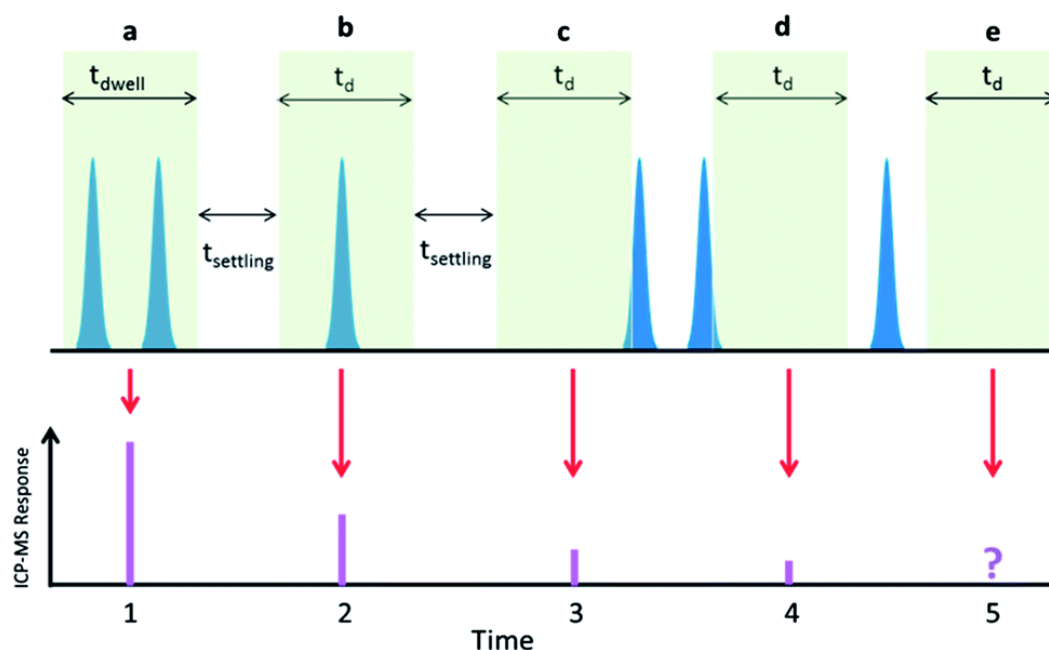


Figure 3 Effect of dwell and settling times on single particle measurements. (a) 2 particles detected (b) 1 single particle detected (c) the leading edge of 1 particle detected (d) the trailing edge of 1 particle detected (e) no particles detected. Reproduced from ref. ⁴³ with permission from the Royal Society of Chemistry.

In case LA is used for sample introduction, transient signals which originate from a single cell are significantly longer. A washout time of approximately one second was the standard for ablation chambers when this work was started,¹¹ technological progress during conduction of this work reduced washout times to about 10 to 100 ms, depending on the used laser spot size and LA unit.³⁶⁻³⁹ While washout times around one second enable multiplexing of several elements even on ICP-MS systems with sequential data acquisition,^{32, 46} shorter washout times in the range of 10 ms usually prevent multiplexing due to the mass analyzer settling times. Transient signals originating from single laser pulses (and the ablation of single cells) can be resolved with the predominantly used quadrupole and sector field mass analyzers, as well as with most TOF-MS devices. Table 1 gives an overview of reported figures of merit of ICP-MS devices with different mass analyzers. Devices which were used in the course of the preparation of this thesis are marked in bold.

Table 1 Comparison of reported ICP-MS figures of merit. Adapted from ref. ⁴⁷ with permission from the Royal Society of Chemistry.

	Quadrupole	Triple quadrupole	Single collector sector field	Multi-collector sector field	Mattauch Herzog	Time-of-flight		
Acronym	ICP-QMS	ICP-QqQMS	ICP-SFMS	MC-ICP-SFMS	MHMS	ICP-TOFMS		
Separation mechanism	DC/RF stability		Spatial separation based on m/z-dependent momentum			m/z-Dependent velocity		
Manufacturers	Agilent, PerkinElmer Sciex, Thermo Fisher Scientific , Analytik Jena	Agilent	Thermo Fisher Scientific , Nu Instruments	Thermo Fisher Scientific, Nu Instruments	SPECTRO	GBC Scientific Equipment	Fluidigm	TOFWERK (icpTOF)
Mass resolving power	Unit mass	Unit mass	300/4000/10000 (10% valley)	300/4000/10000 (10% valley)	400 (5% valley)	2000 (FWHM)	900 (FWHM)	2000–4000 (FWHM)
Collision/reaction cell	Yes	Yes	No	No	No	No	No	Yes
Simultaneous acquisition range	None	None	None	1–21 isotopes (max 15–20% around center mass)	5–240 m/z	1–260 m/z	75–209 m/z	14–275 m/z, 7–175 m/z
Full-spectrum acquisition time	100 ms	100 ms	150 ms	200 ms	20 ms	0.033 ms	N/A	0.030 ms
Time resolution	0.005–0.010 ms (1 isotope)	0.1 ms	0.0001–0.01 ms (1 isotope)	0.2 ms	20 ms	10 ms	0.013 ms	0.03 ms (burst mode), 1 ms (continuous acquisition)
Sensitivity (cps ppm ⁻¹)	10 ⁹	5 × 10 ⁸	10 ⁹	10 ⁹	10 ⁸ to 10 ⁹	2.5 × 10 ⁸	5 × 10 ⁸	6 × 10 ⁷
Abundance sensitivities	10 ⁻⁷ (high mass), 10 ⁻⁶ (low mass)	>10 ⁻¹⁰	3×10 ⁻⁵ (low R _m), 3×10 ⁻⁷ (medium R _m)	10 ⁻⁶ to 10 ⁻⁷ , 10 ⁻⁸ to 10 ⁻⁹ (Nu)	10 ⁻³ to 10 ⁻⁴	2.8 × 10 ⁻⁶ (low mass), 7.4 × 10 ⁻⁵ (high mass)	0.3% for 159Tb	6.5 × 10 ⁻⁴ (high mass)
LOD (pg g ⁻¹)	0.01	0.05	0.001	0.001	1	0.1–1	350 antibodies per cell	0.1–100
Linear dynamic range	10 ⁹	10 ⁹	10 ¹²	10 ⁹ to 10 ¹²	10 ⁸	10 ⁸	10 ^{4.5}	10 ⁶
Isotope ratio precision (RSD)	<0.1%	<0.2%	0.0005	0.00002	0.0004	0.0004	N/A	0.00023
Cost	\$	\$\$\$	\$\$\$\$	\$\$\$\$\$	\$\$\$	\$	\$\$\$	\$\$\$

2.2 Single-cell arraying technologies

Arraying of single cells has a history of more than one decade and multiple strategies for single-cell capture and isolation have been investigated.⁴⁸ A perfect single-cell arraying system for subsequent LA analysis should feature the following: a positioning accuracy better than the maximum laser spot size of conventional LA systems (~150 to 250 μm); cells must be accessible for LA, i.e. lie on a flat surface; high throughput; the capability of “true” single-cell deposition, preventing the need to double-check cell-number per spot; and arraying should be cell-size independent.

Many different approaches to array single cells on microfluidic platforms have been studied and successfully applied.⁴⁹ These approaches rely on different principles, like hydrodynamic cell traps using U-shaped or bypass-channel traps, electrical traps, optical traps, microwells, or trapping of cells using integrated valves. After arraying of cells, microfluidic chips must be removed since cell arrays must be presented on a flat surface. This typically leads to multiple problems, as the initial forces used for cell trapping change and removal of liquids may displace cells due to surface tension forces. To date, only few contributions report arrays produced for mass spectrometric analysis. Urban *et al.* used a microarray of hydrophilic spots on a hydrophobic plate and produced a cell array by wetting the complete surface with a cell suspension. On hydrophilic spots small droplets containing cells adhered, while the rest of the cells were removed. The number of cells per spot was approximately proportional to the cell concentration and followed a Poisson distribution.^{50, 51} Xie *et al.* used a microporous PDMS membrane as a pattern to produce an array of microwells where cells could adhere to a glass slide.⁵² Krismer *et al.* used a non-contact-spotter to array droplets containing cells.⁵³ Yang *et al.* used a surface printed microdot array where cells could adhere.⁵⁴ All these approaches used so far for single-cell arraying for mass spectrometry had no method to control the number of cells at array positions. Thus, a lot of events without single-cell information were analyzed and the actual cell number per spot had to be determined in an additional step. To the best of the author’s knowledge, there is only one study with an approach to control single-cell occupancy per spot: Huang *et al.* developed an approach similar to Xie *et al.*, but reduced the volume of PDMS wells, such that each spot could host only one cell. By centrifuging the cell suspension into the chip they managed to overcome two major disadvantages of the PDMS well method reported by Xie *et al.*: due to centrifugal force all wells were wetted with cell suspension and the well occupancy could be increased due to the fast sedimentation of cells. In this way produced cell

arrays had the highest single-cell occupancy reported to date (87%).⁵⁵ However, the relatively small PDMS wells might lead to the sampling of a subset of small cells and therefore this approach might not be representative for the whole cell population. In this thesis, two novel single-cell arraying techniques are tested as sample preparation method for subsequent analysis by LA-ICP-MS, which will be introduced in the following two chapters.

2.2.1 Microfluidic arraying via hydrodynamic front trapping of cells

Recently, Eyer *et al.* introduced a microfluidic chip for single-cell arraying and subsequent chemical analysis of intracellular biomolecules.⁵⁶ The arraying approach is based on hydrodynamic front trapping using microhurdles and the possibility to isolate each arrayed single cell within a microchamber. This approach enables the sequential exchange of solutions for incubation, washing and labeling steps. In a final step, cells can be lysed for the analysis of intracellular biomolecules within the very small volume of the microchamber. This approach was successfully applied for i) measuring the oxidative stress load (quantification of intracellular NAD(P)H), ii) measuring variations of glucose-6-phosphate dehydrogenase (G6PDH) levels, iii) cytotoxicity tests using suspension cells (U937).⁵⁶ Moreover, Eyer *et al.*⁵⁷ used this chip design for single cell ELISA, e.g. for the quantification of the enzyme GAPDH in suspension and adherent cells (U937, HEK 293) using sandwich ELISA, and to determine the concentration of the secondary messenger cyclic adenosine monophosphate (cAMP) in adherent cells (MLT) using competitive ELISA. Detection limits of intracellular biomolecules were found to be extraordinary low due to the very small volume of microchambers of only few hundred picoliters. Depending on whether suspension or adherent cells were used, different single-cell occupancies of microhurdles were obtained; while for suspension cells up to 75% single-cell occupancy was achieved, for adhesive cells only up to 27% was achieved, respectively. Figure 4 shows the design and operation of the microfluidic device for single-cell analysis. The microfluidic device consists of multilayered PDMS, comprising a control layer, a fluid layer, and a glass microscope cover slip. For manufacturing, first the control layer is bonded to the fluid layer, which then is bonded onto a microscope cover slip, see Figure 4 (a) and (b). To introduce and trap a cell inside the microhurdle feature and to deliver compounds to trapped cells, a cell suspension or compound solution is pumped through the fluid layer, see Figure 4 (c, left, fluid flow from left to right). The trapped cell can be isolated from the environment inside a microchamber by actuation of a ring-shaped valve, see Figure 4 (c, middle, gray colored). Microhurdles consist of two pillars which were shaped to accommodate a single cell. The closing of ring-shaped valves was realized by hydraulic pressurization of the

control layer, which leads to a displacement of the thin fluid layer ceiling in such way that it is pressed directly against the rigid bottom of fluid layer channels (a glass cover slip). Figure 4 (c, right) shows a micrograph of a trapped fluorescing cell surrounded by a non-fluorescing solution tightly encapsulated in a microchamber after actuation of the ring-shaped valve. The tightness of the microchamber was demonstrated by flushing the fluid layer with a fluorescing solution, which led to the high fluorescence intensity in the fluid layer channel outside the ring-shaped valve.

Recently, the approach was successfully adapted for analyzing smaller microbes *E. Coli*⁵⁸ and *Saccharomyces cerevisiae*, including successful on-chip cultivation of the latter microorganism.⁵⁹ Moreover, a detailed comprehensive overview about experimental methods, i.e. the fabrication of the microfluidic device, its operation, and its possible conduction of different experiments like single-cell ELISA is available.⁶⁰

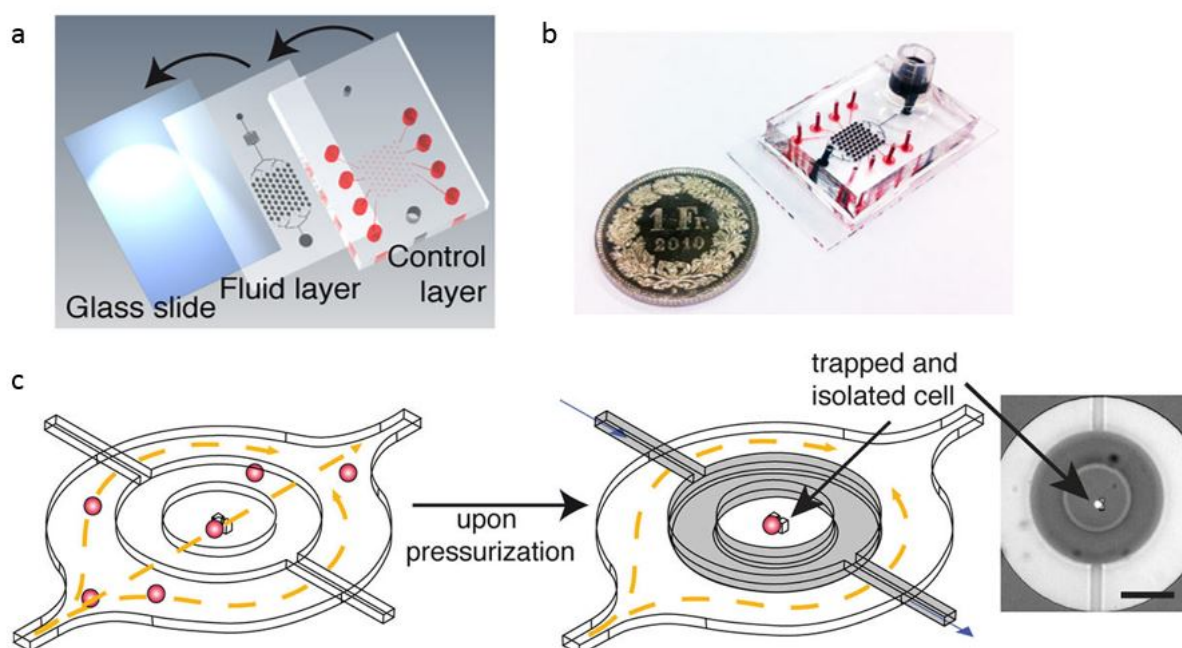


Figure 4 Design and operation of the microfluidic device for single-cell analysis. (a) Scheme of layers required for microchip fabrication. (b) Photograph of the device; the picture shows the fluid reservoir for the application of different reagents and fluid channels, both filled with black food dye, whereas pressure channels are filled with red food dye. (c) Scheme of a microhurdle and single-cell capture and isolation within a microchamber. On the right a single trapped fluorescing U937 cell can be seen inside a closed microchamber, whereas the remaining fluid layer liquid was exchanged with fluorescent solution (scale bare 150 μm). Adapted with permission from ⁵⁷. Copyright (2013) American Chemical Society.

2.2.2 Piezo-acoustic droplet arraying in conjunction with image recognition of cells

Another novel single-cell arraying approach was developed during the preparation of this thesis by cellenion, which will be evaluated as an alternative sample preparation method for automated LA-ICP-MS. The approach relies on a piezo-acoustic spotter (sciFLEXARRAYER S3 with sciDROP PICO, Scienion AG) and an automated software package for image recognition of cells within the piezo dispense capillary (PDC) prior to spotting (cellenONE®, cellenion SASU). After performing automated cell recognition in the PDC, an algorithm decides whether the next droplet will be dispensed onto the target array or discarded into the waste station (Figure 5). For that, the PDC is divided into travel, sedimentation and ejection zone. The ejection zone of the PDC corresponds to the volume which is ejected from the PDC with the next droplet. Accordingly, cell(s) located within the ejection zone will be ejected with the next droplet. The sedimentation zone is a “safety” zone, used to prevent additional cells from sedimenting into the ejection zone while the PDC is moving from the camera station to the arraying position. The travel zone is defined as the zone upward of the sedimentation zone. Figure 5 depicts four possible scenarios: A droplet containing a single cell will only be generated if exactly one cell is present in the ejection zone and no cell is in the sedimentation zone (A). In case of scenario (A), the PDC is moved by the axis system to the target position and a droplet containing a single cell is dispensed onto the target. After each single-cell dispensing, the PDC is repositioned by the axis system to the camera station and the process is repeated until every array position is filled with a single cell. In all other scenarios (B, C, and D), the next droplet will be discarded.

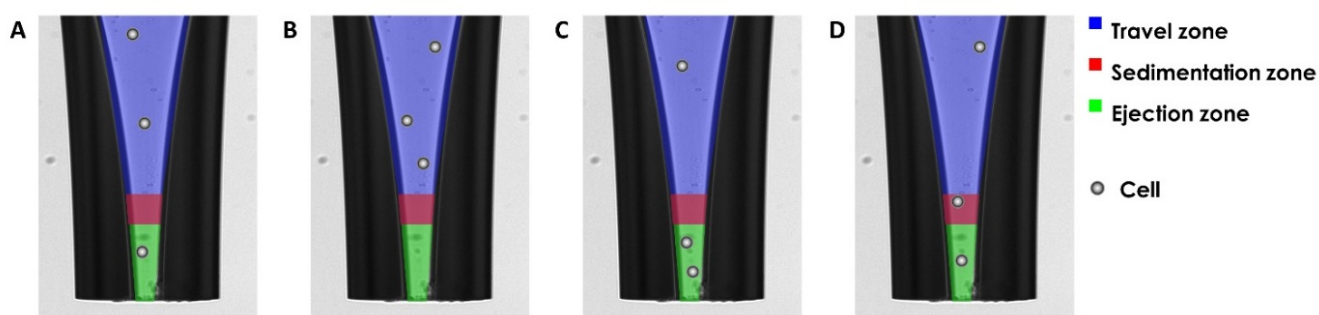


Figure 5 Scheme describing the three PDC zones and different possible scenarios of cells' positions in the PDC. (A) single-cell condition: a single cell present in the ejection zone and no cells in the sedimentation zone. (B) no cells are present in the ejection zone; (C) multiple cells are present in the ejection zone; (D) a single cell is present in the ejection zone but at least one cell is present in the sedimentation zone.

3. Scope of work

It is the aim of this thesis to increase the throughput of LA-ICP-MS analysis of single cells. To reach this goal, this thesis is divided into three parts: (1) comparison of approaches to analyze single cells using LA-ICP-MS, (2) testing of single-cell arraying approaches, (3) high throughput analysis of an array of single cells.

First, the two possible ways to analyze single cells using LA-ICP-MS, imaging and single spot analysis (SSA), are compared. Compared with the low throughput of imaging of single cells by line scans, the throughput can be conveniently increased by SSA. The analytical figures of merit for both LA operation modes have not been compared yet and are investigated in this work. Besides differences in throughput, differences in signal to noise ratio are expected, because in imaging mode a given absolute amount of analyte in a cell is represented by the total intensity divided by the number of pixels, while in SSA the total amount of a metal in a cell is represented by just a single intensity measurement. The sensitivities achieved in LA-ICP-MS depend on the matrix and the applied LA parameters.⁶¹⁻⁶³ Thus, for reliable quantification matrix matched standards are required, which have to be ablated using the same LA parameters as used for the sample.⁶⁴ Considering that laser spot size and irradiance differ significantly between standard imaging conditions and standard single spot analysis conditions, it is questionable whether both LA modes give comparable quantitative results. Moreover, the ICP-MS data acquisition parameters can influence the results as well. Multiplexing is one of the big advantages of ICP-MS, but can lead to a compromised measurement precision, if multiple elements are measured sequentially – as is common for the most widespread mass analyzers in ICP-MS, like quadrupole and sector field (SF) based instruments. Therefore, not only the differences between imaging and single spot analysis but also the influence of multi- and single-element data acquisition are evaluated. As a model sample, single 3T3 cells are grown on a glass slide and stained using a recently developed method involving two metal-conjugated dyes to identify and visualize single cells. Following the protocols developed in a previous study,⁶⁵ the complete cell is stained using maleimido-mono-amide-DOTA(holmium) (mDOTA-Ho), which binds to free thiol groups of e.g. proteins, and an Ir-DNA-intercalator to stain the corresponding cell nuclei. The aim of this first study is to compare the analytical figures of merit obtained for determination of dye metals in single cells using these two LA modes (imaging and SSA) measured with a sector field (SF-)ICP-MS, including the measurement accuracy after adequate calibration.

Secondly, the two promising approaches for single-cell arraying introduced in the theoretical part are tested for their suitability to increase the throughput of single-cell LA-ICP-MS. First, the microfluidic single-cell arraying approach is tested. The approach relies on hydrodynamic front trapping and was developed to analyze intracellular biomolecules in single cells. Secondly, the novel single-cell arraying technology relying on a piezo acoustic microdroplet arrayer in conjunction with image recognition is evaluated.

Finally, a single-cell array of THP-1 cells is produced using the microarrayer and analyzed using LA-ICP-MS with high throughput. For that, a protocol to tag THP-1 suspension cells with the two cell stains mDOTA-Ho and Ir-DNA-intercalator is developed and tested using sc-ICP-MS. Subsequently, these two cell stains are quantified using a recently introduced calibration approach which is suitable for high throughput analysis.⁴¹ Furthermore, the isotopic fingerprints of endogenous elements of a mammalian cell line are studied for the first time using a state-of-the-art ICP time-of-flight (TOF) MS.

4. Experimental

4.1 Comparison of LA-ICP-MS imaging and single spot analysis of single cells

4.1.1 Cell culture

Swiss albino mouse fibroblast cells (3T3, DSMZ) were cultured in Dulbecco's modified eagle medium (DMEM) supplemented with 10% fetal bovine serum (FBS Superior) (FBS and DMEM from Biochrom AG) and grown under standard conditions (37°C and 5% CO₂). For the experiments, the cells were grown for 24 h on sterile coverslips (Menzel Gläser GmbH, 20 x 20 mm) directly on 4-well Lab-Tek™ chamber slices (Thermo Fisher Scientific). The cells were washed three times with phosphate buffered saline (without calcium and magnesium (PBS w/o Ca/Mg, Biochrom AG) and immediately fixed with Histofix (Carl Roth GmbH). After fixation, the cells were washed again with PBS w/o Ca/Mg (three times). Fixated cells can be stored in buffer up to 2 months at 4 °C.

4.1.2 Staining with Ir-DNA-intercalator and mDOTA-Ho

Staining of cells was carried out according to recently optimized procedures.⁶⁵ The Ir-DNA intercalator stock solution (Maxpar® Intercalator-Ir 500 µM, Fluidigm) was diluted with PBS w/o Ca/Mg to an optimized concentration of 0.25 µM. Fixed 3T3 fibroblasts were incubated in the diluted Ir-intercalator for 45 min at room temperature. Before the next dying step, the cells were washed five times with 1 mL PBS w/o Ca/Mg. Maleimido-mono-amide-DOTA (mDOTA, CheMatech SAS) binds to free thiol groups, which are mainly present in proteins in the cell. Moreover, the DOTA moiety was used to chelate the lanthanide(III) isotope Holmium (Ho). Detailed information about loading of DOTA-chelate complexes with lanthanide ions is given elsewhere.⁶ Cells were incubated at a mDOTA-Ho concentration of 0.5 µM in PBS w/o Ca/Mg for 45 min at room temperature. Finally, cells were washed five times with PBS w/o Ca/Mg and dehydrated in a graded series of ethanol prior to LA-ICP-MS analysis.

4.1.3 Calibration using standards arrayed on nitrocellulose membrane

The metal content of cells was quantified in accordance with Drescher *et al.*¹⁰ by spotting of standards onto nitrocellulose (NC) membranes. For this purpose, a calibration series of a mixture of ICP-MS standard solutions (CertiPUR, Merck KGaA) containing holmium and iridium was prepared and diluted to concentrations of 0.05 mg L⁻¹, 0.1 mg L⁻¹, 0.5 mg L⁻¹, 1 mg L⁻¹, 5 mg L⁻¹, and 10 mg L⁻¹ for each element. In deviation from the work of Drescher, the

dilution series was spotted with a microarrayer system onto a nitrocellulose coated glass slide (ONCYTE® SuperNova, thickness <20 µm, GRACE bio-labs). As microarrayer system, the Bio Odyssey Calligrapher Mini Arrayer (Bio-Rad Laboratories Inc.) equipped with a solid pin with a spot square side of 75 µm (type 946NS3, Arrayit corporation) was used. For calibration, the printed membrane with the calibration series was ablated in imaging mode, because the dried spots of the spotted calibration series had a size of ~300 µm, which exceeds the largest laser spot size available (250 µm for the herein used NWR213 (ESI)). For ablation, the exact same LA-ICP-MS settings as used for imaging of cells were used, see chapter 4.1.4. The nitrocellulose layer was ablated completely, as was confirmed by ablating at several positions again and by visual inspection, whereas no visible traces of the nitrocellulose layer could be found. Finally, for each used concentration the integrated signals of two replica were averaged before the calibration function was fitted.

4.1.3.1 Validation of the arrayer system

Validation of the arrayer system was performed in collaboration with S. Techritz and Dr. L. Müller by dissolving flexible membranes (Whatman) with spotted calibration standards and subsequent quantification using liquid ICP-MS. For determination of the delivered volume, a nitrocellulose membrane was printed with 10 grids, consisting of 4 x 4 spots each. These grids were cut out, the membrane pieces were dissolved in concentrated HNO₃, diluted with water (purified to 18.2 MΩ using a Millipore Milli-Q water system) and measured against a standard calibration series with an ICP-SF-MS (Element XR, Thermo Fisher Scientific). The reproducibility of the spotting process was verified by measurements on different days and the delivered volume of the pin was determined to 0.61 nL ± 0.14 nL. Furthermore, the relative spot-to-spot standard derivation was determined to be less than 10% by LA-ICP-MS.

4.1.4 LA-ICP-MS operation

Investigations were carried out using the LA system NWR213 equipped with a two-volume ablation chamber (ESI) coupled to an ICP-SF-MS (Element XR, Thermo Fisher Scientific). The ICP-MS was synchronized with the LA system using the LA system in external trigger mode.

4.1.4.1 Laser Ablation

LA conditions for imaging by line scans were optimized in advance to these measurements and as similar conditions as possible were applied for both LA modes, imaging and SSA, see Table 2. However, complete ablation of a single cell by a single laser pulse was not possible. Therefore, for the ablation of single cells using a single spot, ablation conditions had to be optimized separately for this study: Even if a very high laser fluence of 10 J cm^{-2} was used, occasionally a little dark spot remained on the microscopic slide. Such dark spots remained predominantly in cases where the cell nucleus appeared large in bright field microscopy. Using a second pulse, the dark leftover could be ablated without leaving any visible traces, if the fluence was greater than 1 J cm^{-2} . However, to guarantee complete ablation in case of single spot analysis, three laser pulses with a fluence of 3.1 J cm^{-2} were used at the same location. For single spot analysis, each cell on the microscopic slide was selected manually, whereas for line scanning cell dense regions were selected. The aerosol produced in the LA system was transported to the ICP by helium at a flow rate of 1 L min^{-1} . Argon was added at a flow rate of 0.6 L min^{-1} in front of the ICP torch. The LA-ICP-MS was tuned for maximum intensity of ^{137}Ba and ^{232}Th as well as low oxide ratio ($(\text{ThO}/\text{Th}) < 3\%$) on a microscope glass slide by ablating line scans from the substrate material with a spot diameter of $200 \mu\text{m}$ and maximum laser energy at $10 \mu\text{m s}^{-1}$. All investigations were carried out on the same day within 9 hours using the same tuning conditions of the ICP-MS.

Table 2 Applied parameters for imaging and single spot analysis of single cells with the LA system NWR213 (ESI). The cell slides were placed on the sample holder and inserted into the two volume LA chamber.

	Imaging	Single spot analysis
Carrier gas flow rate:	$1 \text{ L min}^{-1} \text{ He}$	
Laser:	Nd:YAG	
Wavelength:	213 nm	
Laser fluence:	1.0 J cm^{-2}	3.1 J cm^{-2}
Repetition frequency:	10 Hz	20 Hz
Laser spot size:	$30 \mu\text{m}$	$110 \mu\text{m}$
Laser warm up	5 s	5 s
Ablation mode:	line scans ($25 \mu\text{m s}^{-1}$; $25 \mu\text{m offset}$)	single spot (burst count of three)

Two different ICP-MS scan lists were used to test the influence of multi-elemental analysis on quantitative results. First, a scan list previously optimized in our group was used, which would be typically applied in highly multiplexed imaging of immunochemically stained tissues or

single cells, see e.g. Müller *et al.*⁶⁶ In total, this list contained nine isotopes (¹⁵⁰Nd, ¹⁵³Eu, ¹⁵⁹Tb, ¹⁶²Dy, ¹⁶⁵Ho, ¹⁶⁹Tm, ¹⁷²Yb, ¹⁷⁵Lu, and ¹⁹³Ir), of which only two isotopes (¹⁶⁵Ho and ¹⁹³Ir) were used for data evaluation. Secondly, a singleplex scan list which contained only one isotope (¹⁹³Ir) was used, to see if the extended analysis has an impact on the measurement precision and imaging quality. The exact ICP-MS operating conditions and data acquisition parameters for both methods are explained in chapter 4.1.4.2 in detail.

The raw data of an LA-ICP-MS image comprises of a sequence of line scans. To visualize the raw data, for each element the line scans were transformed into a matrix (text image) using a customized MATLAB[®] program. This matrix was finally visualized using ORIGIN[®] to obtain an image with proper dimensions.

For quantitative determination, the signals of each single cell were integrated. In case of imaging, ImageJ (NIH) was used to select the area of each single cell by manually drawing a region of interest (ROI) around the cell and the “measure” tool was used to add up the intensity of all selected pixels. The average background intensity per pixel was determined in a similar fashion using an area without cells and subsequently, integrated intensities of single cells were background corrected. In case of single spot analysis, the signals of single cells were visualized as time-resolved plots. Each single cell was ablated by three laser pulses per spot at 20 Hz within 300 ms. The signals of the three pulses overlapped and formed only one peak, since the washout time of the ablation chamber for one pulse is >1 s. The resulting single peaks were integrated with manually set integration borders using Origin[®] integration gadget, while the total integration time was kept constant. Blanks were measured at spots without cells and subtracted from the integrated signals of cells.

4.1.4.2 Element XR operation and data acquisition

ICP-MS operating conditions are listed in Table 3 and data acquisition parameters for singleplex and multiplex measurements in Table 4, respectively.

To be able to measure an LA-ICP-MS signal in multiplex mode, one needs to sample the peak of a single laser shot with multiple elements. The used sector-field based ICP-MS system is not able to measure multiple elements simultaneously and is designed for the measurement of constant signals with a high precision. The manufacturer provides a preset measurement method for constant signals which takes 1.25 s for each measured isotope, see Table 4. That would be

longer than the transient signal of a single laser shot produced by the used LA platform (~1s). For the acquisition of transient signals, the instrument manufacturer provides an optimized method which only takes 0.1 s. To be able to measure multiple elements, this method was further optimized in our group based on Latkoczy *et al.*,⁶⁷ enabling the measurement of one element within 0.01 s. In the following, the relevant parameters will be introduced briefly along with the optimizations made:

Table 3 Operating conditions of the ICP-MS (Element XR, Thermo Fisher Scientific) for LA- coupling.

ICP-MS operating conditions	
Mass resolution	400
RF plasma source	1350 W
Plasma gas flow	16 L min ⁻¹ Ar
Auxiliary gas flow	1,1 L min ⁻¹ Ar
Sample gas flow	0,6 L min ⁻¹ Ar
Scan type	E Scan

The used Element XR has a reversed Nier-Johnson geometry of the mass analyzer and is usually operated in (electric-) E-Scan mode, because masses can be selected very fast by changing the acceleration voltage and electro static analyzer (ESA) voltage, while the magnetic field, which has a higher settling time, is left constant.⁶⁸ An E-Scan can resolve the mass peak of an isotope. Figure 6 shows the resolved mass peak of ¹⁵³Eu.

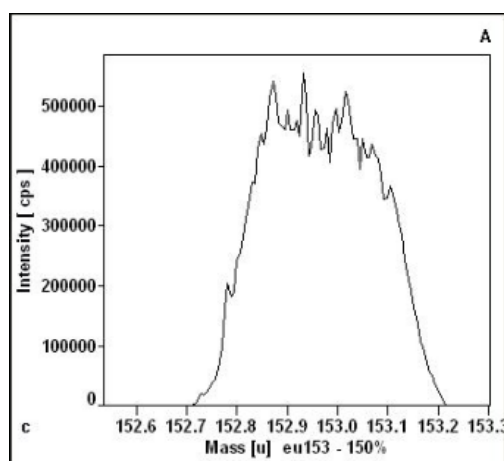


Figure 6 Resolved mass peak of ¹⁵³Eu in a mass window of 150% (screenshot from instrument tuning window).

Each isotope's mass peak has a specific width, which corresponds to a *mass window* of 100%. For the measurement of constant signals, such a mass peak would be typically resolved completely by using a mass window bigger than the mass peak (e.g. 125%, see Table 4). In this

way, it can be ensured that always the same fraction of the mass peak is used as *integration window* (e.g. the 60% in the center), even if the mass calibration is shifted a little bit. For the low-resolution mode, it is a reasonable assumption that the mass calibration is stable enough to skip the time intense peak searching because the mass peaks are broad and have a flat top. Hence, for transient signals the *peak search window* does not exist (0% of the mass window) and the integration window equals the mass window. To decrease the likelihood of sampling outside of the flat top of the mass peak, the mass window was narrowed from 20% to 5%, if compared to the preset Element XR method.

The *sample time* (= integration time at a specific mass) of 50 ms for constant signals is lowered considerably for transient signals to 10 ms for the preset method and 2 ms for the optimized method.

Another parameter affecting the analysis time is the number of *samples per peak*. This exact number will be sampled for a mass window of 100%; but if the mass window is different from 100%, the samples taken per peak change proportionally. To still sample the peak at multiple positions on the flat top, the samples per peak are increased from 20 for constant signals to 50 for the preset method of transient signals to 100 for the optimized method.

Using these parameters, the total time needed to measure one isotope (the so-called *segment duration*) can be calculated using the following equation:

$$\text{segment duration} = \text{mass window} \times \text{samples per peak} \times \text{sample time}$$

Table 4 Comparison of Element XR methods.

		Preset by Thermo Fisher Scientific		Customized for multiplexed LA-Imaging
		constant signal	transient signal	
Sample Time	/ s	0.050	0.010	0.002
Mass Window	/ %	125	20	5
Samples per Peak		20	50	100
Integration Window	/ %	60	20	5
Peak Search Window	/ %	60	0	0
Segment Duration	/ s	1.250	0.100	0.010

To measure at a specific mass, a specific mass close to the desired mass is selected by the magnetic field, the so-called *magnet mass*. The E-Scan mode is limited to a maximum mass range of $\pm 30\%$ around the magnet mass.

For the first seven isotopes of the multiplex measurement a magnet mass of 149.920 Da is selected automatically by the instrument and for the heaviest two isotopes a higher magnet mass of 174.940 is chosen, respectively. Usually, a minimum *settling time* of 1 ms is required between the measurement of two isotopes. Only if the magnet mass is changed, a higher settling time is needed. These settling times were optimized to low values of 100 ms for the jump from ^{193}Ir to ^{150}Nd and to 14 ms for the jump from ^{172}Yb to ^{175}Lu . The segment durations of the nine elements and their corresponding settling times add up to 211 ms to measure all isotopes, but their actual measurement takes an *acquisition time* of 220 ms. The overhead of 9 ms is needed for data treatment. This optimized acquisition time ensures that each peak of a single laser shot gets sampled multiple times (the typical washout time of a single LA pulse was ~ 1 s).

In case of singleplex measurements, the magnet mass is constantly set to 174.940 Da for the measurement of ^{193}Ir . Still, a minimal settling time of 1 ms is needed.

The sample time for singleplexing was increased ten times from 2 ms to 20 ms for two reasons. Firstly, the data treatment for one element takes 3 ms, what means that only during 10 ms out of 13 ms, the signal would be acquired (77% of the time). Secondly, since the data is acquired quasi-continuously, a high time resolution is not needed and data reduction by increasing the sampling time is advantageous. The acquisition time for singleplex measurements adds up to 103 ms, which is still a sufficient time resolution to resolve signals from individual laser pulses.

Table 5 Data acquisition method of the ICP-MS (Element XR, Thermo Fisher Scientific).

	Element	Settling Time ms	Magnet Mass Da	Mass Window	Samples Per Peak	Sample Time ms	Segment Duration ms	Acquisition Time ms
Single-element	¹⁹³ Ir	1	174.940	5%	100	20	100	103
Multi-element	¹⁵⁰ Nd	100	149.920	5%	100	2	10	220
	¹⁵³ Eu	1	149.920	5%	100	2	10	
	¹⁵⁹ Tb	1	149.920	5%	100	2	10	
	¹⁶² Dy	1	149.920	5%	100	2	10	
	¹⁶⁵ Ho	1	149.920	5%	100	2	10	
	¹⁶⁶ Er	1	149.920	5%	100	2	10	
	¹⁷² Yb	1	149.920	5%	100	2	10	
	¹⁷⁵ Lu	14	174.940	5%	100	2	10	
	¹⁹³ Ir	1	174.940	5%	100	2	10	

4.1.4.3 Data acquisition and processing timing

Depending on the number of runs (data points) acquired by the ICP-MS, time is needed for processing and saving. If the ICP-MS software is still processing data, no new data can be acquired if a trigger signal is received from the LA platform. Thus, usually a washout time of 5 s after each line is added on the LA platform, to prevent the omission of a complete line scan. For imaging of calibration standards very lengthy line scans (660 s) were performed, which required more time for data processing. Thus, an unusual lengthy washout time was used after each line scan (> 1 minute). Although all imaging line scans were recorded using the longer washout time for automation purposes, a washout time of 5 s was used for throughput calculations (multi-element 1625 μm x 1000 μm image of cells: laser warm up (5 s) + data acquisition (49 s; including 4 s gas blank) + 5 s washout time + 1 s relocation of LA-stage = 60 s per line scan; equaling ~25 min for the complete image).

4.1.5 Digestion of cell samples for liquid ICP-MS

For the control experiment, cells were grown in a 12-well plate for 24 hours. To determine the number of cells per well after 24 h, three replicate wells were trypsinized for 6 minutes at 37 °C, aliquots were stained with Trypan blue (Carl Roth GmbH) and a cell number per well of $60 \times 10^3 \pm 14 \times 10^3$ was determined using a C-chip (Biochrom AG, Berlin, Germany). The other wells were fixed and staining using Ir-intercalator and mDOTA-Ho was performed as described in section 4.1.2. Instead of an ethanol series prior to measurements, the cells were digested

using 800 µl Trypsin solution (Biochrom AG, Berlin, Germany) for 1 h at 37 °C. The samples were stored at -20 °C in Eppendorf-tubes until analysis.

4.2 Hydrodynamic front trapping of cells in microchambers

The whole process of production and usage of micro chamber array chips, as being applied in the Dittrich group (ETH Zürich), is already nicely described in a JoVE article.⁶⁰ Briefly, designs drawn in AutoCAD are first transferred to a photomask manufactured externally.^{IV} Subsequently, designs are transferred from the photomask to a wafer using photo-lithography techniques, while the height of structures can be controlled precisely via spin coating of the photo resist to a desired height. 20 µm channel height was selected for both layers as a compromise between small channel volumes and preventing the channels from collapsing.

Each chip has a two-layer design consisting of a so-called fluid layer and a pressure layer (control layer). The fluid layer wafer carries the negatives of channels and microhurdles for cell trapping (e.g. yeast or THP-1) and is spin coated with PDMS to a height of approximately 36 µm.^V The control layer wafer is used to cast control layers to a height of 0.5 mm PDMS. This thicker layer gives the assembled chip stability and consists of an array of donut shaped valves which is aligned onto the fluid layer, such that each donut-valve encapsulates a single-cell trap when actuated. Actuation of such a valve is performed via pressurization of the control layer to 2 to 3 bars. The donut valve channel is 80 µm wide and separated from the fluid layer only by a ~16 µm thin, elastic layer of PDMS, which is pushed down to the glass slide if pressurized. The design used for trapping of yeast cells is shown in Figure 7 (a-c); (d, and e) show the control layer design. To trap small yeast cells, microhurdles feature a small gap of only 3.5 µm between the two posts. For experiments conducted to trap THP-1 cells, a previously published chip design was used, with the main difference of microhurdles having a larger gap of 8 µm between the two posts.^{57, 60}

^{IV} Photomasks are the commonly used low-cost option (~100 € per wafer). Chrome masks offer a higher manufacturing precision (~1000 € per wafer).

^V According to studies performed in Sensors and Actuators A 151 (2009) 95–99, spin coating for 60 seconds at 2000 rpm results in such a layer thickness

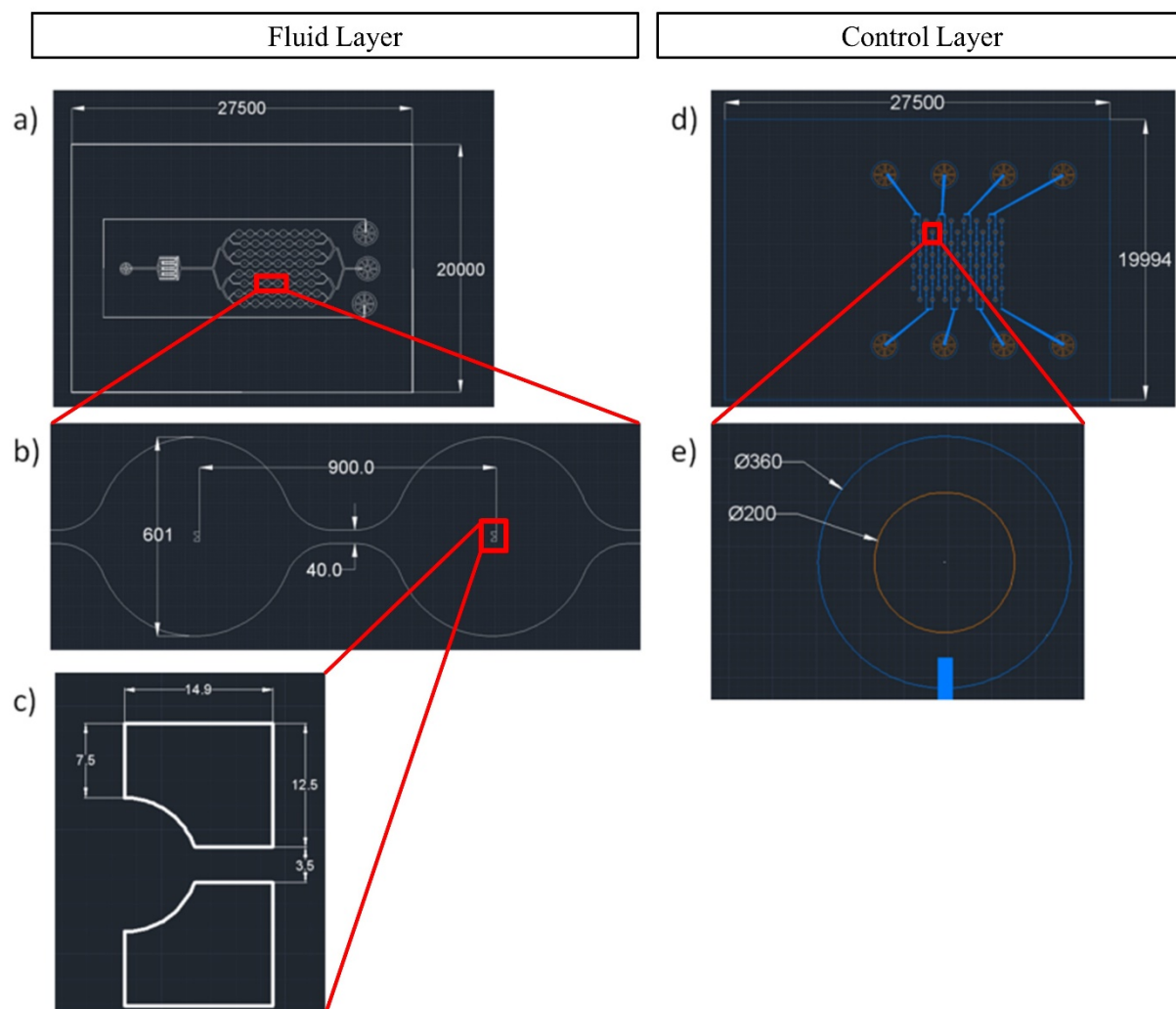


Figure 7 Screenshots of used two-layer chip design from AutoCAD®; all dimensioning in μm . a) Fluid layer: one chip is 27.5 mm x 20 mm in size. A four inch wafer carries five fluid layers. b) Zoom on two traps. c) Closeup of a single-cell trap for yeast cells (3.5 μm gap). d) Control layer: one chip is 27.5 mm x 20 mm in size. A four inch wafer carries ten control layers. e) Closeup of a single donut valve.

4.3 Establishing sc-ICP-MS and testing of cell tagging protocols

4.3.1 Cell Culture

Human monocytic leukemia cell line THP-1 (DSMZ type; a suspension cell line) was grown under standard conditions (37°C and 5% CO₂) in RPMI 1640 medium supplemented with 10% fetal bovine serum, 2 mM L-glutamine, 10 mM Hepes and 1 mM sodium pyruvate (all from Biochrom AG). Cells were passaged every 2 to 3 days to guarantee cell densities below 1×10^6 cells ml⁻¹ to prevent irreversible agglomeration. Prior to cell staining, cells were centrifuged at 300 rcf for 5 min, supernatant was aspirated, and the cells were fixed by resuspension in Roti-Histofix® 4% (Carl Roth GmbH). After cells were fixed for 15 min at room temperature, cells were centrifuged at 300 rcf for 5 min and supernatant was aspirated.

4.3.2 Cell tagging

Staining of cells was carried out following procedures recently optimized for adherent 3T3 cells,⁶⁵ adapted to the suspension cell line THP-1. The bifunctional molecule maleimido-mono-amide-DOTA (mDOTA, CheMatech) is able to chelate lanthanide(III) ions and to bind to free thiol groups, which are present in proteins of the cell. For loading mDOTA with Ho, mDOTA and HoCl₃ were weighed in as molar equivalents and incubated in 45 mM ammonium acetate (pH 6) for 30 min at 37°C. The resulting stock solution of 1.4 mM mDOTA-Ho was kept at 4°C until usage for up to 14 days. For tagging with mDOTA-Ho, fixed and pelleted THP-1 cells (4×10^6) were resuspended in PBS and mDOTA-Ho was added to a concentration of 250 nM. After incubating for 15 min, cells were washed twice with PBS. For tagging with Ir-DNA-intercalator, cells were resuspended in a 1:1 mixture of Roti-Histofix[®] and PBS and Ir-DNA-intercalator stock solution (Maxpar[®] Intercalator-Ir 125 µM, Fluidigm) was added to a concentration of 125 nM. After incubating for 60 min, cells were washed 3 times with PBS and right before further analysis 2 times with water (purified to 18.2 MΩ using a Millipore Milli-Q water system).

4.3.3 sc-ICP-MS

Two different systems were used to measure single cells based on the sp-ICP-MS mode. First, using the quadrupole ICP-MS iCAP Q (Thermo Fisher Scientific) equipped with a concentric PFA nebulizer and cyclonic spray chamber. The device was tuned following manufacturer's recommendations using Tune B solution (Thermo Fisher Scientific). The sulfur content in single cells was measured using oxygen as reaction gas to measure the oxygen adduct ⁴⁸SO after appropriate tuning using a 100 µg L⁻¹ sulfate solution (Thermo Fisher Scientific).

Secondly, a novel sample introduction system dedicated for single cell measurements using a CyTOF[®] device (Fluidigm) was used in combination with the sector field ICP-MS Element XR (Thermo Fisher Scientific). This system is a manually heated total consumption system and was operated with the data acquisition parameters shown in Table 6 after tuning using CyTOF[®] calibration beads (Fluidigm), see as well chapter 5.3.1 and appendix chapter 7.2 for details.

Table 6 Measurement parameters used for sp-ICP-MS measurements on Element XR (Thermo Fisher Scientific).

		sp-ICP-MS
Sample Time	/ s	0,010
Mass Window	/ %	60
Samples per Peak		1000
Integration Window	/ %	60
Peak Search Window	/ %	0
Segment Duration	/ s	6

4.3.4 MALDI-TOF-MS to control complexing behavior of mDOTA and Ho

Matrix-assisted laser desorption/ionization time-of-flight mass spectrometry (MALDI-TOF-MS) was performed on a Bruker Autoflex Smartbeam III MALDI mass spectrometer (Bruker Corporation), operated with a nitrogen laser and at 20 kV acceleration voltage. Mass spectra were calibrated using Standard Kit II (Bruker Corporation) according to manufacturer's recommendations. A mixture of 10 mg mL⁻¹ alpha-cyano-4-hydroxycinnamic acid in 70% acetonitrile (ACN) and 0.1% trifluoroacetic acid (TFA) served as matrix. 1 µL of sample was pipetted and mixed with 1 µL of matrix onto a stainless-steel target plate, which was then dried in air. Spectra were recorded in reflectron mode.

4.4 High throughput LA-ICP-TOF-MS and isotopic fingerprinting

4.4.1 Arraying of calibration standards

The metal content of single cells was quantified by calibration in accordance with Wang *et al.*⁴¹ Standard solutions were prepared in 1 wt% Rhodamine B ($\geq 95\%$, Sigma-Aldrich) in order to match the matrix of single cells and to allow visual recognition of the printed purple spots on the target glass slide (Superfrost plus, Thermo Fisher Scientific). To prepare the standards, a mixture of Ir-DNA-intercalator and mDOTA-Ho was diluted to 0 nM, 31 nM, 0.31 µM, 3.1 µM, and 31 µM in 1 wt% Rhodamine B and spotted using a sciFLEXARRAYER S3 with a PDC (PDC 70, coating type 3, Scienion AG). The volume of dispensed droplets was measured automatically using the gravimetrically calibrated image recognition software (sciDROP PICO, Scienion AG). The droplet volume was tuned manually daily to ~ 330 pL drop⁻¹ with a droplet-to-droplet volume variation (RSD) of $\leq 0.5\%$. In total, thirty calibration arrays, each comprising of ten replicates of each concentration, were initialized with a center-to-center spot distance of 500 µm and spotted using a fully automated arraying protocol.

4.4.2 Arraying of single cells and beads

Initially, an array of 10 fields with 10 x 10 positions and 500 μm center-to-center distances was defined on a target glass slide (Superfrost plus, Thermo Scientific) in the sciFLEX software. A volume of 20 μL of THP-1 cell suspension or bead suspension (15 μm , kisker biotech GmbH) was aspirated into the PDC (PDC70, coating type 3) with 2 $\mu\text{L s}^{-1}$. For each run a single array was prepared and the PDC was automatically emptied and washed.

4.4.3 LA-ICP-TOF-MS

All measurements were carried out using the Analyte G2 ArF Excimer LA system (193 nm, Teledyne CETAC Technologies) with aerosol rapid introduction system (ARIS) coupled to an ICP-TOF-MS (icpTOF, TOFWERK). For this system, washout times of ablated aerosol packages are spot size and material dependent. While spot sizes smaller than 10 μm ensure washout times in the order of ~ 30 ms, longer washout times of ~ 100 ms were observed with increasing spot sizes up to 150 μm . This largest available spot size was used to reliably ablate the entire dried droplet including a single cell. ICP-TOF-MS data was acquired continuously for the entire array with a time resolution of 30 ms (1000 averaged TOF extractions). MS acquisition start was synchronized manually with the ablation start. The LA-ICP-TOF-MS was tuned for maximum signal intensity of ^{23}Na , ^{59}Co , ^{115}In and ^{238}U , as well as low oxide ratio ((ThO/Th) $\sim 0.4\%$) using a NIST612 glass certified reference material. LA and ICP-TOF-MS operation conditions are summarized in Table 7. All measurements of single cells and calibration standards were carried out on the same day within about 30 min using the same tuning conditions. For automated single spot ablation of cells and standards a grid of spots was used as mask. Cells were ablated with 10 subsequent laser pulses per printed single spot ($d=150$ μm) with 100 Hz repetition rate and a fluence of 0.36 J cm^{-2} . Standards were ablated in line scan mode ($10 \times 155 \mu\text{m}^2$ slit) with a dosage of 3 laser pulses. Mass calibration and baseline subtraction, as well as integration of signals of single elements were performed using TOFWARE (<http://www.tofwerk.com/tofware>). Signals from cells were identified using the Originlab[®] peak finder function which searched for the peak centers of nucleated cells using the ^{193}Ir -DNA-intercalator signal. Peaks were integrated over a window of ± 4 data points around the peak center using an in-house written Labtalk[®] script (integration window of 270 ms). ^{165}Ho and ^{193}Ir signals from standards were integrated using the Originlab[®] integration tool.

Table 7 Overview of operation parameters of LA-ICP-TOF-MS

LA-ICP-TOF-MS operation parameters	
Plasma power	1350 W
Nebulizer gas flow (Ar)	0.7 L min ⁻¹
He gas flow in the ablation chamber	0.3 + 0.3 L min ⁻¹
TOF Integration time	30 ms

5. Results and Discussion

5.1 Quantification of metals in single cells by LA-ICP-MS: Comparison of single spot analysis and imaging

Two commonly applied LA strategies were used to measure the content of two metals at single cell level. The first mode is optimized for imaging and is based on multiple line scans. For imaging, a small laser spot size and differential scanning mode⁷ are used to obtain high lateral resolution representing a cell by many pixels which are integrated to achieve an intensity per cell. The second mode, targeted single spot ablation, is optimized for reduced analysis time, which is the basis for high throughput analysis. For such a “single pixel” measurement of intensity, a spot size larger than the cell diameter and a higher laser fluence are required.

In the following, measurement results for LA imaging and single spot analysis will be presented, see chapters 5.1.1 and 5.1.2. In chapter 5.1.3 the measurement modes will be compared with each other: first, regarding ease of use, background and throughput; secondly, the obtained elemental distributions are compared with each other; thirdly, observed differences between mean values of elemental distributions are discussed and a possible solution is proposed. Finally, in chapter 5.1.4 an LA-ICP-MS quantification strategy is applied and the quantified values are compared to quantitative data from liquid measurements of digested cells.

5.1.1 Imaging analysis of single fibroblast (3T3) cells

Multi-element imaging of single 3T3 cells stained according to section 4.1.2 was performed using previously optimized parameters for LA, see Table 2, and optimized ICP-MS data acquisition parameters, which are commonly applied for samples that were dyed using immunocytochemical methods involving several different antibodies conjugated to different metals,⁶⁶ see section 4.1.4.

To compare the LA-ICP-MS images for the Ir-DNA-intercalator and the protein stain mDOTA-Ho with the corresponding bright field image of 3T3 fibroblasts, overlays of elemental distribution images and the corresponding bright field image were prepared in CorelDraw, and results are shown for both metals, Ir and Ho, in Figure 8.

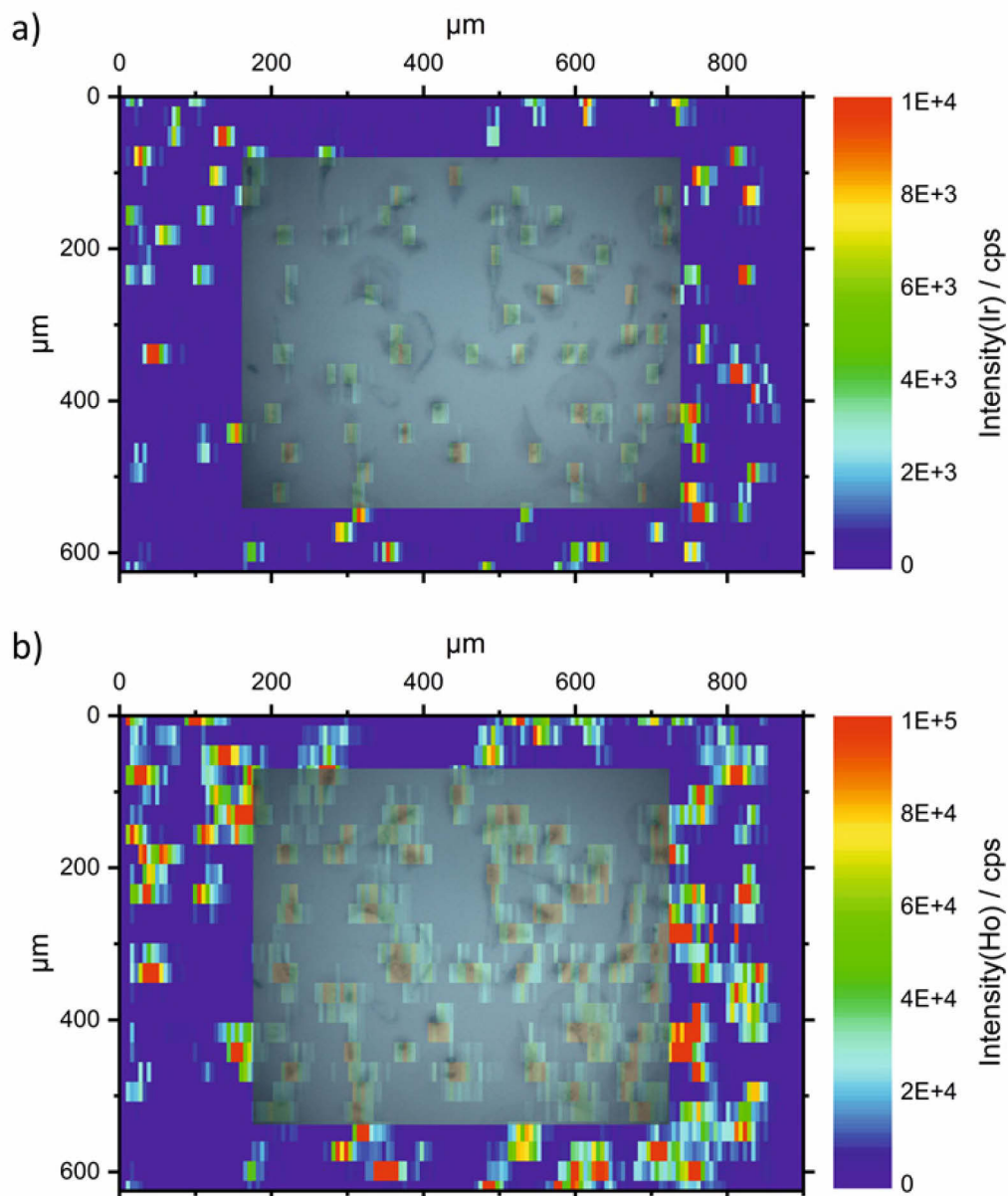


Figure 8 Multi-elemental LA-ICP-MS imaging of 3T3 cells: overlay of LA-ICP-MS image of (a) the Ir-DNA-intercalator and (b) mDOTA-Ho with its bright field image.

Comparing the overlays of Ir-DNA-intercalator (a) and mDOTA-Ho (b), it is visible that the Ir-DNA-intercalator only dyed a small spot within the cell, whereas mDOTA-Ho dyed the complete cell. That observation is in line with previous findings,⁶⁵ as the Ir-DNA-intercalator binds to the DNA in cell nuclei, while mDOTA binds to free thiol groups in proteins which are ubiquitously present in the cell. The highest intensity for Ho can be found in the region of the nuclei, which is most likely a consequence of increased cell thickness. One must keep in mind that even though LA-ICP-MS measurements are plotted as two-dimensional images, each pixel represents a voxel depending of the thickness of the fixed and dried cell.

To quantify the amount of dye on a single-cell basis, signals of 31 cells were quantified by integrating over all pixels of the cell, see procedure described in section 4.1.4. Cells were found to comprise of 27 ± 12 pixels, while the smallest cell consisted of 13 and the largest cell 69 pixels. Each integrated intensity value was corrected by a blank intensity, calculated according to the number of pixels. The average background signal of a pixel was obtained by averaging over an area of 76 pixels without cells and was found to have acceptable low values of 67 ± 69 counts for Ho and 18 ± 25 counts for Ir. The background for an averagely sized cell was found by integrating over cell-free regions of 27 pixels and resulted in 1857 ± 741 counts for Ho and 450 ± 84 counts for Ir (n=5). The background stems from incomplete removal of reagents adhering to the glass slide after incubation. Cells were found to have an average integrated intensity of $5.3 \times 10^3 \pm 2.8 \times 10^3$ counts / cell for Ir and $1.7 \times 10^5 \pm 8.8 \times 10^4$ counts / cell for Ho. A signal to noise ratio can be calculated in two ways: First, on a pixel basis, that means by comparing the average signal of a pixel of the cell with the average noise of a pixel, which would result in 7:1 for Ir and 91:1 for Ho. Secondly, by comparing the average integrated intensity of a cell with the average noise of a cell free area with the size of a cell of 27 pixels, resulting in 63:1 for Ir and 229:1 for Ho. Figure 9 shows the resulting histograms of the integrated Ir intensity (left) and Ho intensity (right) and the number of single-cell events with an intensity in the selected bin. The Ir intensity distribution appears to be a log-normal distribution centered at $\sim 3 \times 10^3$ counts having a long tail reaching up to $\sim 12 \times 10^3$ counts. The Ho distribution looks roughly like a single Gaussian centered at $\sim 1.7 \times 10^5$ counts, which is in line with the assumption that the protein content is normally distributed. The total time needed for imaging of 31 cells was about 25 min, i.e. 48 seconds per cell, see section 4.1.4.3 for further experimental details on the calculation of this number.

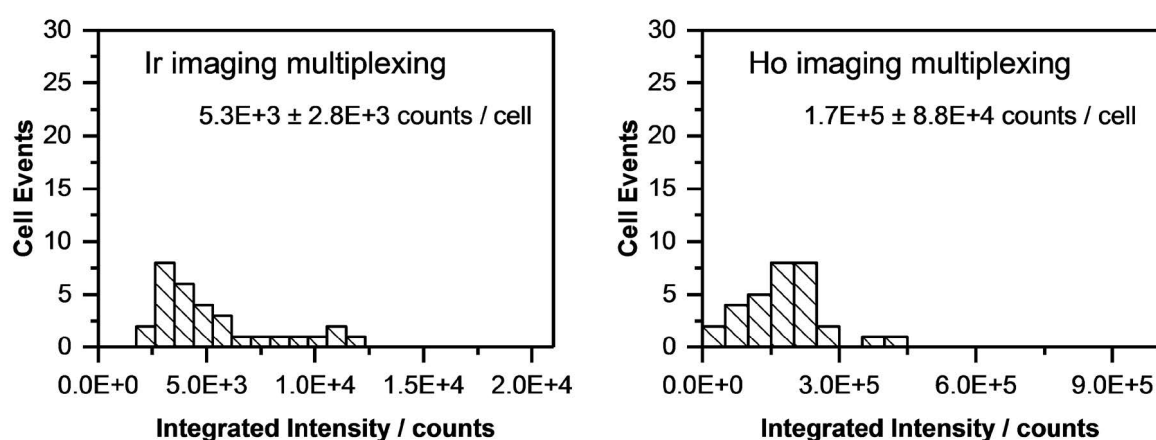


Figure 9 Histograms of Ir (left) and Ho (right) intensity per cell for multi-element imaging.

5.1.2 Single Spot analysis

Single spot analysis of single cells was performed using a spot size of 110 μm to be able to ablate each cell independently of size. Well separated single cells were selected manually and were ablated using optimized LA-parameters, see section 4.1.4, and ICP-MS data acquisition parameters optimized for multi-element analysis, see 4.1.4.2. Figure 10 shows the targeted single spot ablation of two single cells (a) before (blue circles) and (b) after ablation by three pulses. Moreover, Figure 10 (a) shows the sampling of two blanks (green circles) using the same LA conditions. In total, 46 cells were ablated in single spot mode, and 12 blank values were taken. Exemplary time-resolved plots of the transient Ir and Ho signals from the ablation of a single cell (blue) and a single blank (green) are shown in Figure 10 (c). To ensure that each cell is ablated completely, three laser pulses were fired with 20 Hz, as discussed in section 4.1.4. The measured ICP-MS signal of a single pulse has a washout time in the order of ~ 1 s, thus the signals of three laser pulses overlap and only one washout peak is visible.

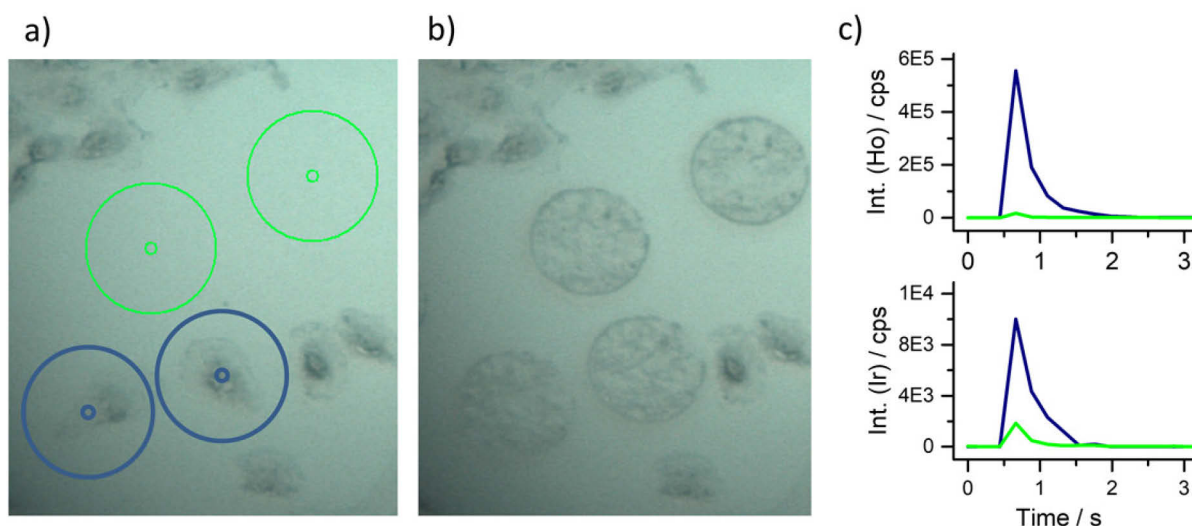


Figure 10 Single spot analysis of two single cells (blue circles) and two blanks (green circles), (a) before and (b) after ablation. Measured signal of a single cell (blue) and average blanks (green, $n=12$) are plotted in c).

Resulting Ir and Ho peaks were integrated for each cell and each blank according to the procedure described in section 4.1.4. The integrated blank intensities gave an average of 776 ± 201 counts for Ir and $4.8 \times 10^3 \pm 2.1 \times 10^3$ counts for Ho. From each integrated intensity of a single cell the mean blank intensity was subtracted which gave mean intensities of $4.9 \times 10^3 \pm 3.4 \times 10^3$ counts for Ir and $1.6 \times 10^5 \pm 9.9 \times 10^4$ counts for Ho. This resulted in average signal to noise ratios of $\sim 24:1$ for Ir and $\sim 76:1$ for Ho. Histograms of integrated intensity distributions

per single cell are shown in Figure 11 for Ir (left) and Ho (right). Using single spot analysis mode 42 cells were measured within ~ 3.5 min, i.e. 5 s per cell.

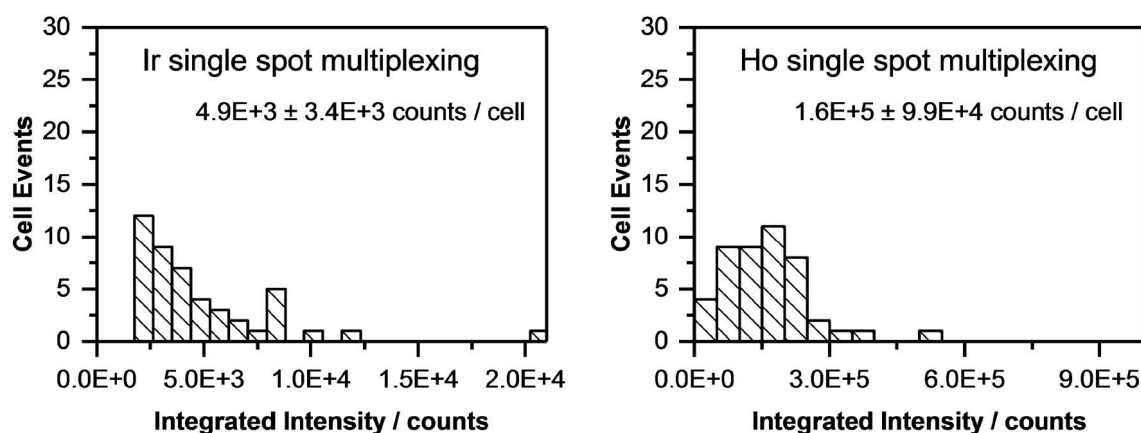


Figure 11 Histograms of Ir (left) and Ho (right) intensity per cell for multi-element single spot analysis.

5.1.3 Comparison of different measurement modes

In this chapter, the applied measurement modes presented above will be compared with each other: first, regarding ease of use, throughput and background; secondly, the obtained elemental distributions are compared with each other, and finally, observed differences between mean values of elemental distributions are discussed and a solution is proposed.

5.1.3.1 Comparison of LA imaging and single spot analysis

Most important, the LA measurement modes differ significantly in throughput. Single spot analysis with ~ 5 s / cell is about ten times faster than imaging with 48 s / cell. Thus, a lot of measurement time can be saved if only the elemental content on a single-cell basis is of interest.

Another advantage of single spot analysis is the straight forward data evaluation. As the signals of each single cell and blank are already separated due to the triggered ICP-MS data acquisition, the elemental content of single cells can be easily calculated. In case of imaging, cells must be integrated carefully, while the cell area must be chosen manually by comparing the LA-ICP-MS image with its bright field image, giving the best results, as single cells can be well distinguished from multiple cells growing close to each other. Another possibility is to select cells only based on the intensity distribution in the LA-ICP-MS image. That is a not trivial task, considering the coarse intensity distribution at a relatively large pixel size at the given resolution ($5.5 \mu\text{m} \times 25 \mu\text{m}$). On the other hand, appropriate single cells had to be selected manually for

single spot analysis as well before the measurement. Anyhow, that task is easier on a bright field image with good resolution.

The background was considerably higher for single spot analysis compared to the background from imaging of an averagely sized cell. For example, single spot analysis gave a Ho background of 4.8×10^3 counts, while for the imaging mode a Ho background of only 1.9×10^3 counts was found. The increased background for single spot analysis is approximately proportional to the total area ablated, which is about 2.6 times as large as the area ablated to image an averagely sized cell.

The comparison of signal to noise ratios is not straight forward, since for imaging the signal to noise ratio can be calculated in two ways: either on a pixel basis, or for an integrated number of pixels making up an averagely sized cell. As cells and their signals usually must be recognized on a pixel basis, only this case is considered for the imaging mode. Comparing both modes, Ir imaging has a ~ 3 times worse signal to noise ratio, and Ho imaging has an approximately equal signal to noise ratio. This is surprising, as a significantly worse signal to noise ratio for imaging was expected. A reason for that might be that in single spot analysis the background and noise was higher compared to imaging. This is a consequence of the ablation parameters used for single spot analysis: The higher fluence likely leads to the ablation of more analyte-containing coating and, more importantly, the larger spot size leads to the ablation of a larger area. The lower background for imaging results in lower noise and, consequently, a surprisingly good signal to noise ratio, although the signal of a cell is split into 27 pixels.

5.1.3.2 Comparison of metal intensity distributions

Distributions of the single-cell metal content obtained either via imaging or single spot analysis appear surprisingly similar, when comparing histograms obtained by multi-element imaging (see Figure 9) with the ones obtained by multi-element single spot analysis (see Figure 11). The mean values of the integrated standard mean intensity and the deviation are identical for both elements. No severe differences depending on the measurement modes could be recognized. It was inferred, that there was no significant instrument drift during the measurement and the instrument worked reliably over the complete measurement time of 9 h. Depending on the distribution exhibited by the datasets, one can use different statistical testing strategies to check for significant differences. mDOTA-Ho seemed to exhibit a simple Gaussian distribution, which

would allow to check for significant differences using simple statistical tests. Thus, first it was shown that H_0 distributions are normally distributed using the Lilliefors test ($\alpha=0.01$). For normal distributions, tests to compare their variances and mean values are available. The variances of both LA measurement modes do not differ significantly according to two-tailed F-test ($\alpha=0.05$). Moreover, the mean values of both LA measurement modes do not differ significantly either, according to two-tailed t-test for distributions showing equal variance ($\alpha=0.05$).

The Ir-DNA-intercalator has a more complex distribution. The binding of the Ir-DNA-intercalator is expected to be proportional to the DNA content of a cell, which is determined by its ploidy and varies from cell to cell according to its cell cycle status. It is a common application to classify the cell cycle status using quantitative DNA-dyes by fluorescence based flow cytometry,⁶⁹ where cells with one set of chromatids (2n, G1-phase) and cells with two sets of chromatids (4n, G2-phase) form distinguishable peaks in the distribution of fluorescent-DNA-dye per cell. Our measurements, see Figure 9 and Figure 11, do not show the expected bimodal Gaussian distribution. In case of imaging (Figure 9) the obtained distribution of Ir-DNA-intercalator content per cell has only one broad peak which might correspond to 2n DNA content ($\sim 3 \times 10^3$ counts), but a second peak is missing. Only a flat tail expanding to higher DNA contents up to $\sim 8n$ ($\sim 12 \times 10^3$ counts) can be seen. The distribution obtained from single spot analysis (Figure 11) also does not show the expected behavior.

To explore which effect single-element and multi-element detection mode has on imaging or single spot analysis, the Ir-DNA-intercalator content distribution was measured for a slightly larger number of cells using single-element and multi-element data acquisition (for parameters see Table 5, section 4.1.4.2). The throughput of single spot and imaging analysis is not affected by the different time resolutions of the ICP-MS data acquisition and depends only on the used LA method. The distributions obtained via single-element imaging (Figure 38, appendix) and single-element single spot analysis (Figure 39, appendix) appear to be similar to those measured using multi-element data acquisition. Next to the clearly visible peak for 2n DNA-content, a second peak which is expected for cells with 4n DNA-content is observed, but still cannot be resolved clearly. The fact that the 4n peak can be recognized better in single-element analysis could be a consequence of additional noise due to spectral skewing under standard multi-element measurements.⁷⁰ Recently, spectral skewing was subject to extensive studies and it was found that unsynchronized LA and MS data acquisition frequency leads to significant image

distortions.⁷¹ However, the herein observed differences are most likely a consequence of the low number of analyzed cells in the multi-element data acquisition, while the Ir-DNA-intercalator content was analyzed with a slightly higher number of cells with single-element data acquisition.

Given that very large RSDs were measured for all histograms, ranging from up to 53% for Ho to 68% for Ir in single spot analysis, the differences of the mean values between single spot analysis and imaging mode of ~7% for Ho and ~6% for Ir can be attributed to the relatively small number of analyzed cells. To estimate to which degree large RSDs can be attributed to biological diversity of cells (herein referring to any measurable differences), the precision of the used LA-ICP-MS setup was tested. For that, a very homogenous sample was needed, which was found in a sputtered Au/Cu coating, as usually used in electron microscopy. Such a coating is only a few nm thick and can be ablated with a single laser pulse. Single spot analysis resulted in a spot-to-spot RSD better than ~4%. Consequently, RSDs worse than 4% can be attributed to biological diversity. Accordingly, measured RSDs represent cell to cell differences which can be found due to biological diversity within one cell population.

The required number of cells (n) to determine the mean value of a normally distributed population with a predetermined relative standard error (RSE), can be calculated by solving the equation for the standard error for n :

$$RSE = t(\alpha, n) \cdot \frac{RSD}{\sqrt{n}}$$

For an RSE better than 5%, a significance level of 5%, and the maximum RSD observed for Ho (53%), the equation above was solved using the Excel solver[®], and a minimum sample size of 435 cells was calculated. It would be very tedious to measure such a large number of cells manually, which demonstrates the need for automation approaches in single-cell LA-ICP-MS, which will be the subject of further studies.

5.1.4 Quantification of LA-ICP-MS measurements and validation via liquid ICP-MS after digestion

In this chapter, an LA-ICP-MS quantification strategy is applied, the quantified values are compared to the results of a digestion of a cell suspension (see section 4.1.5) and possible differences are discussed.

As a matrix matched standard for LA-ICP-MS, a calibration series using element standard solutions was spotted on a nitrocellulose membrane (see section 4.1.3). The calibration series was ablated using the same parameters as for multi-element imaging of single cells (see section 4.1.4). Spotted standards had a diameter of $\sim 300\ \mu\text{m}$ (data not shown), which is relatively large in comparison to a cell. To save measurement time without changing LA-ICP-MS parameters, only half of each dried symmetric droplet was imaged. Signals of each half droplet, as well as blank spots were integrated using the procedure described in section 4.1.4. After subtracting blank values, calibration curves were constructed by linear regression, see Figure 40 (appendix). For ^{165}Ho a sensitivity of $1.5 \times 10^5 \pm 1.4 \times 10^3\ \text{counts pg}^{-1}$ with an intercept at $-6.2 \times 10^3 \pm 6.0 \times 10^3\ \text{counts}$ were found; and for ^{193}Ir a sensitivity of $7.2 \times 10^4 \pm 1.0 \times 10^3\ \text{counts pg}^{-1}$ with an intercept at $7.3 \times 10^2 \pm 5.5 \times 10^3\ \text{counts}$ were found, respectively. Calibration curves of both elements show very good linearity, with R^2 values better than 0.999, and limits of quantification (LOQ, $10\ \sigma$) of 12 fg for Ir and 30 fg for Ho. The higher LOQ for Ho stems from a higher standard deviation of the background on the printed nitrocellulose membrane. Blank-corrected intensities per cell from the different measurement modes were transformed into element mass per cell using the calibration curves. Table 8 gives an overview of the quantified Ir and Ho mass per single cell.

To test the validity of this matrix matched calibration approach, the mean elemental cell content was determined via cell digestion and subsequent liquid ICP-MS for both elements, see section 4.1.5 for experimental details. Mean masses of 97 fg Ir and 330 fg Ho per cell were found as an average of 60,000 cells. On average, 54% of the Ir content was found using quantitative LA-ICP-MS, and 358% Ho, respectively. Accordingly, for Ir the calibration concept worked quite well, considering that amounts quite close to the limit of quantification were measured, and that a limited number of single cells were investigated, taking into account the cell to cell variation. For Ho, the findings using LA-ICP-MS surprisingly are almost four times higher than the validation values obtained via liquid ICP-MS. This might be a consequence of losses during sample preparation. The tag mDOTA-Ho binds to proteins which are present in the membrane, in the cytoskeleton, and in the soluble fraction of the cell, the cytosol. Since for liquid ICP-MS the adherent cells were trypsinized, it is possible that mDOTA-Ho bound to free proteins in the cytosol might be lost due to small ruptures of the cell membrane. In contrast, the Ir intercalator is bound to the DNA in the nucleus and thus is inherently less susceptible to losses through membrane rupture. In future experiments, the fate of Ho should be studied in more detail. However, the values obtained by LA single-cell analysis still differ noticeably from the mean

values obtained from digestion of 6×10^4 cells, proving that this is still a viable field of research. Recently, two new promising approaches for calibrating single-cell measurements were published.^{29, 41} A study comparing elemental sensitivities of these new calibration approaches with the single-cell calibration approach used here¹⁰ would be highly desirable for the LA single-cell community.

Table 8: Quantification of Ir and Ho in single cells using three different measurement modes. LA-ICP-MS was used in two different measurement modes (single spot and imaging analysis) to quantify the Ir and Ho content on a single-cell level. Ir and Ho content was as well determined using liquid-ICP-MS after digestion of 60,000 cells. For the liquid ICP-MS measurements of digested cells no RSDs are given, since the RSDs in the table refer to cell-to-cell variance and not to the conventional measurement precision.

	193Ir			165Ho		
	SSA	imaging	digested cells	SSA	imaging	digested cells
Mean / fg	53	63	97	1146	1222	330
RSD	63%	60%		63%	52%	
n	45	31	60,000	46	31	60,000

5.1.5 Conclusion

LA-ICP-MS measurements of metal labeled single cells were conducted in two measurement modes, LA-ICP-MS imaging and SSA. Comparing both, SSA has a significantly higher throughput ($10 \times$ higher). Moreover, the evaluation of SSA data is straightforward and contributes as well to a reduced total analysis time. Concerning quantitative results, no significant differences between the measurement modes were observed with the limited number of cells analyzed: neither a change in spot size from $30 \mu\text{m}$ to $110 \mu\text{m}$, nor an increase in laser fluence from 1.0 to 3.1 J cm^{-2} altered the resulting histograms significantly. Consequently, these findings support the assumption that single spot measurements and imaging of single cells are comparable. To be able to conduct such a study with a predefined statistical reliability, it was shown that more than 400 cells must be studied. Since manual measurement in both investigated LA-ICP-MS measurement modes would become too tedious for the analysis of such high numbers of cells, it is of great importance to automate single-cell LA-ICP-MS measurements. In case of SSA, manual positioning of the laser is the most time-consuming process, which can be optimized by a cell recognition software and thus can be automated. In case of imaging, integration of all pixels belonging to a single cell using a pattern recognition software might help to speed up data evaluation, which is the most time-consuming step. Furthermore, present LA technologies already provide sub-cellular resolution. Accordingly, the imaging mode will

be used increasingly for imaging of the local intracellular distribution of metals and biomolecules using metal labels in the future. Further research within the scope of this thesis is focused on cell micro-arraying techniques to reduce the required manual steps and enable high throughput screening and quantification of metals in single cells by LA-ICP-MS.

5.2 Single-cell arraying for automated LA-ICP-MS

Single-cell arraying techniques used as a sample preparation method for subsequent mass spectrometric analysis were briefly reviewed in chapter 2.2. Since existing approaches lack a sufficiently high single cell accuracy per spot, it was decided to test two novel promising alternatives, i.e. microfluidic arraying via hydrodynamic front trapping, and piezo-acoustic arraying of droplets containing single cells using image recognition (see chapters 5.2.1 and 5.2.2).

To ensure that current LA systems are capable to ablate a cell array produced using the microfluidic approach presented in chapter 2.2.1, the NWR213 LA system (ESI) was tested for its positioning accuracy and laser stability. For that, the approximate chip geometry was used as an ablation pattern, see Figure 12 (a). Ablation of this pattern was conducted on a glass slide using a laser spot size of 200 μm and 100% energy ($\sim 6 \text{ J cm}^{-2}$) with 10 laser pulses per spot for better visibility of ablation craters. The obtained ablation pattern in the glass slide was imaged using a calibrated microscope (4 \times) with 4 ablation spots per micrograph. Images were stitched together (image composite editor (ICE), Microsoft).^{VI} The stitched image is shown in Figure 12 (b) along with measured distances and their deviation from expected values. The maximum deviation observed is only 58.5 μm and hence it can be concluded that the positioning accuracy of the stage is sufficient. The laser fluence and resulting ^{138}Ba ICP-MS signal stability was tested by ablating this pattern using a single laser pulse. First, this pattern was ablated line-by-line, which resulted in a reduced laser fluence for the first spot of each line, see Figure 12 (c, blue squares). This trend was also visible in the recorded ^{137}Ba intensity, see Figure 12 (c, black line). This is a consequence of the ~ 3 seconds break between lines, resulting in a cooling down of the laser. To overcome this behavior, first a laser warmup of three pulses was performed and second, a snake-like pattern was used for ablation, which resulted in a considerably more stable fluence and signal intensity, see Figure 12 (d).

^{VI} <http://research.microsoft.com/en-us/um/redmond/projects/ice/>

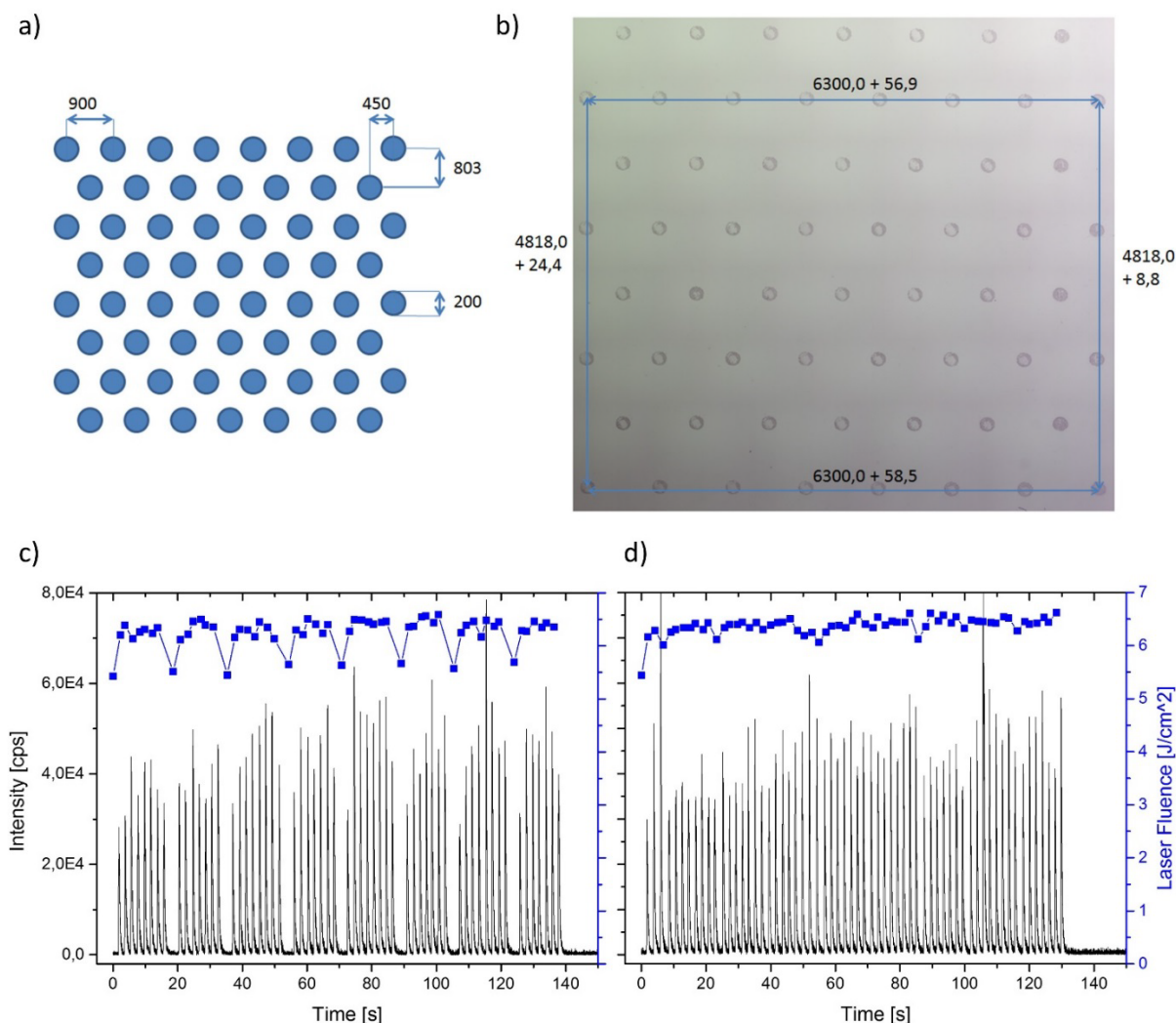


Figure 12 (a) Approximate chip geometry used as ablation pattern. (b) Dimensioning of expected values and observed deviation in stitched images of the ablation pattern using ICE. (c) Ablation of a chip pattern as line of single spots scanning in the same direction (each line from left to right) on a glass slide. LA-parameters: 200μm spot diameter, 100% laser energy; ICP-parameters for ^{137}Ba : sample time 0.002 s, mass window 0.05, samples per peak 100, integration window 0.05, peak search window 0, laser fluence $6.24 \text{ J cm}^{-2} \pm 4.7\%$. (d) Ablation like in (c), including laser warm-up (three pulses) and a snake-like pattern (every second line with reversed scanning direction: first line left to right, then second right to left and so on). All dimensioning in μm.

The last parameter optimized was the ICP-MS integration time, as it was expected that an increase in sample time would decrease the overall noise. Blank measurements showed that the instrument noise for the method decreased from 54% to 17% RSD for a tenfold increased sample time. In this way, the RSD of the integrated ^{137}Ba peaks was considerably lowered. This finding was surprising, since integrated peaks are compared, where point-to-point deviation is averaged out to a huge extent by the integration itself. A possible explanation is instrument specific signal loss in case of short integration times. It can be calculated that the time without

signal acquisition was reduced from 20% to 2%, as the sample time was increased from 2 ms to 20 ms. Table 9 provides an overview of optimized parameters and corresponding effects.

Table 9: Optimization of the ablation of an array-like pattern on a glass slide. Remark: differences in mean ^{137}Ba intensity reflect differences in ICP-MS instrument tuning rather than differences of the used LA method.

	^{137}Ba per peak [counts]			Laser Fluence [J cm^{-2}]		
	mean	SD	RSD	mean	SD	RSD
original pattern, line-by-line	40371	8081	20%	6.25	0.29	4.7%
snake-like ablation	14953	2103	14%	6.33	0.18	2.9%
laser warm-up and snake-like pattern	16132	2793	17%	6.39	0.13	2.0%
10x increased sample time	16450	1907	12%	6.39	0.13	2.0%

Previously, peak-to-peak RSDs down to $\sim 4.6\%$ were observed for the ablation of a printed nitrocellulose membrane (unpublished data; printer: Canon Pixma iP4950; collaboration with Proteome Factory, Berlin). It was suspected, that the microheterogeneity of Ba in the used glass slides could be the reason for the increased RSDs. The standard reference material NIST 610 is well studied and no microheterogeneity for Ba was expected.⁷² Surprisingly, an even higher peak-to-peak fluctuation of Ba was observed (RSD 21%). To check whether this was a consequence of microheterogeneity, a glass slide coated by sputtering with a thin layer of Au/Cu was used as a very homogenous sample for a similar experiment.^{VII} This resulted in a spot-to-spot RSD as low as 3.7% for Au, using LA parameters adapted to this sample (spot size 50 μm , laser fluence 1 J cm^{-2}). Similar low RSD values were reported for metal-spiked inks printed on nitrocellulose membrane, demonstrating that homogeneity is essential for low RSD values.⁷³ Furthermore, this suggests that a standard which is completely ablated has considerably lower RSDs (4%), compared to single spot ablation of a sample which is homogeneously distributed in bulk material (like the RSD of 12% observed for SSA of Ba in bulk glass). Accordingly, in the future, complete ablation of standards should be favored over ablation from a bulk material for calibration.

5.2.1 Microfluidic single-cell arraying

Among the different microfluidic approaches for cell positioning, it was decided to focus on hydrodynamic front trapping approach combined with the micro chamber array chip design for analysis of intracellular biomolecules in single cells (see chapter 2.2.1).⁵⁶ A major advantage of

^{VII} Kindly provided by Kevin Bethke, AB Prof. Rademann, HU Berlin.

this design is that cells can be treated with compounds in a controlled microenvironment using small sample volumes. This approach enables optical on-chip assays for e.g. cell stress and viability, which would be especially beneficial for toxicity assays for inorganic compounds. It was the goal to develop strategies to enable LA-ICP-MS measurements using this platform, which was invented in the group of Prof. Petra Dittrich (Bioanalytics group, ETH Zürich). The first part of the herein presented experiments were performed during a 4 months guest stay in the Bioanalytics group. In these experiments it was focused on arraying of yeast cells, as research in the Bioanalytics group was focused on the two yeast cell lines *Saccharomyces cerevisiae* and *Pichia pastoris* at that time. Moreover, the *Pichia pastoris* strain was genetically modified to produce magnetic iron-oxide nanoparticles, which would present an interesting sample for LA-ICP-MS analysis. Developed methodologies were subsequently adapted to a mammalian cell line (THP-1 suspension cells) at BAM (Berlin).

5.2.1.1 Chip operation in a clamping device

Deviating from the usual operation mode for e.g. studies via fluorescence microscopy, interfacing with LA-ICP-MS requires direct access to cells. That means after cell capturing and treatments, the chip must be removed again for accessibility of cells for LA. The usually used plasma activated bonding of chips to coverslips is a durable sealing of microfluidic channels. This sealing enables high flow rates (e.g. $100\ \mu\text{l min}^{-1}$) that can be used to wash randomly adhering cells away. An existing concept to avoid permanent bonding of chip to cover slip is the usage of a clamping device to press the chip against the cover slip. Figure 13 (a) shows a clamping device which was previously employed in the Bioanalytics group. A PDMS chip is clamped onto a coverslip by screwing a PMMA glass slide (with holes for tubing) onto the chip using 8 winged nuts.

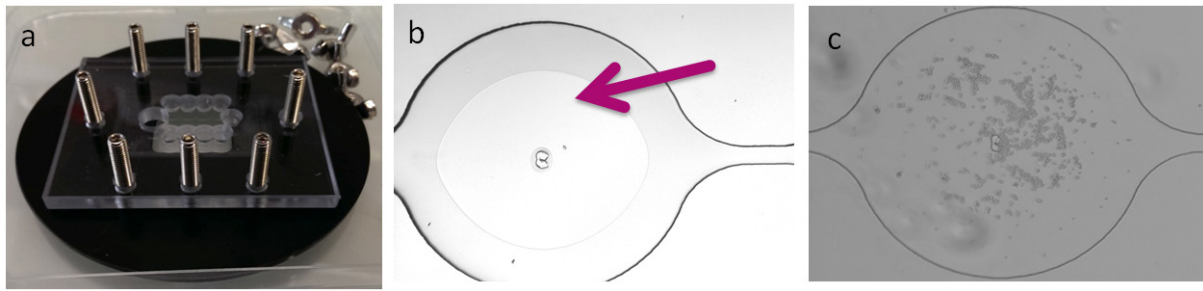


Figure 13: (a) Existing clamping device. (b) Observed optical effect if channel ceiling touches glass ground: due to the direct contact this area appears slightly brighter. (c) “ceiling ground cell trap”: originating from too high clamping pressure, the channel height was decreased to a few micrometers, such that cells were trapped.

Although the clamping technique is known for some time, routine work is still challenging with micro-chamber-array chips. A major challenge is the application of proper clamping force. Insufficient clamping force leads to leakage of liquid and cells from channels, too high clamping force leads to breakage of the coverslip or compression of channel heights until channels are completely blocked, as can be seen in in Figure 13 (b). This optical effect was the only observable pressure indicator. By decreasing the pressure via unscrewing the winged nut, the channel’s ceiling can subsequently be lifted from the glass again. However, this process was found to lack repeatability due to the low manufacturing precision of used screws, the great effect of small turns and the very small, not measurable torque. In first experiments, a highly unequal and hardly repeatable distribution of this effect was observed across the chip, although special attention was paid to achieve an equal clamping force distribution.

Switch from cover slips to glass slides

The reason for the unequal clamping force distribution was the very thin coverslip which was bending at such forces. Moreover, the commonly used $\sim 145\ \mu\text{m}$ thin coverslips (*Menzel #1*) were found to be quite susceptible to breakage. Thus, in clamping applications they are often replaced by $\sim 300\ \mu\text{m}$ thin coverslips (*Menzel #3*), which is a tradeoff between mechanical stability and usability of the assembly in combination with an inverted microscope due to limited working distances of high magnification objectives. *Menzel #3* coverslips were less likely to break. To control even channel heights, fluid layer channels were filled with diluted red food dye and light absorption was observed using a brightfield microscope across the whole chip. Light absorption differed remarkably between channels in the middle and channels in the

outer regions, which means that the cover slip still showed remarkable bending, resulting in unfavorable differences in channel height (data not shown).

Glass as a carrier material is unfavorable for subsequent LA-ICP-MS analysis because it contains numerous elements which might interfere with the elements of interest in future applications (e.g. 0.03% Fe_2O_3).⁷⁴ A convenient workaround are coated glass slides. The commercially available glass slide *Menzel Super Frost plus* has an organic coating which can prevent the ablation of glass. Moreover, glass slides are thicker (1000 μm) than coverslips and thus are mechanically more stable. Accordingly, it was decided to switch to this kind of glass slides for chip clamping. A 1000 μm thick glass slide only allows for limited magnification under an inverted microscope (up to 20 \times), since the working distance of objectives decreases with increasing magnifications. However, this disadvantage is acceptable due to the gain in stability and lower background for elements abundant in glass. The chip can be clamped between two almost rigid layers (PMMA / glass), which greatly enhances the reachable 2D uniformity of the observable compression across the chip.

Usage of springs for adjustment of force in a novel clamping device

In Figure 14 (a) the new clamping device is shown. To facilitate the adjustment of a uniform clamping force load, the number of screws was decreased to four, each located in one corner. Additionally, springs were used as a measure for the applied force at each screw. The force of all four-winged nuts is now transduced via a spring to the PMMA glass and subsequently to the chip. Three different wire diameters were tested for their suitability as visual pressure sensors, see Figure 14 (b). The spring with a wire diameter of 0.7 mm and 7 turns was found to have the proper stiffness, such that a repeatable clamping force can be adjusted in every corner. Figure 14 (c) illustrates the method to adjust a defined force on the PMMA glass: all four springs must be compressed to an equal length (green arrow). For that, the turns of the screw above the winged nut (red arrow) and below the PMMA glass (blue arrow) must have the same constant sum for every screw. Experimentally a suitable clamping force was determined for around ~9 visible turns per screw for chips which were ~0.5 mm thick.

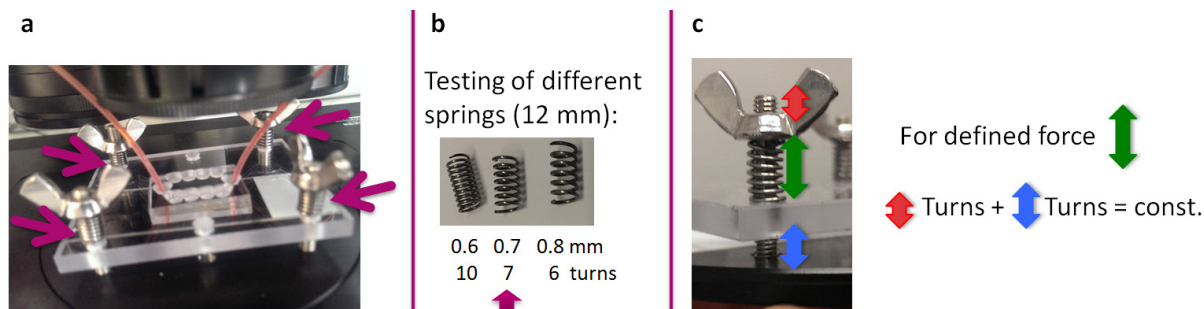


Figure 14 (a) Design of the new clamping device. (b) Custom-made springs (12 mm in height) with three different wire diameters which were tested for their suitability as mechanical pressure sensors. (c) Illustration of the strategy to apply the same clamping force to all corners.

Filling of the microchip with liquids

Bubble free filling of all channels is usually performed via centrifugal force, see Eyer *et al.*⁶⁰ This commonly used approach cannot be used if a clamping device is used. The filling strategy differs for the two layers. The control layer channels can be filled using the pneumatic pressurization device after preloading each connector and tubing with $\sim 10 \mu\text{L}$ water per line. By applying a pressure of 2 to 3 bars, the air within control layer channels solves in the PDMS chip and is replaced by water. This approach is not working for the fluid layer because at such high pressures the chip was lifted from the glass slide and liquids leaked out of channels, even though very high clamping forces were applied. Approaches like clamping of chips submerged in water, and sucking liquid into the chip via a pump, failed due to small bubbles adhering to the fine structures within the fluid layer, or resulted only in a partly filling of fluid layer channels. Finally, pumping liquid into the chip at a moderate flow rate of $20 \mu\text{L min}^{-1}$ was tested. In this way, it was possible to eliminate all air bubbles within ~ 10 min. Afterwards, it was possible to trap several yeast cells in a clamped chip by flushing a yeast cell suspension through the fluid layer channels using previously described procedures.^{56, 59}

5.2.1.2 Transfer of cells to a glass slide and necessity of the control layer

For single-cell LA-ICP-MS, the chip must be removed from the glass slide to grant access to arrayed cells. After removal of the chip, arrayed cells should be presented on the flat glass slide. The easiest approach tested was to lift the chip after cell arraying and dry the cells and remaining solution under atmospheric conditions, but this proved to be not feasible. Whenever the chip was lifted, the solution in fluid layer channels formed a single large droplet due to surface tension forces. Beforehand arrayed cells followed the liquid flow and were distributed randomly

inside the big droplet. To circumvent this problem, the solution in fluid layer channels must be pumped out or evaporated before disassembling the clamping device. This process should be rather fast to prevent e.g. dissolution or diffusive losses of analytes from cells and needs to be non-disruptive for cell membranes. First, removal of liquids by sucking or pushing air through the fluid layer using syringe pumps was tested, but thereby parallel channels were dewetted only partially. As soon as one of eight parallel channels was dewetted, air can pass through the chip from inlet to outlet. By such, dewetting of remaining channels was not possible using syringe pumps due to the limited volume of suitable syringes. Using vacuum pumps or a flow of pressurized gas are possible options for chip dewetting without a volume restriction.

Since pressurized air is commonly available in laboratories, this approach was preferred over vacuum pumps and pursued further. In first experiments, two effects which complicate chip dewetting were observed. First, a reversed flow of liquids in some channels was observed repeatedly, which lead to loosing of all cells in these channels. This unexpected effect happened only after at least one channel was cleared from liquids such that air was able to flow freely from inlet to outlet and was assumed to be a consequence of the so-called Venturi effect.^{VIII} Second, a high probability of cell loss from traps during chip dewetting was observed, even in channels without any flow direction reversal. This was found to be a consequence of surface tension forces, which forced cells out of microhurdle features, see Figure 15 (a). To avoid both problems a novel two-step drying process was employed, as shown in Figure 15 (b and c). First, donut shaped valves were closed to protect cells from possible backflow and interfacial tensions during dewetting. By applying 0.75 to 1 bar N₂ to the chip inlet it was possible to dewet and dry all parallel channels within few minutes. In a second step, donut shaped valves are opened again while N₂ is flushed through the chip. The remaining, previously encapsulated liquid (~625 pL) is evaporated within ~20 s.^{IX} No reversal of flow direction was observed, as air can flow freely through all parallel channels.

^{VIII} The flow of air in an empty channel creates a negative pressure at in- and outlet of neighboring channels, which are still filled with liquids. The resulting negative pressure at either end is proportional to the velocity of the air stream and the area of fluid subjected to the resulting negative pressure. If negative pressure at the inlet is bigger than negative pressure at the outlet this can lead to the observed backflow.

^{IX} This holds only for a single trap. For eight traps connected in series, ~20 s per trap are needed to evaporate the 625 pl, since the N₂ stream is not dry anymore (summing up to 160 s for eight consecutive traps).

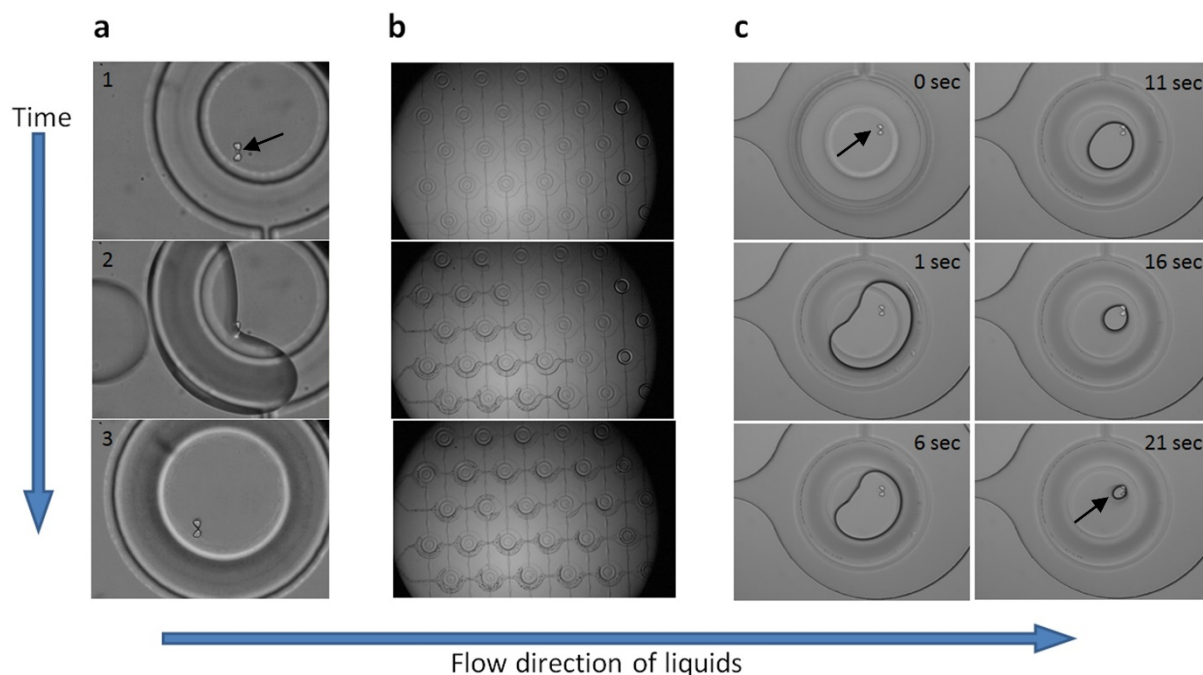


Figure 15 (a) Loss of a single cell (see black arrow) due to surface tensions if drying is performed without closing of donut shaped valves. In (b) and (c) an advanced two-step drying process is shown. In a first step (b), channels are dried with closed donuts such that cells are protected from interfacial forces. In the second step (c), the donut shaped valve is opened and the remaining ~ 625 pL encapsulated by the valve are dried reliably via evaporation. Here, drying of a mother-daughter budding yeast is shown (marked with black arrow for 0 sec and 21 sec).

Interfacial tension forces keep previously encapsulated liquid in place, such that the remaining ~ 625 pL dried preferably towards the microhurdle, leading to a highly defined positioning of cells. If a trapped cell is leaving the trap during drying, or is located anywhere else within the microchamber, it was observed that cells are usually pulled towards the two pillars due to interfacial tensions, see Figure 16 (a). After dewetting and drying of all liquids, the chip can be lifted from the glass slide and dried yeast cells were found to be located predominantly on the glass slide, presumably due to gravitation. In Figure 16 (b), all cells from the dried agglomerate shown in Figure 16 (a) were transferred to the glass slide. The PDMS-surfaces of the chip fluid layer were free of cells. First experiments showed, that trapped cell-agglomerates and crystals formed from dried solvents (in or around the trap) made the sticking of cells to the chip likelier. Thus, the dewetting and drying step was always performed after a washing step using water (purified to $18.2 \text{ M}\Omega$ using a Millipore Milli-Q water system). Due to problems regarding the photolithographic manufacturing process of yeast cell traps on chip negatives (wafers), it was not possible to array a sufficient number of cells and obtain statistics regarding the efficiency of this process.

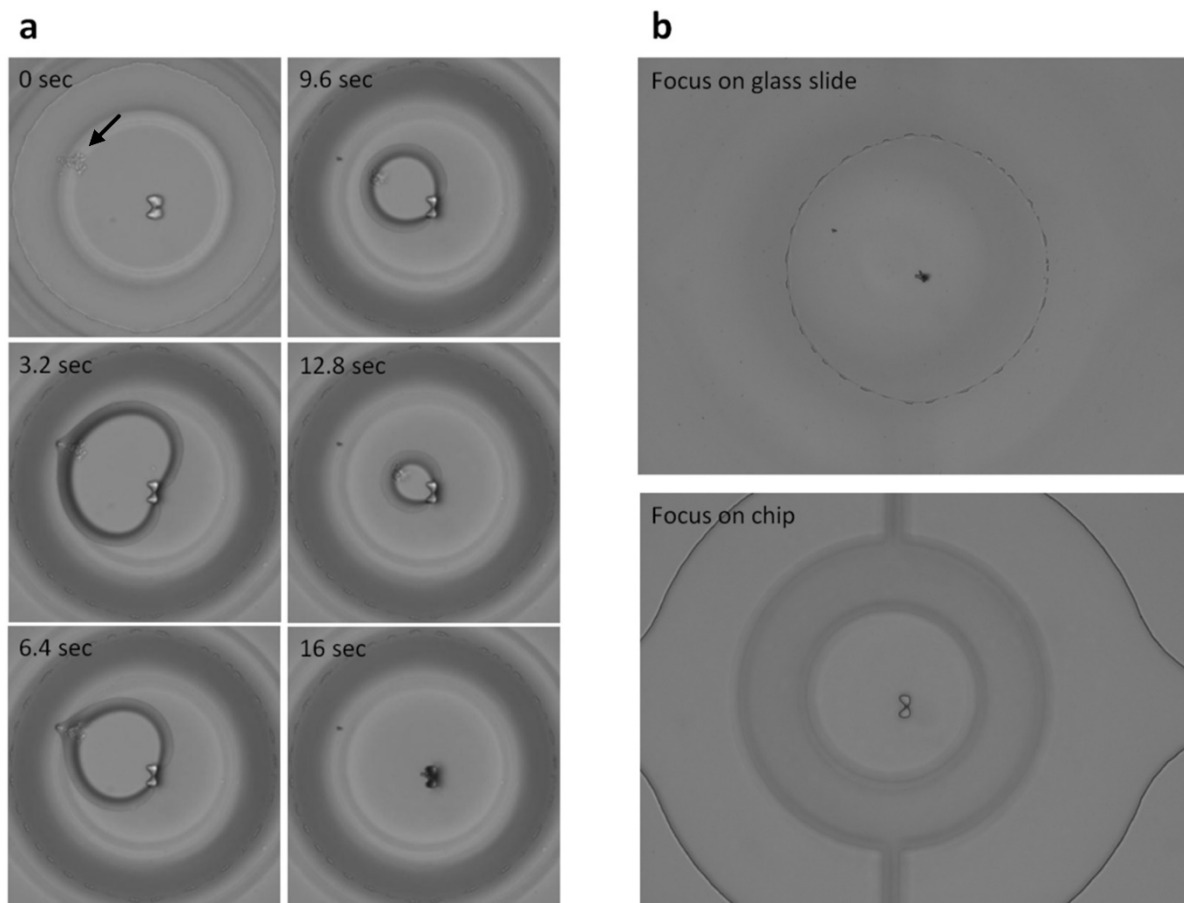


Figure 16 Drying of a micro-chamber which contains a big cell agglomerate within 16 seconds is shown in (a). The agglomerate is located next to the donut valve in the upper left corner before opening of the valve at $t = 0$ sec, see black arrow. After valve opening, the liquid forms a “bridge” between the agglomerate and trap due to interfacial tension and the agglomerate is transported towards the trap during evaporation of liquids. After slightly lifting the chip, micrographs were taken with focus on glass slide or chip, see (b). All cells were found to be located on the glass slide. Besides the big agglomerate, a smaller remainder of the agglomerate is visible at its initial position, still sticking to the glass slide.

5.2.1.3 Adaption of processes to new lab environment

It was planned to establish developed microfluidic methods for single cell arraying at BAM. Most microfluidic standard equipment could be adequately substituted by equipment available in BAM’s new microfluidics facility. A new pressure control system needed to be engineered and constructed (collaboration with Andreas Schulz, technician, BAM Division 1.1). A mechanical system was found sufficient regarding cost efficiency and ease of use. To allow independent actuation of eight parallel lines of donut-shaped valves, the device was equipped with eight in-house fabricated valves, which used spring actuated wedges to compress the pressure lines’ silicone tubing. Moreover, the device was equipped with a main valve to allow

on / off switching of the eight pressure lines at once. As mentioned earlier, the control layer must be filled with water using pressurized air before the chip can successfully be used. For convenient suction of water into all silicone pressure lines at once, a syringe was integrated. To protect the syringe from high pressures during donut valves actuation, an additional on / off valve was integrated. For chip dewetting, only 0.5 to 1 bar are needed. Thus, a pressure reducer was integrated, which can be manually controlled by using an additional manometer to measure the reduced pressure. A sketch of the constructed pressure control system is shown in Figure 17.

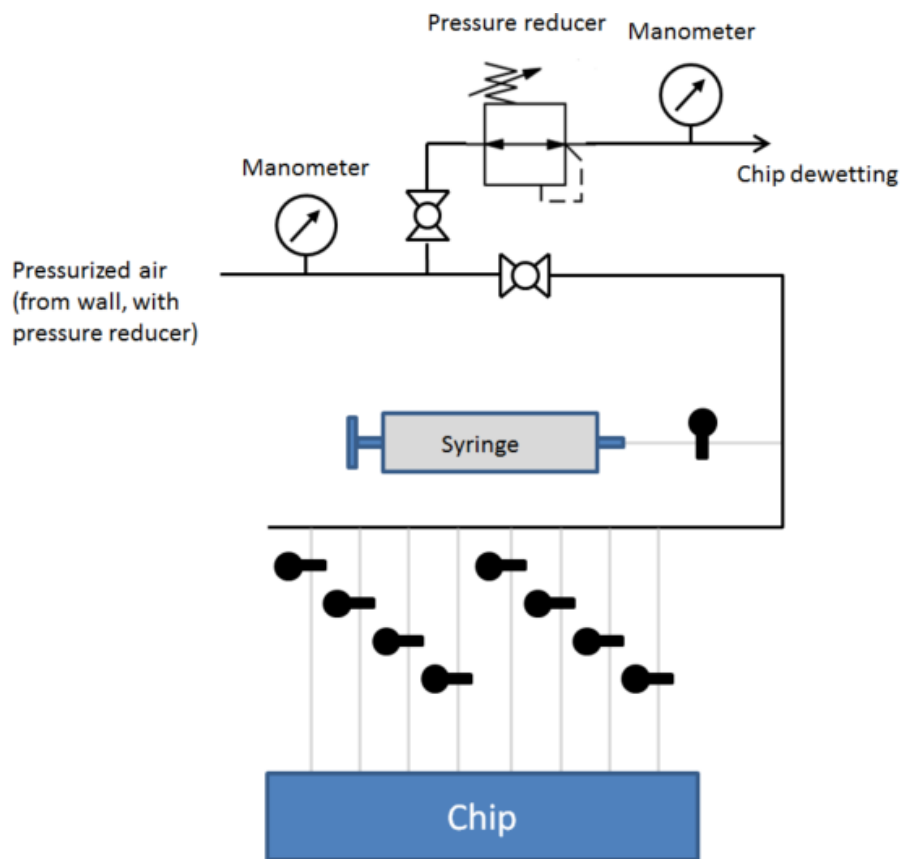


Figure 17 Sketch of the constructed mechanical pressure control system. Black lines represent solid metal tubing; grey lines represent flexible silicone tubing; in-house fabricated valves are represented as rotary knobs with (spring actuated) wedges used to compress the pressure lines' silicone tubing.

5.2.1.4 Arraying of THP-1 cells

As it turned out that the problems associated with the photolithographic manufacturing process of the very fine structures (required for the microhurdles to capture small cells like yeast) were more severe than expected, it was decided to use the chip negatives (wafers) with microhurdles

for bigger cells, which can be reliably produced with sufficient precision.^{56, 57, 60} Additionally, the advantages of single-cell sample introduction to the ICP-MS via arraying and subsequent LA are more prominent for bigger cells. Accordingly, all further studies focus on human THP-1 suspension cells, which are 10 to 20 μm in diameter (i.e. 2 to 7 times larger than yeast cells).

For cell arraying, a previously successfully applied flow rate ($30\ \mu\text{L min}^{-1}$) was used as a starting point for trapping fixed THP-1 cells.^x In order to minimize compression of fluid layer channels (20 μm in height), the minimum necessary clamping force was applied by tightening the clamping device screws until fluid layer channels did not leak. In a first attempt to array THP-1 cells, surprisingly no cells were visible in the fluid layer. After disassembly of the chip, many cells were found in the inlet region. It was concluded that cells got stuck before entering the fluid layer channels, because the diameter of THP-1 cells was larger than the height of the fluid layer channel. Since the channel height decreases according to the clamping force, the clamping force needed to be optimized. As the clamping force was lowered, the chip started to leak at the initial flow rate. Consequently, the clamping force and the flow rate were carefully balanced and step by step the clamping force was lowered. At a flow rate of $10\ \mu\text{L min}^{-1}$, a minimum clamping force was applied (spring length of 7.5 turns), whereby fluid layer channels were decompressed but did not leak. Compared to previously performed experiments (using glass slides and chip design for yeast cells), the maximum flow rate needed to be further decreased. Using optimized conditions, several cells were successfully flushed into the fluid layer channels, see Figure 18 (a), while the majority still got stuck in the inlet region or fluid layer channels as the channel diameter increases around cell traps, see Figure 18 (b). Two single THP-1 cells were trapped successfully, see Figure 18 (c). Previously developed methods to transfer cells to super frost plus glass slides were applied, and one of two cells got stuck in the trap, see Figure 18 (d).

^x Access to this cell sample was made possible by Dr. A. Lopez. Cells were prepared in the labs of Dr. Haase (BfR, Berlin).

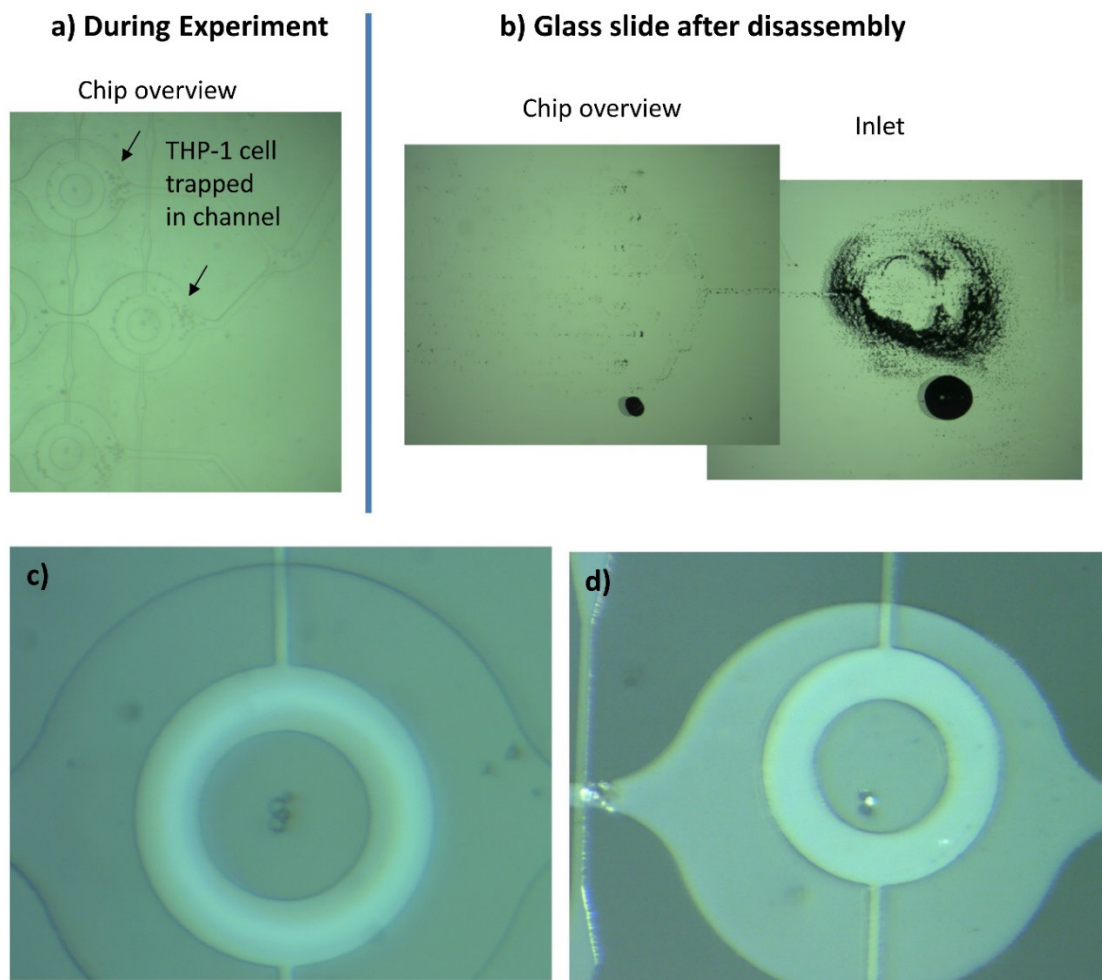


Figure 18: Behavior of fixed THP-1 cells in a chip with 20 μm channel height mounted in a clamping device. In (a) the behavior during the experiment is shown. THP-1 cells predominantly get stuck before reaching the cell trap. In (b) an overview after a trapping experiment is shown. Most cells get stuck at the inlet and cannot enter fluid layer channels. (c) Successful trapping of single THP-1 cells during experiment. (d) After disassembly of the chip, one of two single cells got stuck in the trap.

This experiment was repeated several times and single cell (or single polystyrene beads with $d=12\ \mu\text{m}$ and $-\text{NH}_2$ coating, kisker biotech GmBH) occupancies up to 15% were reached, but not exceeded. This is significantly less compared to reported single-cell occupancies (75%)⁵⁶ and likely is a consequence of chip clamping. As described above, cells could not flow freely within the fluid layer channels because they got trapped in the inlet region and wherever fluid layer channels widened. The recurrent problem of compressed fluid layer channels was identified as the main problem, which prevented a successful application of this microfluidic device to array a sufficiently high number of single cells for LA-ICP-MS. Several approaches to solve this problem are imaginable. A more rigid material than PDMS could be used for

clamping, but this would adversely affect the possibility to close donut-valves by pressure application. A straight forward possibility would be to use existing masks to fabricate master molds with a higher channel height, but this would lead to elongated cell traps which are able to host multiple cells. Moreover, the clamping pressure on such elongated cell traps would possibly lead to deformation of cell traps, and the pressure needed to actuate the donut-valves would be higher. In case several cells were captured within one microhurdle, this would be hardly recognizable due to their exact same positioning via the microhurdle and the broad focus of common objectives. Another possibility would be to reengineer the chip design with the goal to decrease aspect ratios of fluid layer channels. Cells got stuck between ceiling and ground, i.e. around the cell trap, where the herein used chip design had the largest aspect ratio (channel diameter / channel height). Cell traps are in the middle of an approximately round channel with a diameter of 600 μm in channels, and channels are 20 μm in height, leading to an aspect ratio of 15. This is already 50% more than generally recommended, see ‘The Evolution of Design Rules for Biological Automation’ by Quake *et al.*⁷⁵ For chips operated in a clamping device, no recommendations exist yet, but aspect ratios should be generally lower compared to chips operated under normal conditions. Introduction of design features like pillars between traps are a convenient method to reduce such aspect ratios.⁷⁵

For the transfer of arrayed cells or beads from assembled microfluidic chip to the Superfrost plus glass slide, a transfer efficiency of about 50% was estimated after this experiment series. To obtain better transfer efficiency for positioned cells or beads, PDMS surfaces could be coated with fluoropolymers. Such coatings were previously employed in microfluidics to prevent chip swelling induced by organic solvents.⁷⁶

5.2.1.5 Conclusion

A recently developed method for single-cell arraying and subsequent analysis of intracellular biomolecules was tested for its suitability to array cells for subsequent LA-ICP-MS analysis. For that, a novel method for dewetting and drying of chips was developed which prevented unfavorable repositioning of cells during dewetting. A novel clamping device was constructed which allows usage of coated carrier glass slides favored for LA-ICP-MS analysis. Existing methods to manufacture and operate double layer PDMS-based microfluidic devices were successfully transferred to a new lab environment and a novel mechanical pressure control system designed according to needs for single-cell LA-ICP-MS sample preparation was

constructed. Beyond these initial successes, it was found that existing protocols for single-cell arraying cannot be transferred in a straight forward way to chips operated in a clamping device. To enable delivery of cells to microhurdles a steady flow of cell suspension must be ensured. To enable a steady flow, a flow-rate-dependent clamping force must be applied to seal fluid layer channels. This clamping force in combination with the high compressibility of PDMS chips was found to be problematic. Fluid layer channels are compressed by the clamping force needed to seal fluid layer channels, leading to potentially deformed microhurdles and cells getting stuck in the inlet region as soon as the channel diameter widens. Another single-cell arraying approach based on piezo-acoustic arraying of droplets containing single cells was tested independently at the same time and was considered more promising as a sample preparation method for subsequent LA-ICP-MS, see section 5.2.2.

5.2.2 Piezo acoustic single-cell arraying approach in conjunction with image recognition of cells

In this section, a novel technique for single-cell arraying based on a piezo-acoustic microarrayer (sciDROP PICO[®] mounted on a sciFLEXARRAYER S3 axis system, Scienion AG) was tested. The device uses a novel software module which was kindly provided by Scienion AG (cellenONE[®] software, cellenion SASU). The software enables automated optical detection of cells within the piezo dispense capillary (PDC) prior to each droplet generation. In this way, dispensing of droplets containing single cells onto an array becomes possible by eliminating droplets containing multiple cells or no cell.

5.2.2.1 Image recognition and automated mapping of PDCs

Figure 19 shows the image recognition procedure demonstrated for 15 μm polystyrene beads and THP-1 cells. First, image recognition parameters for beads were optimized: After subtracting the background from the brightfield image (a), the image is first transformed into a binary image via thresholding (b). The binary image is processed using two erosion cycles and finally only objects with a specific area (here: 150 pix to 500 pix) are recognized as beads (c). In (a), every recognized bead is marked with a light blue dot. Image recognition parameters for THP-1 cells were not yet optimized. As can be seen in Figure 19 (a), THP-1 cells have quite different optical properties compared to 15 μm polystyrene particles. Only two out of six cells were recognized in the brightfield image. The four cells marked with blue arrows in (a) still can be seen partly after subtraction of background. After the application of filters and parameters

optimized for recognition of 15 μm polystyrene beads, those four cells cannot be recognized anymore (c). Two red arrows pointing out dark areas in the bright field image correspond to cells adhering to the PDCs inner wall and were already present in the background. Thus, these dark areas were not recognized after background subtraction and thresholding.

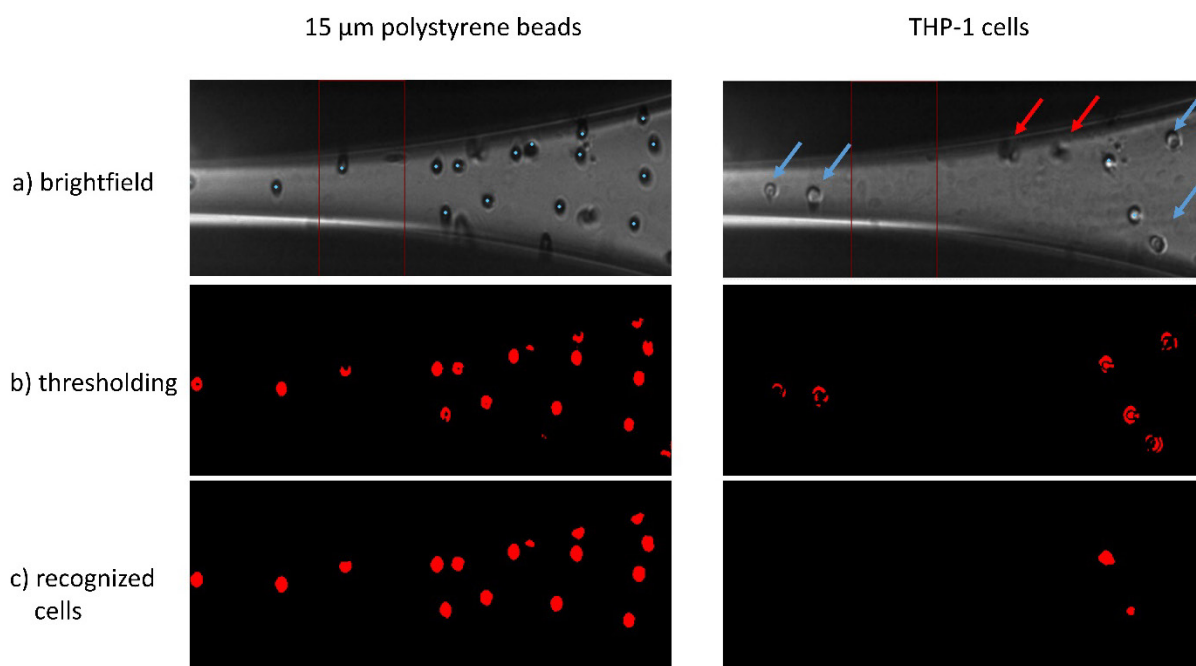


Figure 19 Image recognition of 15 μm polystyrene beads and THP-1 cells in the PDC: a) brightfield image, b) binary image after thresholding, c) cells (or beads) recognized after two erosion cycles, having a specific number of pixels (area between 150 and 500 pixel).

Only a careful optimization of original image recognition parameters led to a reliable recognition of THP-1 cells. Especially minimal area (from 150 to 50 pix) and intensity threshold (from 35 to 10) had to be substantially lowered, as cells had a weaker contrast compared to polystyrene beads. In Figure 20, mapping experiments with (a) original and (b) optimized settings for image recognition of cells are shown. The blue dots represent recognized cells which were successfully tracked after the subsequent droplet generation. Green dots represent cells at locations where it was not possible to track after the next droplet ejection. As can be seen, the green dots spread over a huge span of the PDC in Figure 20 (a), whereas in Figure 20 (b) only very few green dots can be seen, since optimized settings were used. Therefore, cells were tracked successfully until ejection from the PDC. Accordingly, after optimizing the image recognition parameters, cells were detected sufficiently reliable to enable a successful mapping experiment.

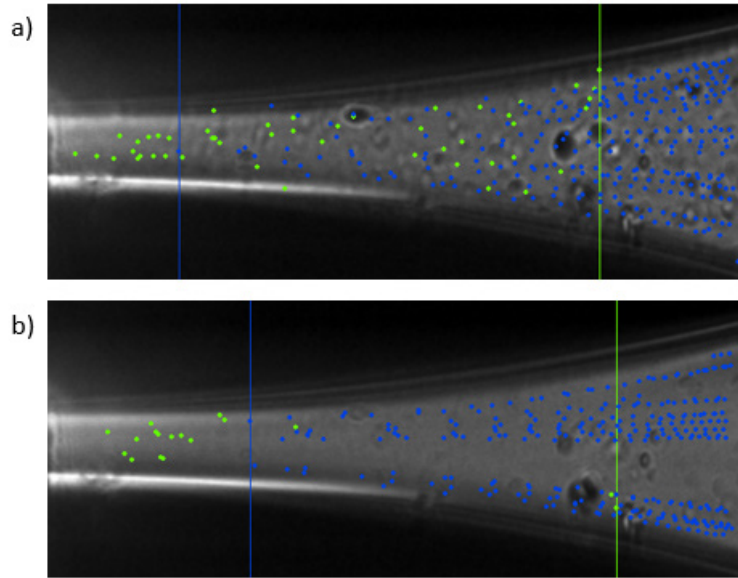


Figure 20 Result of a mapping experiment of THP-1 cells with (a) original and (b) optimized image recognition settings. Green dots equal to untrackable cells, blue dots represent trackable cells, the blue vertical lines indicate the trackable cell which was closest to the nozzle outlet (and thus this is the border of the ejection zone), the green line indicates the untrackable cell which was furthest away from the nozzle outlet.

5.2.2.2 Visual inspection of printed cell arrays

Using optimized image recognition parameters and the ejection boundary from the mapping experiment, it was possible to fill 269 array positions within ~ 2 hours without any further adaptations. To control resulting single-cell arrays for positioning accuracy and single-cell occupancy, the array was imaged using the autofluorescence of cells using a microarray scanner (MArS, DITABIS - Digital Biomedical Imaging Systems AG) and a brightfield microscope at different magnifications, see Figure 21 (a-c). Here, all cells are surrounded by a dried spot of cell culture medium (RPMI) which originates from its ~ 230 pL droplet. In later experiments, cells were washed before spotting, to prevent background signal from cell culture medium, and to get rid of excess tagging reagent in case of cell tagging. Using MArS (Figure 21 a), it was possible to image the whole array very fast, but only at limited resolution ($10\text{ }\mu\text{m}$). Thus, it was not impossible to distinguish between two adjacent cells within a single spot. The same holds true for 4x brightfield microscopy. Only at 20x magnification, it was possible to reliably distinguish between two adjacent cells. Unfortunately, no imaging system which reliably images complete glass slides fast, automated and with the necessary resolution was available. Hence, a portable brightfield microscope which allows for different magnifications was used to

monitor the single-cell occupancy of arrays in the following experiments to optimize arraying throughput and single-cell occupancy in dependence of the cell concentration.

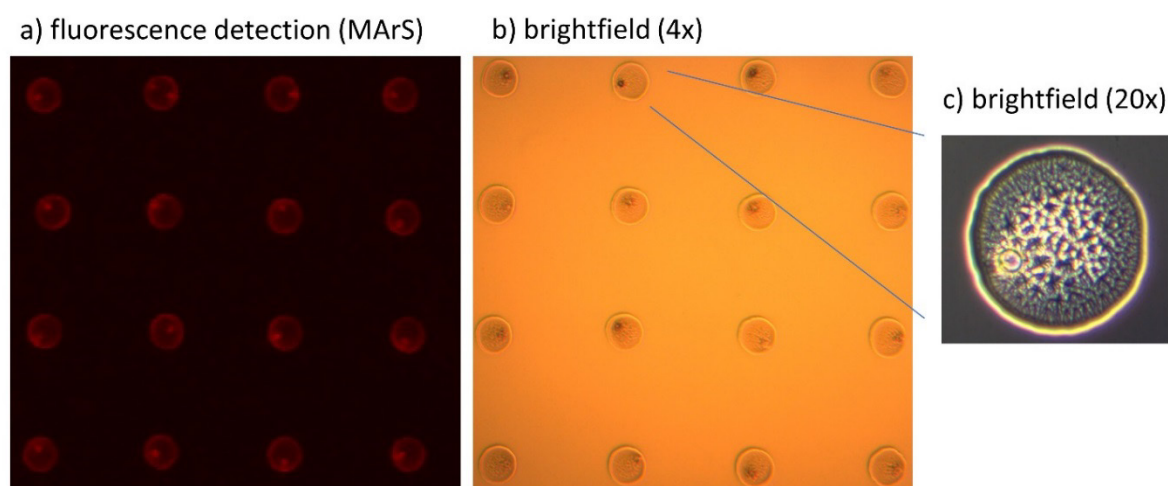


Figure 21 Micrographs of single cells arrayed in cell culture medium taken either via fluorescence imaging using (a) a microarray scanner and the autofluorescence of cells (normal scan with 10 μm resolution, mode: red-serial-red), (b) a brightfield microscope (4x), and (c) the same microscope at higher magnification (20x).

5.2.2.3 Optimization of the arraying procedure using polystyrene beads

Optimizations of the arraying process were carried out using 15 μm polystyrene beads, which present an ideal cell model due to the similarity in size and buoyancy compared to the target cell line (THP-1). After a first mapping experiment to define the ejection zone of the PDC, the so-called sedimentation zone must be defined manually. The size of the sedimentation zone depends on the time needed for the PDC movement from camera to target, and on the sedimentation velocity of beads, i.e. bead properties (size, density, shape) and buffer properties (density, viscosity). An overestimated sedimentation zone lowers bead recovery and overall arraying throughput, while an underestimated sedimentation zone increases spots with multiple beads. To define its optimal size, the sedimentation zone was gradually decreased until a rise in the number of spots with two or more beads were observed under a conventional microscope (16x magnification). In this way, an optimum size for the sedimentation zone was identified and used for the rest of these investigations. The bead concentration was expected to influence spotting throughput, recovery and single-bead occupancy of array spots. To elucidate the influence of bead concentration, a concentration series was spotted (three separate runs with

arrays of 400 spots for each concentration). Figure 22 shows the relationship between bead concentration and single-bead occupancy as well as arraying throughput.

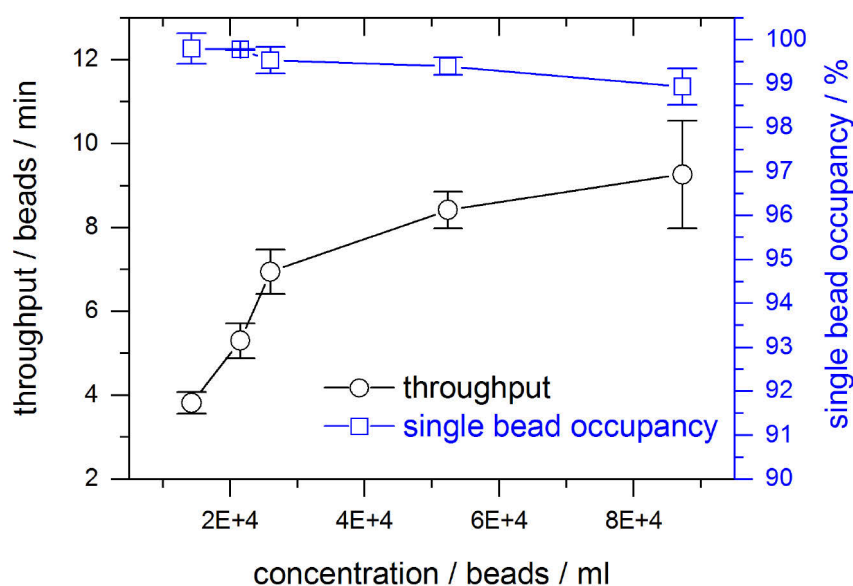


Figure 22 Throughput and single-bead occupancy in dependence of the concentration.

The number of spots without any bead was negligibly low with only two empty spots in a total of ~7,500 printed spots, while 38 spots contained two beads and none of the spots contained more than two beads. Empty spots were caused by the image recognition software recognizing a dirt particle as a bead due to a similar optical appearance in solution. However, after the dirt particles were dried and inspected under a microscope, they were clearly distinguishable from polystyrene beads. In principle, this problem could be overcome in the future by fluorescence assisted single-bead arraying. In these experiments, spots containing two beads were more prevalent and might be a consequence of 2D-vision: beads overlapping on the optical axis between LED and camera cannot be recognized as two separated beads. Depending on the degree of overlap of beads, some overlapping beads could be sorted out by applying stricter image recognition parameters such as a lower maximal area, elongation factor, and circularity factor in the software. With increasing concentrations, the likelihood of overlapping beads increases together with the fraction of spots containing two beads. Within the tested concentration range, the single-bead occupancy was consistently well above 99%, which is significantly better compared to any other existing single-bead arraying method fulfilling the requirements for further analysis by LA-ICP-MS. The recovery was assessed using the two lower concentrations by comparing the expected number of beads with the number of beads

spotted into the array. The expected number of beads was calculated by multiplying the bead concentration determined with a coulter counter (Scepter, Millipore) with the volume of 20 μL aspirated by the PDC before spotting. Recoveries of $99.6\% \pm 5.1\%$ for a concentration of 1.6×10^4 beads mL^{-1} and $95.6 \pm 3.5\%$ for a concentration of 2.2×10^4 beads mL^{-1} were determined. Recoveries for higher concentrations were not determined in this experiment, as arrays of 500 spots were filled completely. However, the recovery was expected to decrease with rising concentration due to the higher likelihood of multiple beads in the ejection and the sedimentation zone (scenarios C and D depicted in Figure 5).

The throughput of single cell arraying using sciFLEXARRAYER S3 platform is mainly limited by the time needed for back and forth dispenser movement between the camera station and the target array which takes roughly 2.4 s each way. Moreover, one dispensing and imaging cycle takes about 0.25 s, which leads to a theoretically limited throughput of about 12 cells min^{-1} . The practically achievable spotting throughput is lowered by the natural cell distribution following Poisson statistics and cell concentration. Within the studied concentration range, the spotting throughput showed a linear increase for lowest concentrations and plateauing at higher concentrations due to the increasing number of cells which had to be discarded. If the concentration would be increased further, the throughput would eventually decline together with a decrease in single cell occupancy (not shown) as the likelihood of having multiple cells in both the ejection and sedimentation zone would increase.

5.2.2.4 Validation of optimized arraying procedure for THP-1 cells

To verify the results obtained for 15 μm polystyrene beads, THP-1 cells were cultured as described in the main article and prepared for arraying by replacing the cell culture media after centrifugation (300 rcf, 3 min) with PBS buffer containing 1.3% paraformaldehyde for cell fixation. The cell suspension was diluted to a cell concentration of 7.3×10^4 cells mL^{-1} (measured using a coulter counter (Scepter, Millipore)). This concentration was found to represent a reasonable trade-off between high throughput and high single cell occupancy, see Figure 22. Using optimized parameters, five single cell arrays of 500 cells each were printed in five independent runs resulting in a throughput of 9.2 ± 0.6 cells min^{-1} (~ 550 cells h^{-1}) and a single cell occupancy of $99.0 \pm 0.8\%$. Moreover, the cell recovery was assessed by manually reviewing the micrographs of the first 100 dispensed cells of each of the five independent runs, which resulted in a cell recovery of $67 \pm 7\%$. The cell recovery is proportional to the cell concentration

and is expected to increase with lower concentrations but at the expense of throughput. The obtained cell recovery is significantly higher compared to transport efficiencies usually observed for pneumatic nebulization based single cell ICP-MS (up to 50%). More importantly, the selection of cells depends only on their statistical distribution in the PDC and thus is independent of cell size and representative for the cell population.

5.2.2.5 Conclusion

The novel piezo-acoustic single-cell arraying approach was successfully tested as a sample preparation method for LA-ICP-MS and was found to be suited to array a sufficient number of cells (>400) in order to achieve a statistically significant data set, as shown in section 5.1. Using optimized cell concentration, an unprecedented single-cell occupancy of >99% and decent arraying throughput (up to ~550 cells h⁻¹) were achieved, with a cell recovery of >67%. The overall transport efficiency of the approach is not cell-size dependent, which is advantageous compared to other single-cell arraying methods and conventional pneumatic nebulization single-cell ICP-MS. Further software-enabled developments regarding single-cell recognition and tracking within the PDC, as well as hardware-based developments like a faster axis systems or fluorescence detection of cells and cell markers have the potential to increase the instrument's usability, its figures of merit and versatility further.

5.3 Establishing sc-ICP-MS methods and testing of cell tagging protocols

For a final proof of principle experiment, it was the goal to quantify elemental markers in THP-1 cells. For that, the same two interesting elemental dyes which were already successfully used for staining of adherent 3T3 cells, mDOTA-Ho and Ir-DNA-intercalator, see chapter 5.1. The established tagging protocols needed to be adapted from cells which grow adherent to glass slides to suspension cells. Unfortunately, in this development period no access to a working LA system was possible due to recurrent instrumentation problems. The introduction of complete cells into the ICP was chosen as a readily available alternative, see section 2.1.2.1, and sc-ICP-MS was established as an alternative sample introduction method. Methods to measure nanoparticles using the popular sp-ICP-MS mode were already established in Dr. Jakubowskis' group (BAM division 1.1) and served as a starting point.⁷⁷⁻⁷⁹

First tests were carried out using a quadrupole ICP-MS (iCAP Q, Thermo Fisher Scientific) with established methods for nanoparticle analysis. This instrument is equipped with a sample introduction system for conventional liquid ICP-MS analysis, i.e. cyclonic quartz spray chamber and concentric PFA nebulizer (400 $\mu\text{L min}^{-1}$ nominal sample flow rate). The sample introduction transport efficiency for gold nanoparticles (60 nm, NIST) was determined using established methods to $\sim 3\%$.⁷⁷ To test whether this sample introduction system works as well for bigger particles like cells, Eu doped polystyrene beads (CyTOF[®] calibration beads, Fluidigm) with a diameter of $1.2 \pm 0.4 \mu\text{m}$ (determined by DLS measurements ($n=3$) using a Zetasizer Nano ZS, Malvern Instruments Ltd.) were analyzed, see Figure 23. First results were very promising, as a transport efficiency of 2.9% was determined, which agrees well with the transport efficiency of nanoparticles. Moreover, the sp-ICP-MS intensity distribution of particles (mean intensity of 3700 counts, 11% RSD) agreed well with mass cytometry data reported in the manufacturer certificate of analysis (Lot: P13J2704; mean intensity of 5200 counts, 16% RSD).

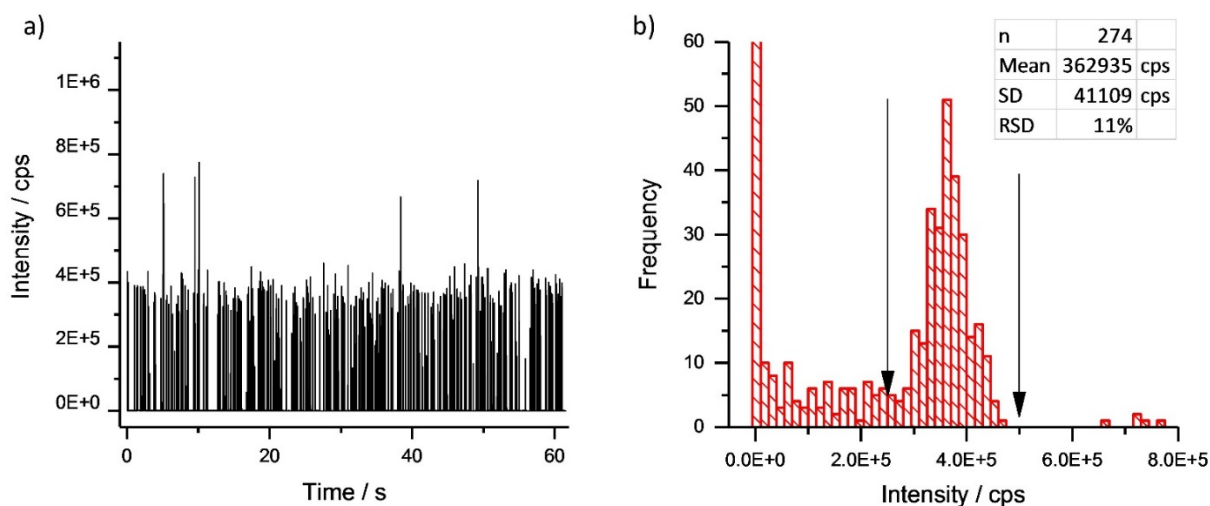


Figure 23 sp-ICP-MS measurement of micrometer sized Eu doped polystyrene CyTOF[®] calibration beads (3.3×10^5 beads mL^{-1} , Fluidigm) on a quadrupole ICP-MS (iCAP Q, Thermo Fisher Scientific). (a) shows the time-resolved measurement of ^{153}Eu (dwell time 10 ms), (b) shows the resulting intensity distribution and statistics of the analyzed peak (borders are marked with black arrows).

Next, the goal was to analyze THP-1 cells using the same approach. First tests to measure THP-1 cells tagged with Ir-DNA-intercalator and mDOTA-Ho failed, as only background was visible. The transport efficiency of single THP-1 cells was determined using a naturally occurring element with a sufficiently high content, to ensure that cells are transported to the plasma. Sulfur as a naturally occurring element in proteins was used as an elemental cell marker for THP-1 cells.^{XI} Surprisingly few peaks were observed for that measurement considering the used cell concentration of 5×10^5 cells mL^{-1} , see Figure 24, which would result in a transport efficiency of only $\sim 0.003\%$. To confirm plausibility of this measurement, results were compared to recently published literature. In a recent study, different trace elements (including sulfur) were successfully quantified in three mammalian cell lines by applying sp-ICP-MS quantification methods, see Figure 24 (b, c).⁸⁰ If the same quantification approach is applied to the performed measurement using a single particle calculation tool,⁸¹ a sulfur content of 2.9 ± 1.4 pg per single cell was calculated, which is in agreement with published values (2 to 3 pg per cell).⁸⁰

^{XI} Experiments were carried out together with Nora Lemke (BAM, Division 1.1).

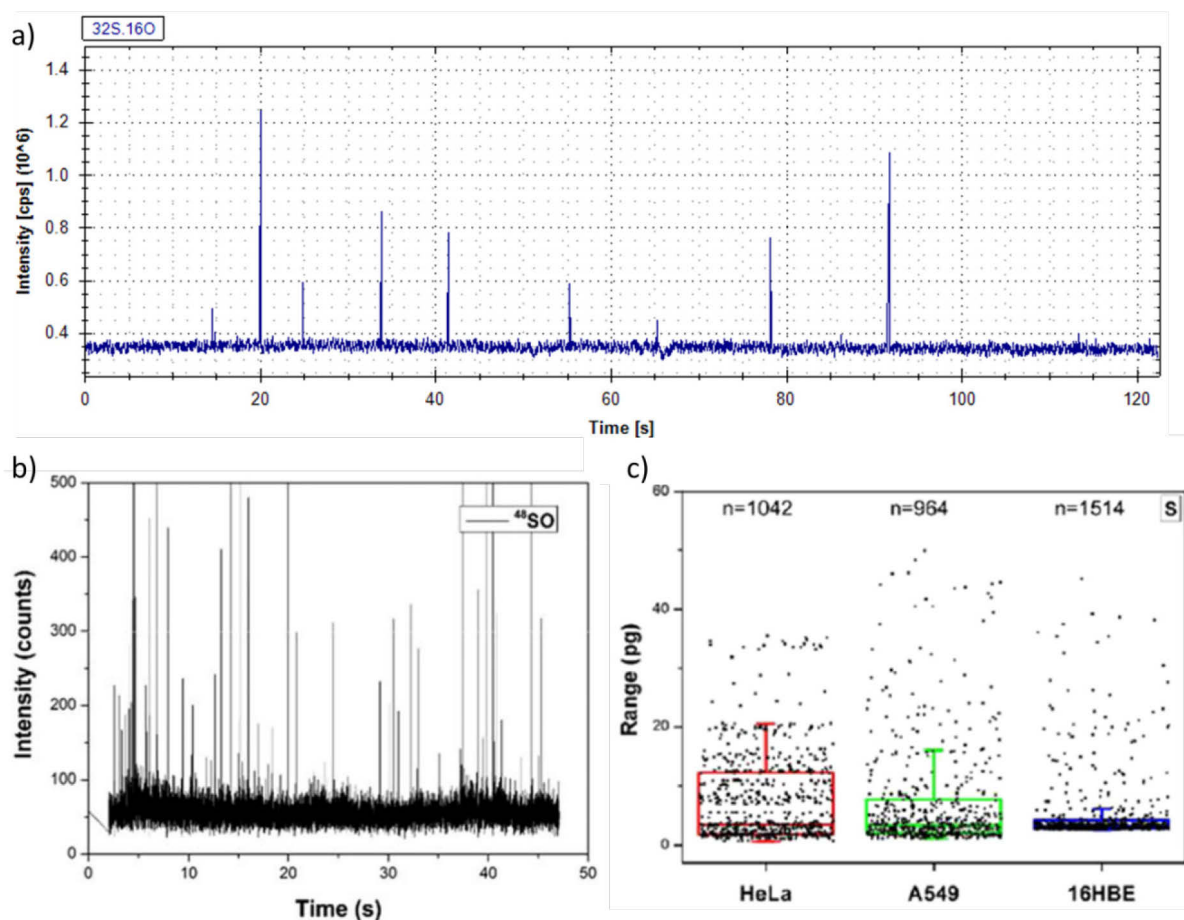


Figure 24 (a) sc-ICP-MS measurement of sulfur content in single THP-1 cells (5×10^5 cells mL^{-1}) by using oxygen as reaction gas to measure the interference-free oxygen adduct ^{48}SO . Parameters used to estimate sulfur content: dwell time 10 ms, transport efficiency 3% (for bulk solution), ^{48}SO sensitivity for inorganic dissolved standard solution 300 cps $\mu\text{g L}^{-1}$; sample flow rate to nebulizer 0.31 mL min^{-1} . The time-resolved ICP-MS measurement graph was exported from the iCAP Qs operation software (Qtegra, Thermo Fisher Scientific). (b, c) For comparison and plausibility check: Recently published measurement of sulfur content in different mammalian cell lines using sc-ICP-MS. Adapted from ref.⁸⁰ with permission of Springer.

To obtain sc-ICP-MS data with meaningful statistics, 5×10^7 cells would be required for each test. It would be very costly and laborious to culture and handle cells at that scale for method development purposes, as several T-75 cell culture flasks would be required to generate the data for each experiment. In Figure 24 (b) the sc-ICP-MS sulfur measurement of a cell suspension with a concentration of 1×10^6 cells mL^{-1} is shown, illustrating the better transport efficiency of the high efficiency cell introduction system (HECIS) used by Wang et al., which consisted by a self-built heated single pass spray chamber.⁸⁰ Consequently, it was decided that a more effective sample introduction system for single cells should be acquired and its usage should be established to enable effective testing of cell tagging protocols with sing-cell resolution.

5.3.1 A sample introduction system with high transport efficiency for sc-ICP-MS

Only two dedicated sample introduction systems were commercially available at that time, which both were sold as a single-cell sample introduction system for use in combination with the manufacturer's ICP-MS devices. The most widely used single-cell sample introduction system is used in combination with CyTOF[®] devices (Fluidigm). Recently, a novel *Single-cell Sample Introduction Kit* was introduced for NexION 1000/2000 ICP-MS devices (Perkin Elmer). Herein, it was decided to rely on the CyTOF[®] single-cell sample introduction system because of its superior transport efficiency, see section 2.1.2.1.

The acquired CyTOF[®] single-cell sample introduction system encompassed a normal nebulizer (nominal flow rate 40 $\mu\text{L min}^{-1}$, Meinhard) and a dedicated single-pass spray chamber. For operation, the required accessories differ from those needed for commonly used liquid sample introduction systems: (i) no waste needs to be drained from the spray chamber, as this is a total consumption system, (ii) the spray chamber needs to be heated to $\sim 200^\circ\text{C}$ in order to heat up (iii) an additional Ar gas flow which is used to guide and desolvate large droplets on the way to the ICP. Accordingly, a customized heating device was constructed, see Figure 25 (a).^{XII} The heating device is operated manually by application of heating voltage, while an impedance-based sensor allows for manually controlling the temperature by tuning the heating voltage. Because the Element XR (Thermo Fisher Scientific) was the only ICP-MS device which featured an additional Argon gas line with controllable flow and the option to ramp up the gas flow after the plasma is switched on, all further experiments were conducted using Element XR. Figure 25 (b) shows the installed system with connected gas lines, ready for operation. A procedure to safely switch on and off was elaborated, see appendix section 7.2.1.

^{XII} Construction of the heating system by Andreas Schulz and Jens Pfeiffer (BAM division 1.1) is acknowledged.

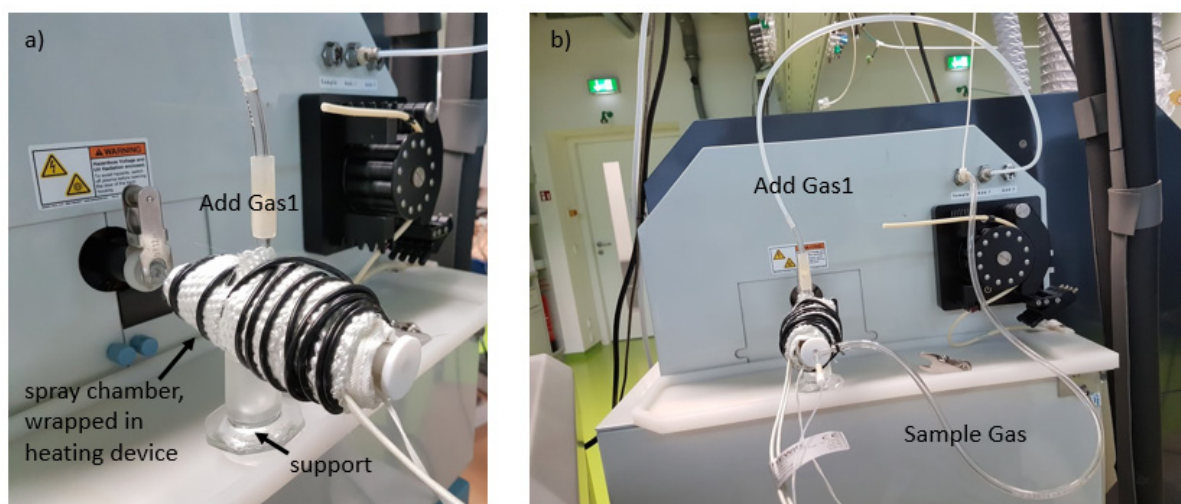


Figure 25 (a) Spray chamber and heating system connected to Element XR (Thermo Fisher Scientific). (b) System with installed nebulizer and connected Add Gas1 and sample gas.

Tuning of the new sample introduction system was performed in a similar way as usually performed for conventional sample introduction systems using a standard solution with $1 \mu\text{g L}^{-1}$ In (Tune B standard solution, Thermo Fisher Scientific). All instrument parameters are tuned for maximum ^{115}In sensitivity and signal stability, including the novel parameter Add Gas1 flow rate. It became clear that the setup allowed to be tuned to unusual high intensities, owing to the high achievable transport efficiency. Depending on the tuning conditions, the observed mass peak showed an unfamiliar shape, as the usually observed flat top of the ^{115}In mass peak was not as flat as usual, see Figure 26, left. This unfamiliar mass peak shape was attributed to a quite unstable signal, and the tuning of Add Gas1 was found to have a quite high impact on signal intensity and stability. Moreover, owing to the very high and unstable intensities, an overload effect of the detector (operated in counting mode) was observed for intensities higher than 2×10^6 cps. When the detector was overloaded, recording of the mass peak stopped, see red arrow in Figure 26, right. The ‘tuning mode’ of the ICP-MS device does not allow to use the so-called ‘dual detection mode’, which in case of a too high intensity switches automatically from counting mode to the analog mode. Accordingly, a measurement series was performed to optimize the new and critical parameter Add Gas1 flow rate using a $10 \mu\text{g L}^{-1}$ Eu standard solution.

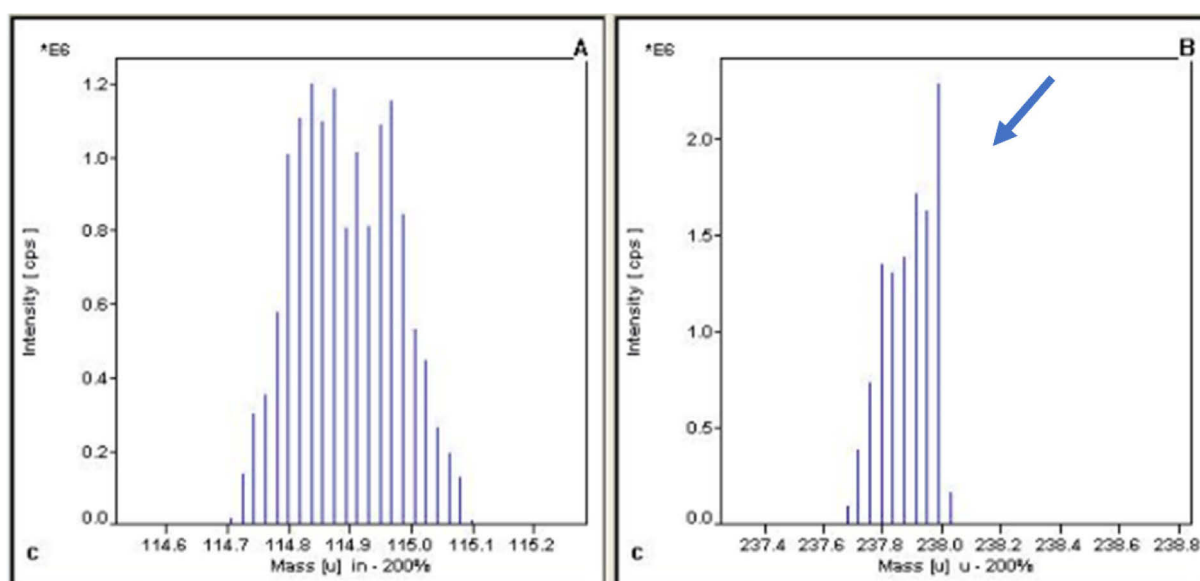


Figure 26 Screenshot from tuning window of Element XR. Left: Unfamiliar noisy peak shape, observable in the so-called flat top region. Right: As intensity gets too high, recording of the mass peak stops, see red arrow.

Figure 27 shows the result of tuning the Add Gas1 flow rate. Maximum signal intensity was observed for an Add Gas1 flow rate of 1.6 L min^{-1} , while standard deviation was maximal for an Add Gas1 flow rate of 1.4 L min^{-1} . For lowest detection limits, the signal to noise ratio has to be minimized. The signal stability was found to have two equally low local minima with an RSD of 9% for Add Gas1 flow rates of 1.1 L min^{-1} and 1.6 L min^{-1} . Since the Add Gas1 flow rate 1.6 L min^{-1} has a considerably higher signal, this flow rate seemed to be the optimum. Nonetheless, it was unclear which processes lead to these observations, and the Add Gas1 flow rate optimization experiment was repeated in sp-ICP-MS mode using CyTOF[®] calibration beads.

For that, a novel sp-ICP-MS data acquisition method based on Shigeta's approach⁸² was used to minimize the Element XR settling times, see appendix section 7.2.2. Using the previously optimized parameters, the Add Gas1 flow rate was optimized for the detection of CyTOF[®] calibration beads. The resulting average bead intensities and the measurement precision are shown in Table 10 along with the number of detected beads. Again, two local minima for the RSD could be found for Add Gas1 flow rates of 1.1 L min^{-1} with 22% and 1.6 L min^{-1} with 17%, whereby for 1.6 L min^{-1} a six times higher intensity was measured. However, for 1.1 L min^{-1} fourteen times more bead events were detected. For a better visual representation of the data, histograms are shown for each Add Gas1 flow rate in Figure 28.

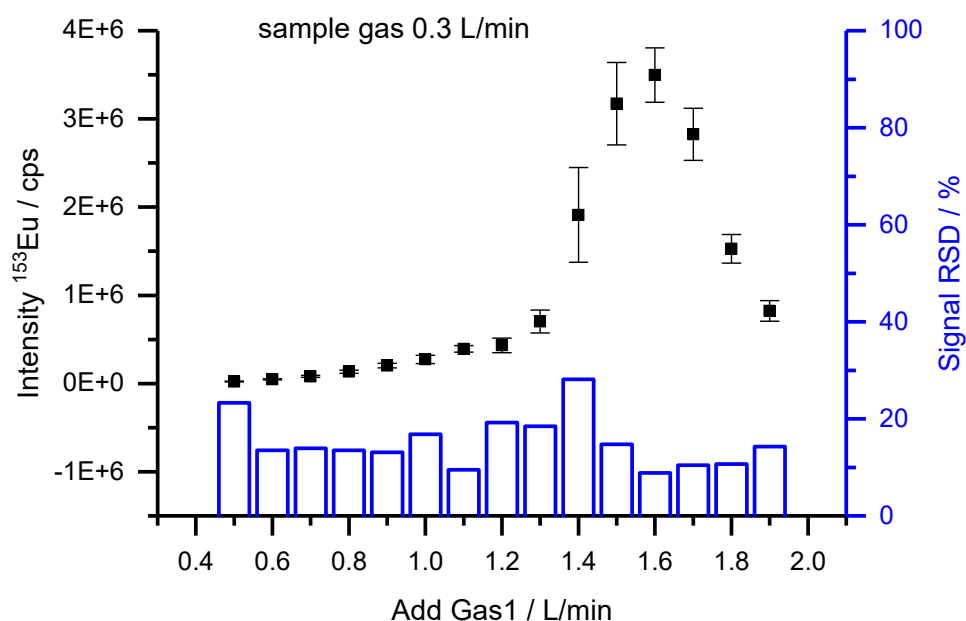


Figure 27 Tuning of the Add Gas1 flow rate using a liquid standard solution ($10 \mu\text{g L}^{-1}$ Eu). Parameters used in this investigation: sample gas flow rate 0.3 L min^{-1} , dual detection mode, detector integration time 10 ms, 7000 runs (i.e. measurements).

Table 10 Result of Add Gas1 flow rate optimization experiment for sp-ICP-MS using CyTOF[®] calibration beads, in which all intensity values >20 counts were detected as single bead event. Number of events equals the sum of all observed bead events. All intensities in counts.

Add Gas1 / L min ⁻¹	0.6	0.7	0.8	0.9	1	1.1	1.2	1.3	1.4	1.5	1.6	1.7	1.8	1.9
Avg. bead intensity	57	91	143	225	337	487	627	995	2204	3061	3045	2193	1571	699
Bead intensity SD	15	23	34	62	83	276	152	296	662	698	510	615	508	289
Bead intensity RSD	27%	25%	23%	28%	25%	22%	24%	30%	30%	23%	17%	28%	32%	41%
Number of events	483	486	583	580	561	598	609	523	69	43	43	71	225	541

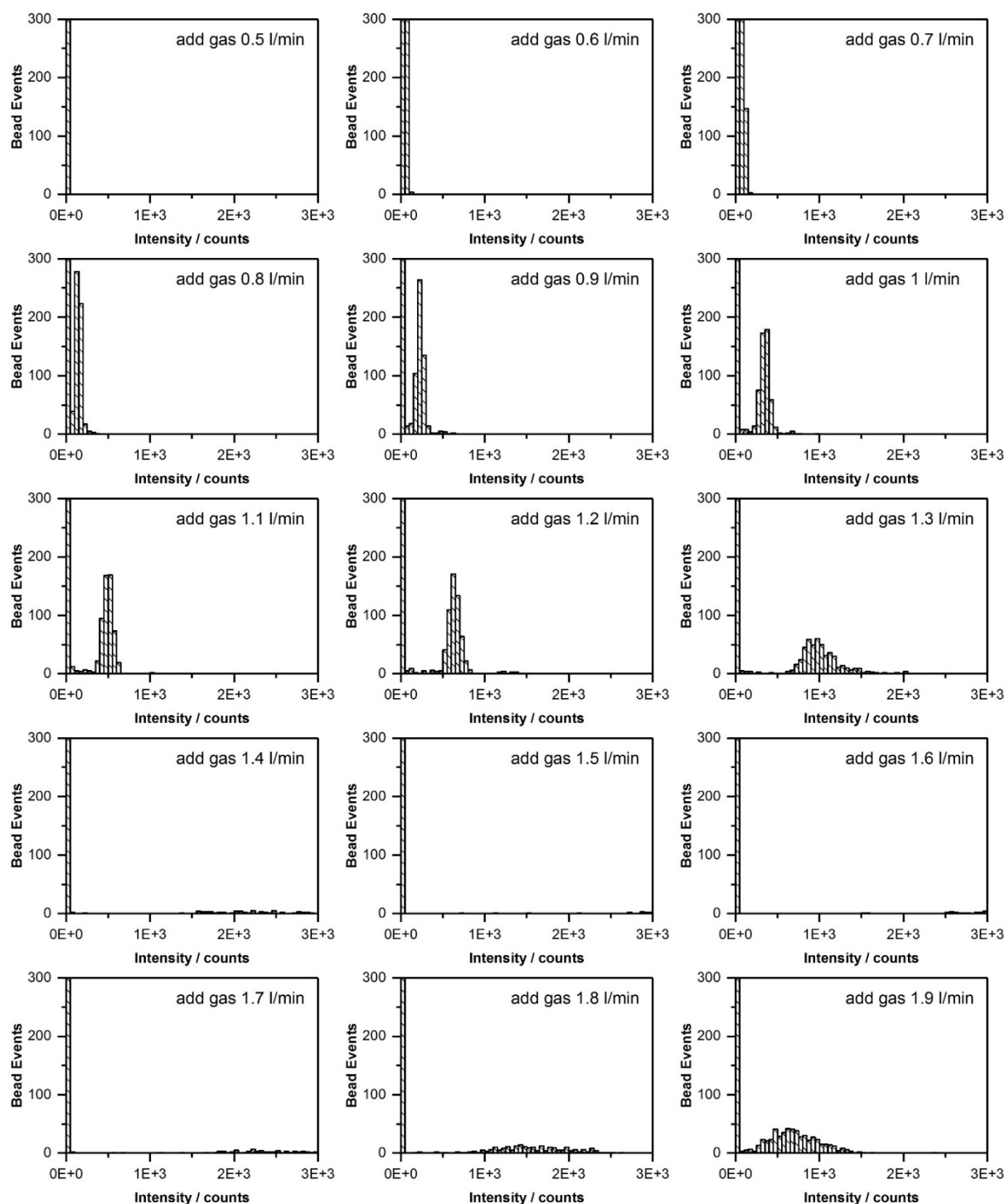


Figure 28 Add Gas1 flow rate optimization experiment for sp-ICP-MS using CyTOF[®] calibration beads.

As the Add Gas1 flow rate increases, the sensitivity for ^{153}Eu in beads increases, but the rise in sensitivity is accompanied by peak broadening and a decrease in transport efficiency. At an Add Gas1 flow rate of 1.5 L min^{-1} , the obtained intensity is maximal, but almost no more particles reach the ICP. If the flow rate is further increased, the bead intensity decreases, and the transport efficiency increases again. This suggests that very high bead intensities correspond to a

measurement of several beads at once. On the other hand, at lower Add Gas1 flow rates a proportionality to the average bead intensity was observed while the transport efficiency stayed approximately constant. These effects are thought to be related on the one hand with specific flow conditions and with a shift of the plasma zones for evaporation, atomization and ionization on the other hand. However, the underlying reasons of this behavior are not clear and would need further investigation of the flow patterns causing the observed effect, using e.g. a highspeed camera and particle tracking. Within the scope of this optimization experiment it was decided to optimize only the main peak using customized borders to exclude incompletely recorded beads and multiple beads per integration time (compare Figure 3). Table 11 shows the results from Table 10 restricted to the main peak (with peak specified borders of minimal and maximal intensity), whereby flow rates greater than 1.4 were excluded as too high flow rates resulted in a very limited transport efficiency and large bead intensity RSDs. An optimum was identified at an Add Gas1 flow rate of 1.2 L min^{-1} , with the highest transport efficiency, a high average bead intensity and the lowest observed RSD. Moreover, the bead intensity RSD determined herein agrees very well with the one determined using optimized parameters on the iCAP Q equipped with a conventional sample introduction system. Noteworthy, sp-ICP-MS measurements on properly tuned iCAP Q and Element XR devices (both Thermo Fisher Scientific) enabled a more precise measurement compared to the precision reported by the manufacturer measured on a CyTOF[®] devices.

It should be mentioned that the average bead intensity measured under optimal flow conditions in Table 11 was significantly lower compared to previous experiments (compare Figure 23). The reason for that were not yet optimized parameters for the ion lenses and mass separation device, which were optimized only in the next step. However, these parameters are independent and after their optimization an average bead intensity of $\sim 10^4$ counts was achieved, which agrees well with the expected value (roughly twice the intensity of a CyTOF[®] device, compare Table 1).

Table 11 Result of Add Gas1 flow rate optimization experiment for sp-ICP-MS using CyTOF[®] calibration beads (same experiment as in Table 10), in which only the main peak corresponding to single beads with minimal and maximal intensity borders was analyzed. All intensities in counts.

Add Gas1 / L min ⁻¹	0.6	0.7	0.8	0.9	1	1.1	1.2	1.3	1.4	1.5	1.6	1.7	1.8	1.9
Min. intensity	20	40	60	120	150	300	400	600	-	-	-	-	-	-
Max. intensity	120	150	220	320	525	700	900	1550	-	-	-	-	-	-
Avg. bead intensity	57	92	144	227	346	496	639	1002	-	-	-	-	-	-
Bead intensity SD	15	19	28	35	53	57	68	182	-	-	-	-	-	-
Bead intensity RSD	27%	20%	19%	16%	15%	12%	11%	18%	-	-	-	-	-	-
Number of events	483	470	548	524	517	549	558	472	-	-	-	-	-	-

5.3.2 Testing of cell tagging protocols^{XIII}

Tagging of suspension cells using the two elemental dyes Ir-DNA-intercalator and mDOTA-Ho can be regarded as an established standard method in mass cytometry laboratories. The Ir-DNA-intercalator is typically added in every mass cytometry analysis as it is used to discriminate single cells from cell agglomerates via signal length and intensity.⁸³ The mDOTA reagent is well-known in mass cytometry, as it was introduced as the first reagent enabling mass-tag based cell barcoding (MCB), an approach which is used to improve the efficiency and comparability of assays in which cells from different sources should be analyzed. MCB uses a cocktail of different antibodies to stain all samples simultaneously within a single tube, ensuring that all samples are exposed to the same antibody concentration at the same cell density.⁸⁴

Next, it was the goal to optimize the intensity of both dyes for the high throughput LA-ICP-TOF-MS analysis of a cell array, based on published protocols and experience from dying of adherent cells using these two reagents. The variables which should be optimized were the conditions for cell fixing and the incubation concentration and time for both dyes. Table 12 shows the elaborated initial protocol which served as a starting point. A noticeable difference from other protocols used for suspension cells is the lack of cell permeation step using

^{XIII} Assistance of Sabine Flemig (BAM division 1.1) in cell culturing and testing of cell tagging protocols is greatly acknowledged

methanol, as cell permeation previously lead to lowered sensitivity for adherent cells,⁶⁵ and makes cell handling more difficult due to a decrease in cell density. Moreover, it was shown by Zhu *et al.* that DOTA can be complexed with lanthanide ions in various buffers. If $\text{pH} \geq 6$ is ensured, the reaction was found to be very fast as it was completed in less than 4 min.⁸⁵ For synergetic reasons mDOTA was complexed with Ho in PBS buffer ($\text{pH } 7.2$).

Table 12 Protocol used for tagging of cells with Ir-DNA-intercalator and mDOTA-Ho; with abbreviations: room temperature (RT), phosphate buffered saline (PBS), relative centrifugal force (rcf), x = number of millions of cells used for the experiment (determined using Scepter[®] (Merck KGaA)).

1. Transfer $x \cdot 10^6$ cells to 50 mL centrifuge tube
2. Centrifuge (5 min @ 300 rcf), discard supernatant
3. Resuspend cells in x mL 4% paraformaldehyde
4. Incubate 15 min @ RT
5. Centrifuge (5 min @ 300 rcf), discard supernatant
6. Resuspend in x mL 250 nM mDOTA-Ho (diluted in PBS)
7. Incubate 15 min @ RT
8. Centrifuge (5 min @ 300 rcf), discard supernatant
9. Wash 2 times: Resuspend in 2x mL PBS, centrifuge (5 min @ 300 rcf), discard supernatant
10. Resuspend in 3 mL 125 nM Ir-DNA-Intercalator (diluted 1:1, PBS to Roti Histofix)
11. Incubate 60 min @ RT
12. Centrifuge (5 min @ 300 rcf), discard supernatant
13. Wash 3 times: Resuspend in 2x mL PBS; Centrifuge (5 min @ 300 rcf), discard supernatant
14. Right before further analysis:
Wash: Resuspend in 2x mL water; Centrifuge (5 min @ 300 rcf), discard supernatant
Resuspend in $x/2$ mL water to reach a target concentration of $x \cdot 10^6$ cells mL^{-1}

After tagging of cells using the proposed protocol shown in Table 12, cells were analyzed using the newly established sc-ICP-MS sample introduction system coupled to the Element XR. Surprisingly, these measurements showed for both dyes that cells were not tagged with sufficient efficiency such that no cell events could be distinguished from the background. Varying incubation time and concentration of both dyes and paraformaldehyde did not improve tagging efficiency. Finally, two simple mistakes were identified as the reason for the failure of the applied protocol. Firstly, using MALDI-TOF-MS^{XIV} it was shown that mDOTA is not able to complex Ho in PBS buffer, see Figure 29. After incubating equimolar concentrations of mDOTA and HoCl_3 in either PBS, water (purified to $18.2 \text{ M}\Omega$), or ammonium acetate (45 mM, $\text{pH } 6.5$) for 30 min, samples showed a distinctly different complexation behavior. While no mDOTA-Ho complex was formed in PBS buffer, approximately equimolar

^{XIV} Timm Schwaar and Sabine Flemig are greatly acknowledged for assistance in MALDI-MS measurements.

ratios of mDOTA and mDOTA-Ho could be observed after incubation in water. Only if ammonium acetate was used as buffer, mDOTA was completely complexed with Ho, such that only the peak for the product mDOTA-Ho was observed. Therefore, from now on ammonium acetate served as buffer for mDOTA lanthanide complexing. Secondly, it was suspected that the currently used Ir-DNA-intercalator stock exceeded its shelf life. Thus, a fresh stock of Ir-DNA-intercalator was ordered, which solved the problem. The formerly used Ir-DNA-intercalator stock was probably damaged due to recurrent freeze-thaw cycles. Accordingly, it was decided to aliquot the stock solution upon arrival to amounts needed for a single experiment.

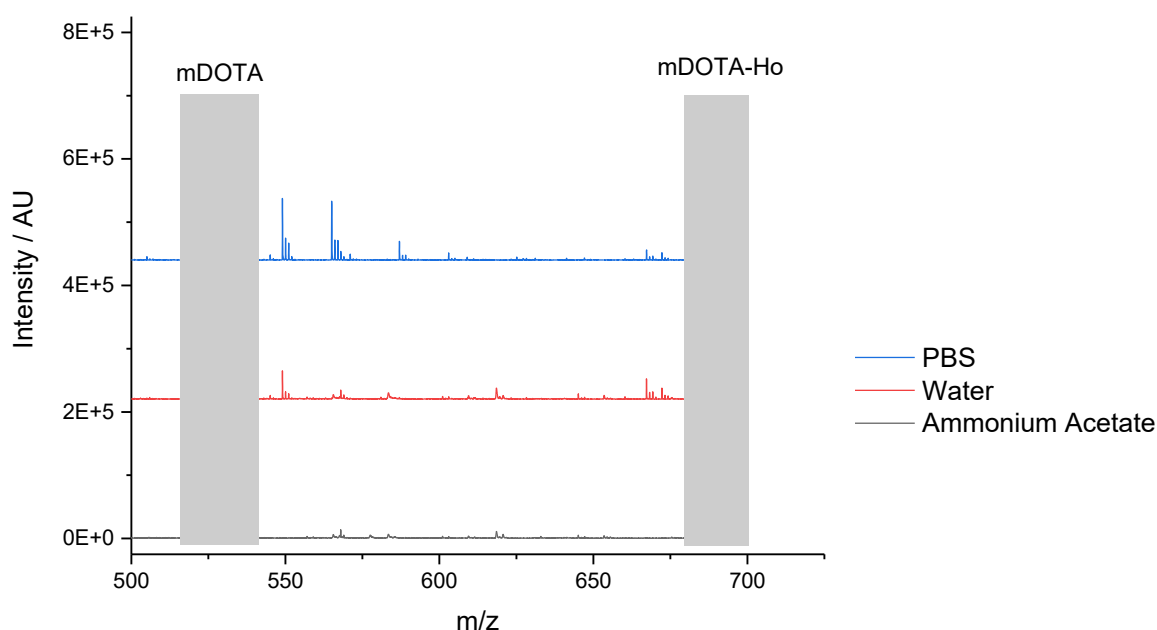


Figure 29 MALDI-TOF-MS measurement to test the suitability of different buffers to complex mDOTA with Ho to obtain mDOTA-Ho. For the analysis of mDOTA in PBS two peaks with comparatively high intensity as [mDOTA] can be seen at masses [mDOTA +22] and [mDOTA +38], corresponding to sodium and potassium adducts.

After the problems were solved for both elemental dyes, a batch of THP-1 cells was successfully dyed using the tested protocol in Table 12. Dyed cells were analyzed using sc-ICP-MS and, at the same time, an aliquot was subject to single-cell arraying for subsequent LA-ICP-TOF-MS analysis, see chapter 5.4. Histograms of elemental dye intensity per single cell obtained using sc-ICP-MS are shown in Figure 30 (top). For Ir-DNA-intercalator (left), a clear main peak with an intensity of 2.5×10^3 counts is visible. This peak could not be baseline separated from the background and has a relatively long flat tail of higher intensities. For mDOTA-Ho (right), a considerably higher background was observed, and single-cell events were only visible as a flat

tail of the single peak observed for the background (see inset). To reduce the background, the remaining cell suspension was washed 3× using water and analyzed again, see Figure 30 (bottom). Unfortunately, about 95% of cells were lost during these additional washing steps. It is assumed that a slower sedimentation of cells in water was responsible for this surprisingly low cell recovery. At first this seems counterintuitive, as water has a lower density than the usually used PBS buffer and thus cells should be sedimenting faster. However, it was observed that fixed cells suspended in water show a distinguishable growth in volume after a few hours. This swelling was attributed to an influx of water into the cells due to osmotic pressure, leading to a reduced density and a slower sedimentation of cells. After washing, single-cell intensity distributions with significantly reduced background were obtained, such that the main peak of Ir-DNA-intercalator was almost baseline separated from the background and a peak for mDOTA-Ho began to take shape.

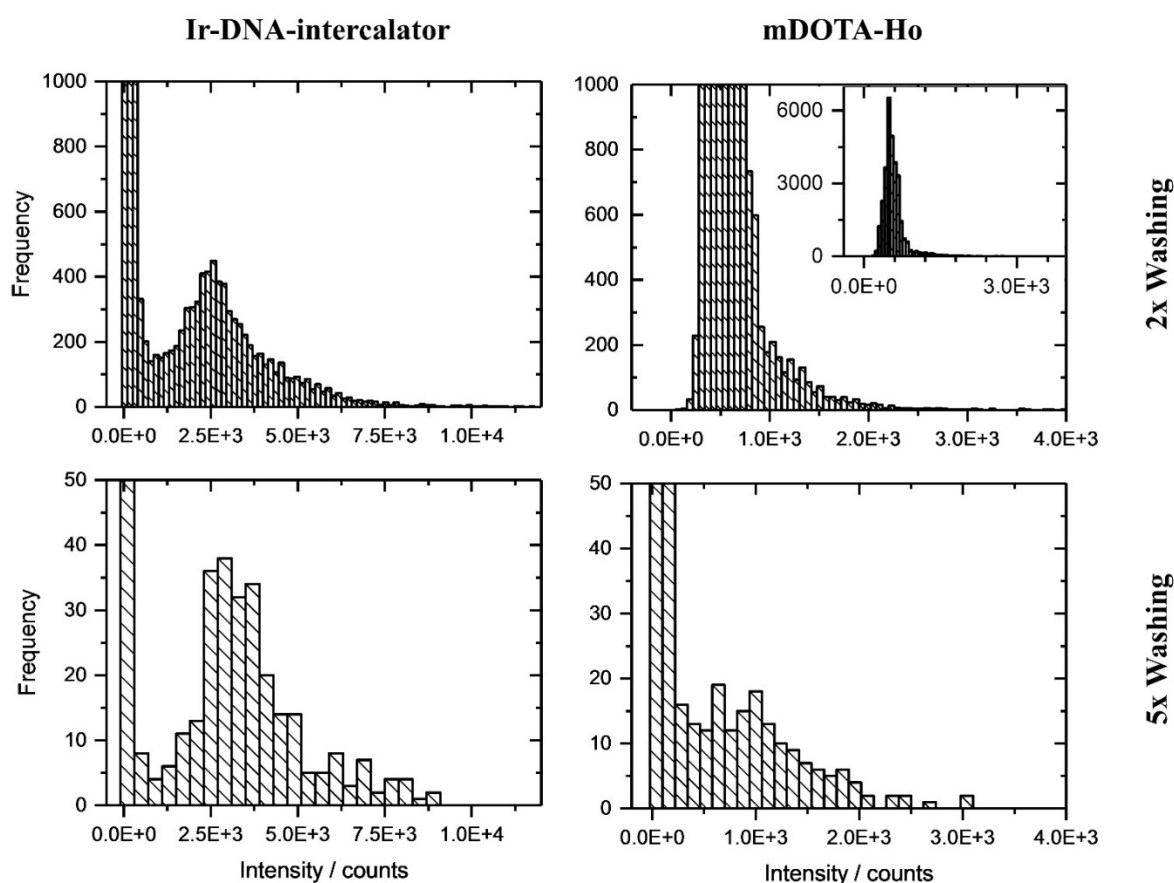


Figure 30 Histograms from sc-ICP-MS measurements of THP-1 suspension cells, which were died using the protocol in Table 12 (top) or three additional washing steps (bottom). On the left the histograms for the Ir-DNA-intercalator (^{193}Ir intensity) are shown, on the right the histograms for mDOTA-Ho are shown.

First steps to optimize the tagging protocol to obtain a higher mDOTA-Ho tagging degree of cells were made, but an increase of mDOTA-Ho incubation time and concentration did not lead to a satisfactory improvement of signal to noise ratios. This was surprising, as Bodenmiller *et al.* obtained single-cell intensities one to two orders of magnitude higher for a comparable suspension cell line (K652).⁸⁴ The major difference in tagging protocols was the fixation method: While in this study 4% paraformaldehyde was used, Bodenmiller *et al.* used in addition to 1.6% paraformaldehyde ice cold methanol. Resuspension of pelleted cells in ice cold methanol is a widely used approach to fix and permeate cells at the same time. Permeated cells allow for staining of intracellular antigens as pores are formed in the cell membrane to allow diffusion of antibodies into the cell. However, for the analysis of naturally occurring trace elements using LA-ICP-TOF-MS, such a permeabilization step would lead to losses of cell suspension liquid and proteins along with naturally occurring elements. Moreover, previous studies on mDOTA staining behavior by Herrmann *et al.* showed that cell permeabilization did not improve mDOTA staining.⁶⁵ To prevent losses of naturally occurring elements and obtain unaltered isotopic fingerprints of THP-1 cells, it was decided to not permeabilize cells. Later, it was discovered that the Nolan group had reported that cell permeabilization was considered as a crucial step for mDOTA based barcoding of cells.^{86, 87} Obviously, these findings and the findings by Herrmann *et al.* contradict each other. The major difference between the studies which lead to different observations was that Herrmann *et al.* investigated adherent cells instead of suspension cells. It remained unclear why permeabilization was considered necessary for suspension cells but did not lead to a significant increase of the tagging degree for adherent cells.

5.3.3 Conclusion

A high efficiency cell introduction system (HECIS) based on parts used for CyTOF[®] single-cell sample introduction was successfully constructed and optimized for usage with an ICP-SF-MS (Element XR). After a thorough optimization of gas flows, the HECIS transport efficiency was comparable with the transport efficiency reported for usage in combination with CyTOF[®] mass spectrometers with dedicated accessories and appliances. Using CyTOF[®] calibration beads, a ~50% better precision was measured regarding bead-to-bead intensity variation reported in the manufacturer's certificate of analysis (measured using a CyTOF[®] device). HECIS enabled testing of the elaborated cell tagging protocol via sc-ICP-MS, such that initial problems with reagent preparation and storage could be identified and overcome.

5.4 High throughput Laser Ablation ICP-TOF-MS and isotopic fingerprinting

So far, it was shown that the laser ablation mode SSA is preferable over imaging (chapter 5.1) and arraying of single cells was established to overcome the time intense manual targeting of single cells (chapter 5.2). In this chapter, these findings are combined and an array of THP-1 cells was prepared to quantify the two metal-dyes which were used to dye cells using the protocol developed and tested in chapter 5.3. Moreover, the used LA-ICP-MS was equipped with a time-of-flight (TOF) detector to enable detection of elements over the whole mass range simultaneously. The two metal-dyes were quantified on a single-cell level using arrayed droplets of the same dye of a known concentration mixed with Rhodamine B which was added to achieve a closer matrix-match with cells.⁴¹ For the first time, the fingerprint of endogenous elements in single cells was explored by ICP-TOF-MS. Finally, accumulation of Mg and P throughout the cell cycle was investigated by using the Ir-DNA-intercalator as a biomarker for the cell cycle status.

5.4.1 Single-cell arraying

For a proof of principle study, THP-1 cells were fixed and dyed with mDOTA-Ho and Ir-DNA-intercalator (see sections 4.3 and 0) for arraying using the piezo-acoustic arraying process (see section 5.2.2). After aspiration of cell suspension into the PDC and automated mapping of the PDC ejection zone, the sedimentation zone was optimized empirically. For arraying, a volume of 20 μL cell suspension (2×10^6 cells mL^{-1}) was aspirated into the PDC. Under the defined conditions, about 200 positions were filled per hour. After 921 of 1,000 array positions were filled, no more cells were in the PDC, resulting in a cell recovery of $\sim 2\%$ (number of arrayed single cells divided by number of cells aspirated into PDC). Spots which were hosting no cell were negligibly low ($< 1\%$). Such empty spots were caused by the image recognition software recognizing particulate matter as a cell due to their similar optical appearance in suspension. However, after the droplet dried, the particulate matter was clearly distinguishable from cells by visual inspection via brightfield microscopy. In principle, this problem could be overcome in the future by fluorescence assisted single-cell arraying. While $\sim 80\%$ of the spots hosted exactly one cell, $\sim 19\%$ of the spots hosted more than one cell. Spots hosting two, or even more cells, are the consequence of unoptimized image recognition parameters and 2D-vision. Cells overlapping on the optical axis between LED and camera cannot be recognized as two separated cells. Depending on the degree of cells' overlap, stricter image recognition parameters such as a lower maximal area, elongation and circularity factor could be used to automatically reject

cell debris or agglomerates. Figure 31 shows a 4×4 subset of the THP-1 cell array, illustrating the accuracy of single-cell isolation and positioning precision required for subsequent automated LA. In these preliminary tests, the concentration of cell suspension and image recognition parameters were not yet fully optimized, which resulted in poor cell recovery and occurrence of double cell events per position. Despite the sub-optimal isolation accuracy, the number of spots containing exactly one single cell was sufficient for a proof of principle LA-ICP-TOF-MS study. Additionally, all positions containing none or more than one cell were discarded from this study after visual inspection.

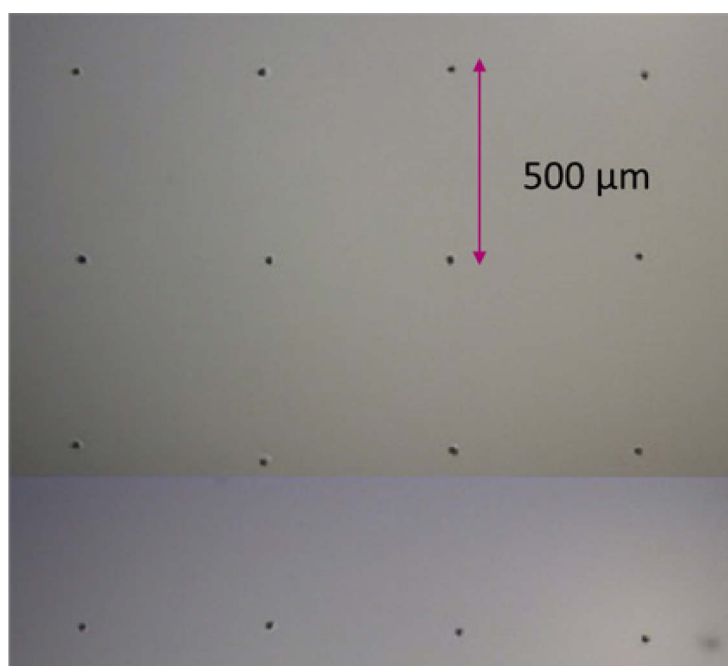


Figure 31 Micrograph of a 4×4 subset of the cell array, taken with the camera of the LA platform.

5.4.2 LA-ICP-TOF-MS measurement

For ablation of the cell array, a LA system with very fast washout times was coupled to an ICP-TOF-MS instrument which can measure elements of the whole mass range quasi-simultaneously (see chapter 4.4.3 for details). First, a grid of spots with a center to center distance of 500 μm was aligned onto the cell array. Visual inspection of the aligned grid in the software of the LA-system revealed that a laser spot size of 150 μm was sufficiently large to include every cell in the corresponding spot. Fluence and number of laser pulses applied per cell were optimized such that every cell was ablated completely, but no Si background from the glass slide was observed. Figure 32 shows the transient LA-ICP-TOF-MS signals of several elements from single spot analysis of four individual cells (see appendix section 7.3 Figure 41

for detailed single-element plots). The ICP-TOF-MS signal of a single ablated cell lasted <180 ms. Single cells could be ablated and measured with a throughput of ~1 cell per second, which was limited by the LA-system stage movement speed. Signals from cells were identified using the ^{193}Ir -DNA-intercalator signal and were integrated for all isotopes. To exclude multiple cell events per spot, cell occupancy of array spots was verified visually using micrographs from the LA platform and all spots which did not contain exactly one single cell were excluded. In total, 562 single cells were measured, which can provide higher statistical significance as discussed earlier (see chapter 5.1.3.2)

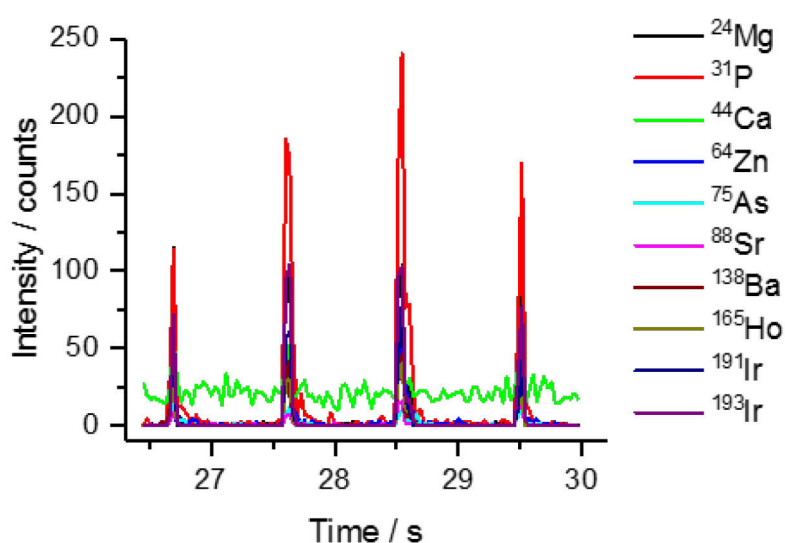


Figure 32 Transient signals of selected naturally occurring isotopes and metal-dyes measured by LA-TOF-ICP-MS from four individual single cells.

5.4.3 Blank correction

Signals from single cells need to be corrected for background signals, which originate from the gas blank, from ablation of the glass slide coating, and most importantly from the liquid embedding a dispensed cell (droplet blank). The contribution of gas blank intensities was estimated by integrating the signal over intervals of 270 ms prior to ablation of cells. To assess the background from glass slide coating and cell suspension liquid, droplets of cell suspension supernatant were ablated. Droplets of cell suspension supernatant without cells are representative for the background, as a THP-1 cell with a diameter of ~16 μm contributes insignificantly with only ~1% to the dispensed droplet volume (~330 pL). Supernatant was collected from the original cell suspension used for the analysis after allowing for cell sedimentation for 2 h. The droplet blank array was measured in the same way as the cell array

and peaks from individual spots (n=60) were integrated using the ^{23}Na signal for peak recognition. Gas blank, droplet blank and mean cell intensities (before blank correction) are shown in Table 13. Droplet blanks of the elemental dyes Ir and Ho were very close to zero, while the droplet blanks for most other endogenous elements were a bit elevated, if compared to the gas blank, but still relatively low. All single-cell intensities were blank corrected using the droplet blank.

Table 13: Signal intensities of gas blank, blank from ablation of dried droplets containing cell suspension supernatant only (droplet blank, n=60) and single cells before blank correction (n=562) given in counts. Percentages of cells in which the isotope X was detectable are listed as %>LOD.

	^{23}Na	^{24}Mg	^{27}Al	^{31}P	^{32}S	^{44}Ca	^{55}Mn	^{56}Fe
gas	1000 \pm 36	2 \pm 2	7 \pm 3	8 \pm 3	7147 \pm 155	75 \pm 9	7 \pm 3	330 \pm 19
droplet	4332 \pm 657	18 \pm 7	12 \pm 5	16 \pm 7	11948 \pm 184	172 \pm 21	9 \pm 3	418 \pm 25
cells	21091 \pm 2192	190 \pm 183	44 \pm 79	374 \pm 149	12527 \pm 202	225 \pm 18	18 \pm 6	526 \pm 198
% >LOD	100%	99%	17%	100%	23%	22%	6%	12%
	^{65}Cu	^{66}Zn	^{75}As	^{88}Sr	^{138}Ba	^{165}Ho	^{191}Ir	^{193}Ir
gas	1 \pm 1	4 \pm 2	1 \pm 1	3 \pm 1	0 \pm 0	0 \pm 0	0 \pm 0	0 \pm 0
droplet	2 \pm 2	4 \pm 2	9 \pm 5	6 \pm 3	16 \pm 6	1 \pm 1	1 \pm 1	1 \pm 1
cells	11 \pm 5	44 \pm 22	29 \pm 11	25 \pm 7	73 \pm 30	58 \pm 26	89 \pm 33	154 \pm 62
% >LOD	47%	95%	25%	45%	76%	99%	100%	100%

5.4.4 Quantification of cell dyes

Different approaches for the matrix matched quantification of metals in cells by LA-ICP-MS have been proposed.^{10, 29, 41} Here, an approach according to Wang *et al.* was applied, which is based on a calibration series of dried droplets containing the elements of interest mixed with Rhodamine B to simulate a matrix similar to the matrix of cells.⁴¹ Calibration arrays can be spotted onto glass slides using the same spotter with no need for further equipment. Thirty calibration series with four different concentrations of mDOTA-Ho and Ir-DNA-intercalator (10 spots per calibration series) were spotted. Because the droplet volume can be influenced by e.g. surface tension and the long-term buildup of deposits during spotting, it was checked for time dependent changes by optically measuring the droplet volume before and after spotting of each concentration. The droplet volume was sufficiently stable (327 pL \pm 1.6% for the spotting

of thirty calibration series within 25 min). For ablation of standards, the same fluence as for cells (0.36 J cm^{-2}) was used, whereby three shots were sufficient to completely ablate the standard on the glass slide. Dried spots had a diameter of approximately $150 \text{ }\mu\text{m}$ with a non-uniform appearance. The shape of dried droplets is affected by wetting and drying effects and depends on substrate surface condition and other environmental factors. To ensure complete ablation of the whole spot including the non-uniform rim, a larger area was ablated by line scans. Since neither ^{193}Ir , nor ^{165}Ho were detected in the coating, this does not affect the quantitative results and the ‘total consumption concept’ could be applied. As this is not true for all elements of potential interest, in future smaller droplets should be used to array calibration standards. Signals of each spot were integrated and averaged for each concentration. The precision of measured intensities was found to be concentration dependent. A spot-to-spot RSD of 8.5% was found for the lowest concentration of Ir-DNA-intercalator ($1.23 \pm 0.02 \text{ fg } ^{193}\text{Ir}$ per calibration spot), decreasing to 1.7% for the highest concentration ($1.23 \pm 0.02 \text{ ng } ^{193}\text{Ir}$ per calibration spot). Comparably low spot-to-spot RSDs were obtained for mDOTA-Ho, illustrating good precision of LA-ICP-TOF-MS. A linear calibration was fitted in Originlab[®] for ^{193}Ir with a sensitivity of $59 \text{ counts fg}^{-1}$ and for ^{165}Ho with a sensitivity of $110 \text{ counts fg}^{-1}$, respectively, while R^2 was >0.9999 for both elements. Limits of quantification (LOQs) were calculated to be 102 ag for Ho and 236 ag for Ir ($10 \times \text{SD}$ of the background from ablating dried cell suspension supernatant, see Table 13). The obtained LOQs are approximately two orders of magnitude lower compared to the previous study, see section 5.1. This is a consequence of an advantageous sample preparation, as a more precise non-contact spotter was used for arraying of calibration standards. Additionally, in the previous study, cells were fixed and dyed on the same slide as used for analysis, leading to higher background levels and RSDs.

This calibration was used to calculate the content of both elements per cell and Figure 33 shows the Ir and Ho mass distributions in THP-1 cells. The Ir mass in cells is well above the LOQ (dashed vertical line), while Ho mass in some cells is close to the LOQ. The histogram of Ho content per cell appears to follow a simple normal distribution, while the Ir distribution has two maxima. This finding is interpreted as a proportionality of the Ir-DNA-intercalator content to the amount of DNA, which varies according to the cell-cycle phase, see section 5.4.6.

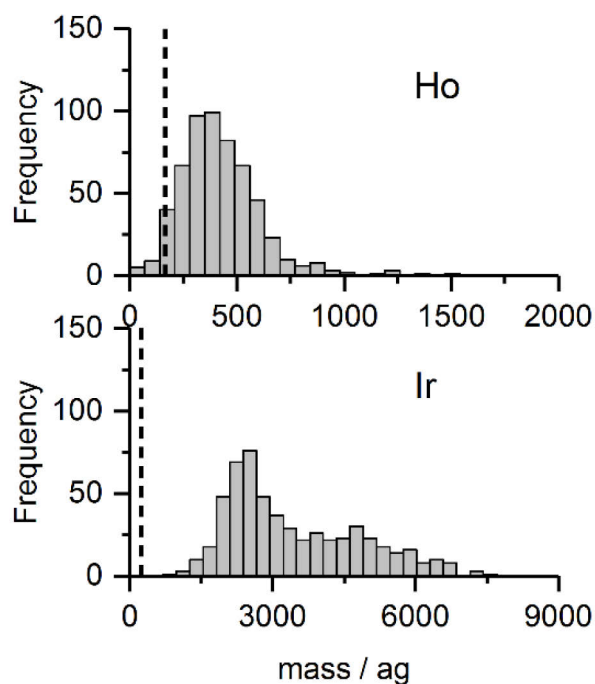


Figure 33 Histograms of Ho (top) and Ir (bottom) mass per single THP-1 cell. Dashed lines represent LOQs of 102 ag for Ho and 236 ag for Ir, respectively.

In the previous study (section 5.1), LA single spot analysis was compared with LA imaging for measuring the elemental content of single cells and no significant differences regarding the variance and the mean of intensity distributions were found, although distribution means differed by $\sim 10\%$. This was the consequence of a low sample size which lead to a large standard error of the mean (SEM) of 17% ($\alpha=0.05$). It was shown that at least 435 cells need to be analyzed to obtain a mean with a relative SEM $\leq 5\%$. In the current study, a Ho content of 420 ± 188 ag per cell was determined with a relative SEM of 3.7% ($\alpha=0.05$, $n=562$). Accordingly, LA-ICP-MS single-cell studies can be conducted on a robust statistical basis using the herein presented approach and equipment.

Moreover, both isotopes of Ir were quantified and it was found that the isotopic composition in single cells of 1.68 ± 0.28 ($^{193}\text{Ir}/^{191}\text{Ir}$) reflects the natural isotope ratio, which demonstrates the absence of interferences. The relatively high uncertainty of the isotope ratio on a single-cell level of 17% is a consequence of low concentrations and low signal intensities.

5.4.5 Detection of endogenous isotopes in single cells

The spot-to-spot SD of signals of dried blank droplets was used to calculate the limit of detection (LOD) for all other isotopes using the IUPAC approximation for signals having low

count numbers (see appendix section 7.3.1).⁸⁸ The signal RSD is mostly defined by droplet-to-droplet volume RSD of the spotter, which was fairly low (<0.5%), and the measurement uncertainty of LA-ICP-TOF-MS. The signal RSDs of most isotopes in blank droplets were very low and were mostly dominated by the measurement uncertainty of LA-ICP-TOF-MS (counting statistics), see Table 13. For ²³Na and ²⁴Mg few outliers were observed and discarded, see appendix section 7.3.1 for details. Distribution patterns of blank corrected signal intensities from single-cell measurements are shown in Figure 34, in which LODs are depicted as dashed vertical lines. Signals of ²³Na, ²⁴Mg, ³¹P, ⁶⁶Zn and ¹³⁸Ba were detectable in most cells, while ²⁷Al, ³²S, ⁴⁴Ca, ⁵⁵Mn, ⁵⁶Fe, ⁶⁵Cu, ⁷⁵As and ⁸⁸Sr were detectable in less than 50% of cells.

Several of these isotopes were not expected to be contained in detectable quantity in cells. Mass interferences are a possible reason for wrongly detected isotopes. However, for measuring ³²S, ⁴⁴Ca, and ⁵⁶Fe, the mass resolution was sufficient to at least partially resolve the major interferences and for ⁷⁵As the presence of its major interference ⁷⁵ArCl could be excluded as well, see appendix section 7.3.1. Unexpectedly detected isotopes are thus believed to have their origin in trace impurities of substances used for cell culturing or tagging. Paraformaldehyde fixing of cells is known to allow small molecules to pass through the cell membrane. Hence only minor influences are expected for elements predominantly bound to bigger molecules, whereas elements which are solubilized or bound to small molecules might have been lost or unintentionally added during staining.

The detection limits of several potentially interesting isotopes like ²⁷Al, ³²S, ⁴⁴Ca, ⁵⁵Mn, ⁵⁶Fe, and ⁶⁵Cu might be further improved by usage of a reaction/collision cell, as has been recently demonstrated.^{80, 89} Optimizing reaction/collision cell conditions for the detection of these isotopes by ICP-TOF-MS would be the next step.

Signal intensities of isotopes in single cells appear to show different distributions, see Figure 34. While ²⁴Mg, ³¹P, ⁶³Cu, ⁶⁶Zn, and ¹³⁸Ba appeared to show a log-normal distribution, ²³Na signal followed a normal distribution. Log-normal distributions of cell size and elemental contents are typically observed for biological cells.⁹⁰ Thus, the normal distribution of ²³Na intensity was unexpected but might be explained by the main function of Na in animals, as Na⁺ ions are used for maintenance of electrolyte and fluid balance. These Na⁺ ions are not tightly bound to cells and, thus, the observed Na distribution is believed to be a consequence of diffusion during sample preparation. For isotopes with a detectability of >95% in single cells, distributions were fitted, see Figure 34.

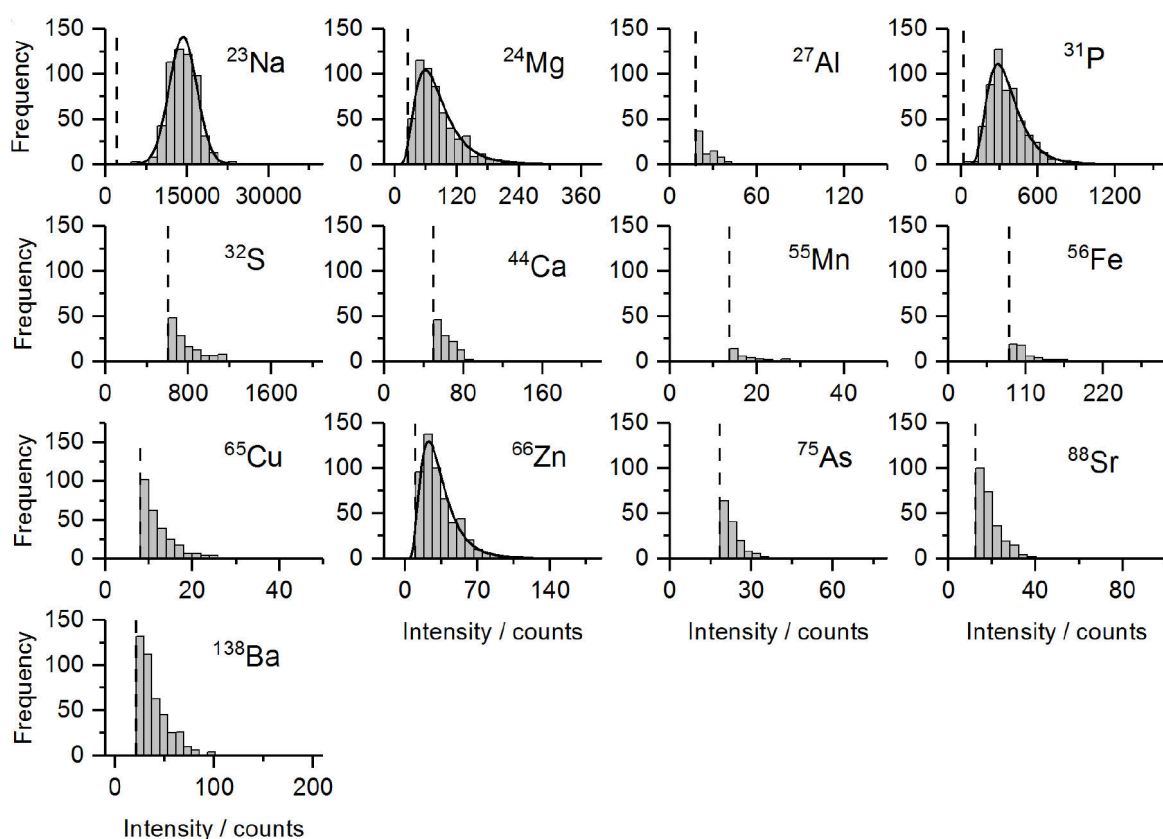


Figure 34 Blank corrected intensity distributions of isotopes in THP-1 cells (n=562) obtained via LA-ICP-TOF-MS. LODs were calculated ($3 \times \text{SD}$ of blank spot intensities) and inserted as dashed lines. For isotopes, which were detected in $>95\%$ cells, log-normal (^{24}Mg , ^{31}P , ^{66}Zn) or normal distributions (^{23}Na) were fitted in Originlab®.

Recently, Wang *et al.* studied the distribution of several elements (P, S, Mn, Fe, Cu, and Zn) in single cells by pneumatic nebulization ICP-MS.⁸⁰ They found multimodal distributions for P and several other elements for three mammalian cell lines (HeLa, A549, 16HBE) and they inferred that these modes represent sub-populations of cancerous cell lines. For the THP-1 cell line studied here, unimodal distributions for all studied elements were observed (except for the Ir-DNA-intercalator). This difference in observations is interesting and should be subject to further investigations.

5.4.6 Correlation of isotope intensities

The simultaneous measurement of all isotopes by ICP-TOF-MS enables the correlation of isotopic contents on a single-cell basis in a multidimensional way. To get an idea to which degree isotope signal intensities correlate with each other, the Pearson correlation coefficients for all isotopes with detectability $>95\%$ in single cells were calculated, see Table 14. While ^{31}P and ^{66}Zn intensities showed the highest correlation (0.83), ^{31}P and ^{24}Mg showed the lowest

correlation (0.47), see Figure 35. Moreover, ^{66}Zn and ^{31}P signals correlated well with ^{165}Ho and ^{193}Ir contents (coefficients 0.76 to 0.80). Because of their good correlation, P and Zn should be further investigated for their suitability as a label free marker for the cell volume in LA studies, see also discussion by Mueller *et al.*⁶⁶

Table 14 Pearson correlation coefficients of elements with detectability in >99% of cells.

	^{24}Mg	^{31}P	^{66}Zn	^{165}Ho	^{193}Ir
^{23}Na	72%	66%	65%	69%	67%
^{24}Mg		47%	59%	57%	59%
^{31}P			83%	77%	80%
^{66}Zn				76%	79%
^{165}Ho					70%

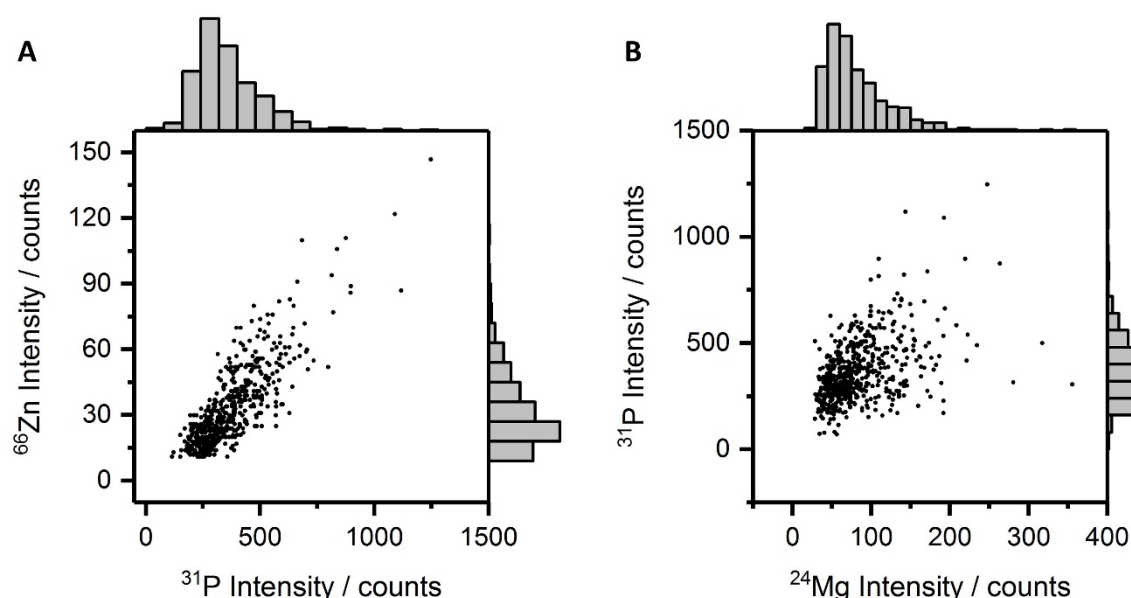


Figure 35 Scatter plots of single-cell elemental intensities with (A) highest correlation, i.e. ^{31}P and ^{66}Zn , and (B) lowest correlation, i.e. ^{31}P and ^{24}Mg .

The signal intensity of the artificially introduced Ir-DNA-intercalator correlates well with the signal of the naturally occurring essential nutrient ^{31}P (correlation coefficient 0.81), see scatter plot Figure 36, left. In mass cytometry, the Ir-DNA-intercalator is usually used to gate for single nucleated cells.⁹¹ Moreover, in a recent multiplex LA-ICP-MS study we could show that the Ir-DNA-intercalator intensity is roughly proportional to the cell-cycle phase which correlates with the specific DNA content of individual cells.⁶⁶ Even though the Ir-DNA-intercalator does not provide sufficient stoichiometry for routine automated assessment of the cell cycle phase,^{92, 93} the rough correlation of Ir-DNA-intercalator with cell-cycle phase was used to demonstrate the

possibilities such a dataset offers. Manually chosen gating borders are plotted as red-dashed lines in Figure 36. The percentages of cells in G1, S, and G2 phase agree well with published values for THP-1 cells.⁹⁴ Such a cell cycle analysis enables e.g. tracking of Zn / P accumulation throughout the cell-cycle, see Figure 36, right side. The increase of the Zn and P content from G1 to S to G2 phase was in line with our expectation, as cells grow throughout all three phases until they divide again, therefore P and Zn are accumulated as both are essential nutrients.

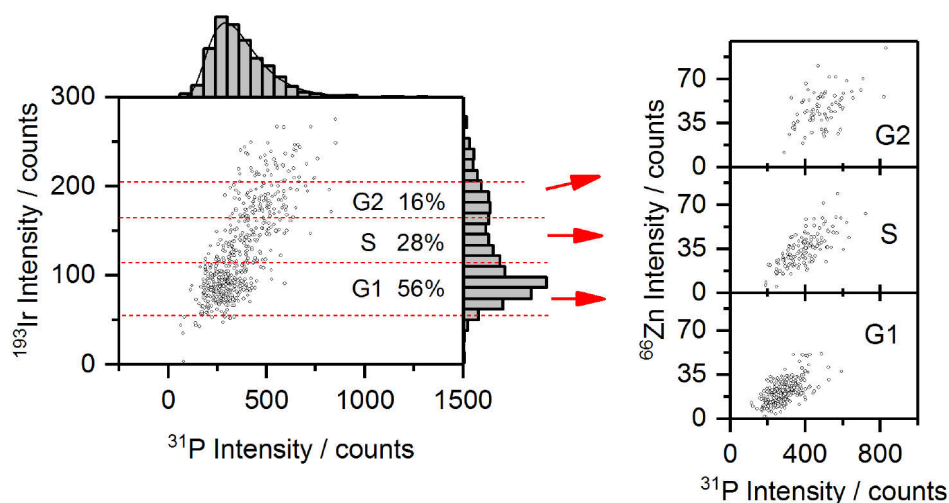


Figure 36 Scatter plot of ^{193}Ir -DNA-intercalator and ^{31}P intensities in single cells with marginal histograms. Red horizontal dashed lines indicate approximate gating of cell-cycle phases. This gating strategy was used to track the accumulation of Zn and P throughout the different cell-cycle phases (right side).

Recently, in toxicology exposure studies to different Cr(VI) concentrations it was shown that the Mg content can be used as a label free biomarker for cell stress and size.⁹⁵ So far, three individual measurements had to be performed for such a study: one for each isotope and one for the cell size. For a recent arsenic oxide toxicity study by time-resolved ICP-MS, several cellular biomarkers and arsenic uptake had to be measured separately, preventing the correlation of arsenic uptake and biomarker information on a single-cell level.⁹⁶ The approach presented here provides all this information in a single run and allows correlating the fingerprints of endogenous and exogenous elements and other physicochemical parameters that might lead to a better understanding of the role of the metallome in the cell life cycle.

5.4.7 Conclusion

A novel single-cell arraying approach was tested as preparation method for quantitative high throughput analysis by LA-ICP-TOF-MS. The presented approach is highly suitable for

quantitative determination of cellular isotopic contents, as the calibration can be performed conveniently by using arrayed dried droplets of corresponding isotope standards. The capability of LA-ICP-TOF-MS to detect endogenic and exogenic isotopes as fingerprints of individual cells with detection limits as low as hundred attogram was described. It was shown how multiplexing capabilities of LA-ICP-TOF-MS can be used to characterize cells using elemental cell dyes, and how gating for parameters can be correlated with changes in naturally occurring elemental contents of cells. In the future, cell characterization can be expanded by immunocytochemistry for the study of diseases connected with naturally occurring elements. I believe that the presented approach opens new ways for high throughput LA-ICP-TOF-MS analysis of single cells. This approach might become an alternative to pneumatic nebulization single-cell ICP-MS, offering better quantification approaches and an uncompromised transport efficiency of single cells of all sizes to the ICP.

5.5 Comparison of LA-ICP-TOF-MS and sc-ICP-SF-MS

Cells grown and dyed in a single batch were analyzed via sc-ICP-SF-MS and via piezo acoustic single-cell arraying with subsequent high throughput LA-ICP-TOF-MS. In this chapter the two methodologies are compared regarding their figures of merit. Expected, but still noticeable was a significantly higher intensity per single cell for an analysis using a ICP-SF-MS (Element XR) instrument in comparison to the used ICP-TOF-MS (icpTOF). The difference in sensitivity can be compared e.g. by using the main peak of Ir-DNA-intercalator intensity, from which a ~35 times higher sensitivity for sc-ICP-SF-MS was calculated for ^{193}Ir . This agrees reasonably well with the expected sensitivity gain for an ICP-SF-MS which was calculated using published average sensitivities for both devices (17 \times , see Table 1). The fact that sc-ICP-SF-MS showed an about twice as high sensitivity (35 \times), is believed to be a consequence of daily instrument performance variations. More importantly, median background levels were decreased ~500 times for LA-ICP-TOF-MS. The ~14 times over-proportional signal intensity decrease of background levels for LA-ICP-TOF-MS can be explained by a simple mass balance: in sc-ICP-SF-MS a specific volume of cell suspension is introduced into the ICP within a single integration time:

$$V = flow_{neb} * TE * t_{int} = 4667 \text{ pL}$$

with

- V = Cell suspension volume introduced into the ICP within a single integration time
- $flow_{neb}$ = Flow rate of the nebulizer (~40 $\mu\text{L min}^{-1}$)
- TE = Transport efficiency (estimated to ~70% using CyTOF calibration beads)
- t_{int} = Detector integration time (10 ms)

In the sample preparation process for LA-ICP-TOF-MS, i.e. during single-cell arraying, a precise amount of only ~330 pL is spotted and subsequently ablated and introduced into the ICP. Accordingly, in sc-ICP-SF-MS ~14 times more cell suspension was transported into the ICP, compared to the arrayed droplet volume subsequently analyzed using LA-ICP-TOF-MS. Consequently, the signal to noise ratio (s/n) was significantly enhanced for LA-ICP-TOF-MS (s/n = 113) in comparison to sc-ICP-SF-MS (s/n = 41), leading ultimately to lower detection limits for LA-ICP-TOF-MS (2.8 times lower). Arraying with subsequent LA-ICP-MS can potentially provide an even higher gain in detection limits, as the spotting has very high

precision in the order of 0.5% (volume RSD of droplets), which leads to RSDs of $\sim 1.8\%$ for LA-ICP-MS analysis at sufficiently high signal intensities (see e.g.

Table 17). sc-ICP-MS using a HECIS has inherently a relatively high signal RSD compared to conventional liquid ICP-MS because HECIS is designed to allow bigger droplets to reach the ICP, decreasing the signal stability of the sample introduction system. In this study, the lowest RSD obtained using such a HECIS to introduce a standard solution was $\sim 9\%$ (see Figure 27), which means that the approach of arraying and subsequent LA-ICP-MS analysis can provide about 5 times lower background noise. This advantage will prove especially useful for analysis of elements with inherently high background, e.g. sulfur. However, it should be mentioned that in sc-ICP-MS detection limits can be lowered by reducing the detector integration time. The observed noise is related to the chosen integration time according to statistics introduced in section 2.1.1. The lowest integration time possible in sc-ICP-MS is the actual signal duration of a cell event. A cell event has a duration in the order of $500\ \mu\text{s}$, which is $20\times$ shorter than the herein used sc-ICP-MS integration time. A twentyfold reduction of the integration time would lower the background noise to $\sim 22.4\%$. Accordingly, if a time resolution which can resolve ion clouds of different single cells is supported by the used ICP-MS device, detection limits are expected to be in the same order.

Comparing the Ir-DNA-intercalator intensity distribution obtained via sc-ICP-MS (Figure 30 left, top) to data obtained via arraying and subsequent LA-ICP-MS analysis (Figure 33), one major difference can be observed. While the LA-ICP-MS histogram shows a second minor peak, the sc-ICP-MS histogram shows only one peak with a flat tail. The second peak corresponds to cells with double DNA content right before division into two cells. The lack of a second peak in the sc-ICP-MS histogram is believed to be a consequence of the cell-size dependent transport efficiency in sc-ICP-MS. Cells having twice the DNA content correspond to the fraction of bigger cells, which have a lower transport efficiency.

The two methods of analyzing single cells using ICP-MS differ considerably in throughput. In sc-ICP-MS, the maximal throughput is usually limited by the ability to distinguish two subsequent cell events from each other and thus by the used detector integration time. While longer integration times like $10\ \text{ms}$ allow for detecting a few cells per second, very fast data acquisition which is able to timely resolve a cell's ion cloud emerging from the ICP (200 to $500\ \mu\text{s}$ in duration) allows for detecting up to $1000\ \text{cells s}^{-1}$.^{44, 45} The throughput of the two-step process of single cell arraying and subsequent LA-ICP-MS analysis is mainly limited by the

axis movement of the used arraying and LA system. Herein, for arraying a throughput of ~500 cells per hour and for LA a throughput of ~1 cell per second was achieved. However, with the recently introduced generation of the commercialized single cell arraying platform cellenONE[®] (cellenion SASU) a throughput up to 2000 cells per hour can be achieved.^{xv} This results in an overall throughput in the order of 1000 cells per hour for the two-step process. Accordingly, with sc-ICP-MS a throughput up to three orders of magnitude higher can be achieved compared to the two-step process of arraying and subsequent LA-ICP-MS analysis.

^{xv} Private communication with G. Tourniaire (cellenion SASU)

6. Summary and Outlook

In this work, the throughput for LA-ICP-MS based cytometry was successfully enhanced. The two LA modes used to analyze single cells, imaging and single spot analysis (SSA), were successfully characterized regarding figures of merit and compared with each other. Most importantly, SSA has at least a 10× higher throughput, as well as lower detection limits. It became clear, that for a quantitative comparison of both LA modes a high number of cells (>400) must be analyzed to enable a statistically significant comparison. Manual targeting of single cells was identified as too laborious, usually preventing such studies from being carried out. Accordingly, it was the goal to find a way to automate single-cell targeting by introducing an additional sample preparation step to array single cells for subsequent automated LA analysis.

Two approaches for single-cell arraying were evaluated. First, an approach to hydrodynamically trap cells in an array of microchambers using clamped PDMS-based multilayer chips was tested. A novel drying procedure was elaborated to prevent single cells from surface tension induced displacements during the removal of the PDMS-based chip to allow for accessibility via LA. Unfortunately, the structural instability of PDMS-based chips did not allow single-cell arraying in a clamping device. However, the approach is still considered as promising and a chip design optimized for operation in a clamping device with a defined clamping pressure might solve this problem.

Secondly, a novel single-cell arraying technology relying on a piezo acoustic microdroplet arrayer in conjunction with image recognition of cells was tested. Using optimized parameters, an unprecedented single-cell occupancy of >99%, decent arraying throughput (up to ~550 cells h⁻¹) in combination with a very high cell recovery of 66% were achieved. Moreover, the commercial system was easy to operate and allowed preparation of arrays of calibration standards simulating the matrix of cells. The transport efficiency of the approach is not cell-size dependent, which is advantageous compared to other single-cell arraying methods and single-cell ICP-MS using conventional pneumatic nebulization, even if high efficiency cell introduction system (HECIS) with a heated total consumption spray chamber is used. Software developments enabling better single-cell recognition and tracking within the PDC, as well as hardware-based developments like a faster axis systems or fluorescence detection of cell (-

markers) have the potential to improve the arrayer's usability, its figures of merit and versatility even further.

Finally, a cell array prepared using the piezo acoustic microdroplet arrayer was analyzed using quantitative high throughput LA-ICP-TOF-MS. The capability of LA-ICP-TOF-MS to detect endogenic and exogenic isotopes as fingerprints of individual cells with detection limits as low as hundred attogram was described. It was shown how multiplexing capabilities of LA-ICP-TOF-MS can be used to characterize cells using elemental cell dyes, and how gating for parameters can be correlated with changes in naturally occurring elemental contents of cells.

I believe that the presented approach opens new ways for high throughput LA-ICP-TOF-MS analysis of single cells. This approach might become an alternative to pneumatic nebulization single-cell ICP-MS, offering better quantification approaches and an uncompromised transport efficiency of single cells of all sizes to the ICP. In the future, cell characterization using LA-ICP-TOF-MS can be expanded by immunocytochemistry to enable an in-depth characterization of single cells playing a role in diseases connected to naturally occurring elements.

Moreover, the herein produced cell arrays are considered a very promising tool to enable high throughput single cell analysis using different mass spectrometric techniques (e.g. SIMS or MALDI) in future. Furthermore, the produced cell arrays hold great potential to ease high throughput multimodal analysis of cells using optical methods such as surface enhanced raman spectroscopy (SERS).

7. Appendix

7.1 Comparison of different LA modes: single-element measurements

Quantitative comparison of metal content distributions.

In this supplementary section, the experiments presented in sections 5.1.1 and 5.1.2 were repeated with the modification that only the single isotope ^{193}Ir was measured, see single-element data acquisition parameters, Table 4. Such an experiment can be compared best with data from the single isotope measurement of a metal in a cell in suspension in the so called sc-ICP-MS mode.

Single-element imaging

Single-element imaging of ^{193}Ir was performed using the same LA parameters like in multi-elemental imaging, see Table 2, for optimized single-element ICP-MS data acquisition parameters see Table 3. Acquired raw data was transformed into images using the same procedure as for multi-elemental imaging. Overlays of ^{193}Ir distribution images and the corresponding bright field image were prepared in CorelDraw, see Figure 37.

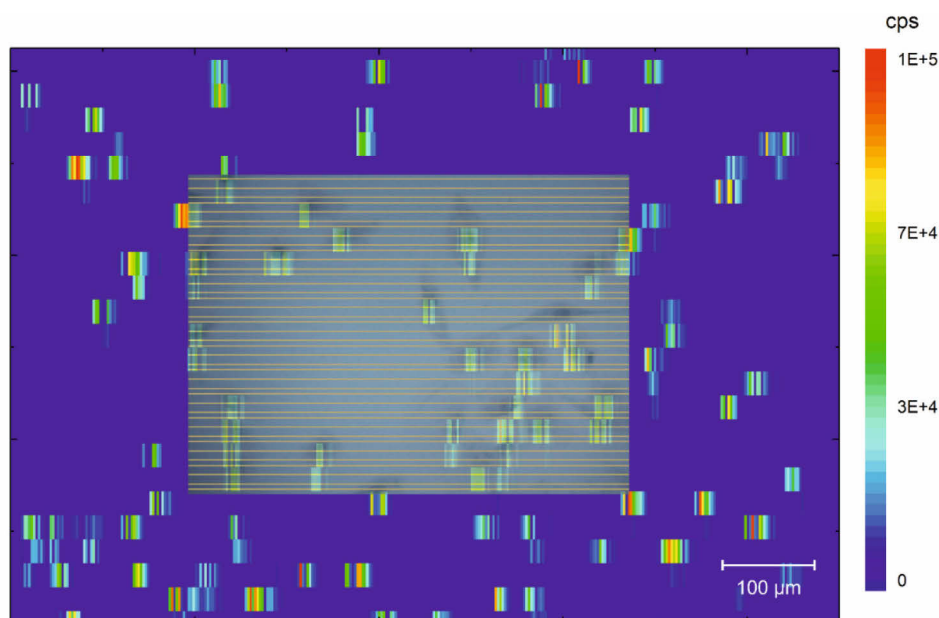


Figure 37 Overlay of singleplex LA-ICP-MS image of ^{193}Ir and the brightfield image of fibroblast cells before LA. Yellow lines in the brightfield image indicate individual line scans with a laser spot diameter of $30\text{ }\mu\text{m}$ in a line to line distance of $25\text{ }\mu\text{m}$.

If compared to the overlay from multi-element ^{193}Ir imaging in Figure 8 (a), the two images look very similar. Darker regions in the middle of cells, corresponding to the nuclei, gave higher signals as well. Between single-element and multi-element imaging of Ir-DNA-intercalator, no qualitative difference is visible. Signals of 59 cells were integrated on a single-cell basis analogous to multi-element imaging, see procedure described in section 4.1.4. Cells were found to comprise of 52 ± 14 pixels, while the smallest cell had 20 and the biggest cell 96 pixels. Compared to multi-element imaging (27 ± 12 pixels) the cells have approximately twice the number of pixels. This is a consequence of different acquisition times per pixel: in single-element mode the acquisition time is only 103 ms per pixel, whereas the acquisition time in multi-element mode is approximately twice as big with 220 ms. Each integrated intensity value was corrected by a blank intensity calculated according to the number of pixels. The average blank signal of a pixel was calculated by averaging over an area without cells (243 pixels) and was found to have acceptable low values of 63 ± 46 counts. Compared to multi-element imaging (18 ± 25 counts), the background per pixel is about three times higher. Most likely, this is a consequence of a slightly unequal distribution of the background on the glass slide. However, the background was considered sufficiently stable within the imaged area. Moreover, the background is in the order of only one percent of the Ir intensity per cell, and accordingly the influence on the quantitative results is limited. Cells were found to have a background corrected integrated intensity of $5.4 \times 10^3 \pm 2.9 \times 10^3$ counts / cell, agreeing well with the numbers obtained from the multi-element measurements ($5.3 \times 10^3 \pm 2.8 \times 10^3$ counts / cell). Figure 38 shows the resulting histograms of integrated Ir intensity.

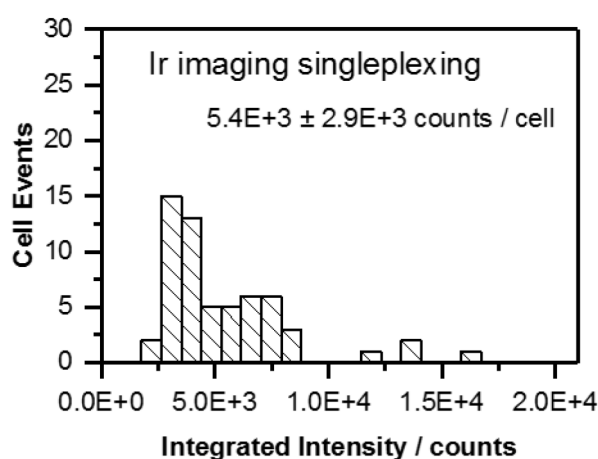


Figure 38 Histogram of ^{193}Ir intensity per cell for single-element imaging.

Single-element single spot analysis

Single-element SSA of single cells was performed using the same optimized LA-parameters as for multi-element SSA, see section 4.1.4, and ICP-MS data acquisition parameters optimized for single-element analysis, see Table 5. The Ir intensity of 51 cells was measured, as well as the blank Ir intensity of 11 cell-free spots. Acquired signals were integrated for each cell and each blank, see section 4.1.4. The integrated blank intensities were averaged to 1017 ± 46 counts for Ir, which was in the same order as the background of the multi-element single spot analysis ($\sim 25\%$ higher). From each integrated intensity of a single cell, the mean blank intensity was subtracted, which gave an integrated mean intensity of $6.8 \times 10^3 \pm 3.8 \times 10^3$ counts. This results in average signal to noise ratio of 148:1. The resulting histogram of Ir intensity per single cell is shown in Figure 39. The distribution appears to be two almost separated Gaussians, having their maxima at $\sim 4 \times 10^3$ counts and $\sim 8 \times 10^3$ counts.

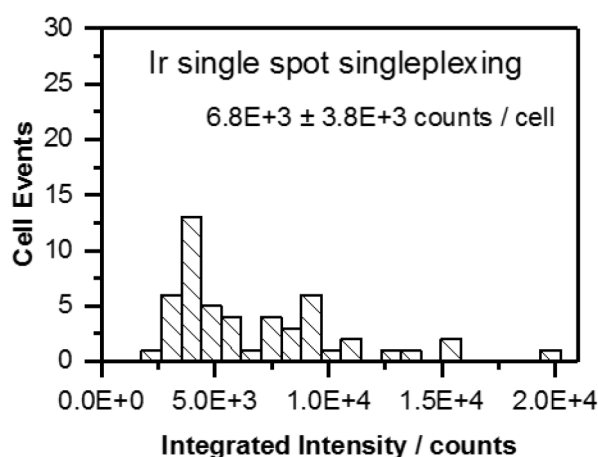


Figure 39 Histogram of Ir intensity per cell for single-element single spot analysis.

Calibration via nitrocellulose membrane

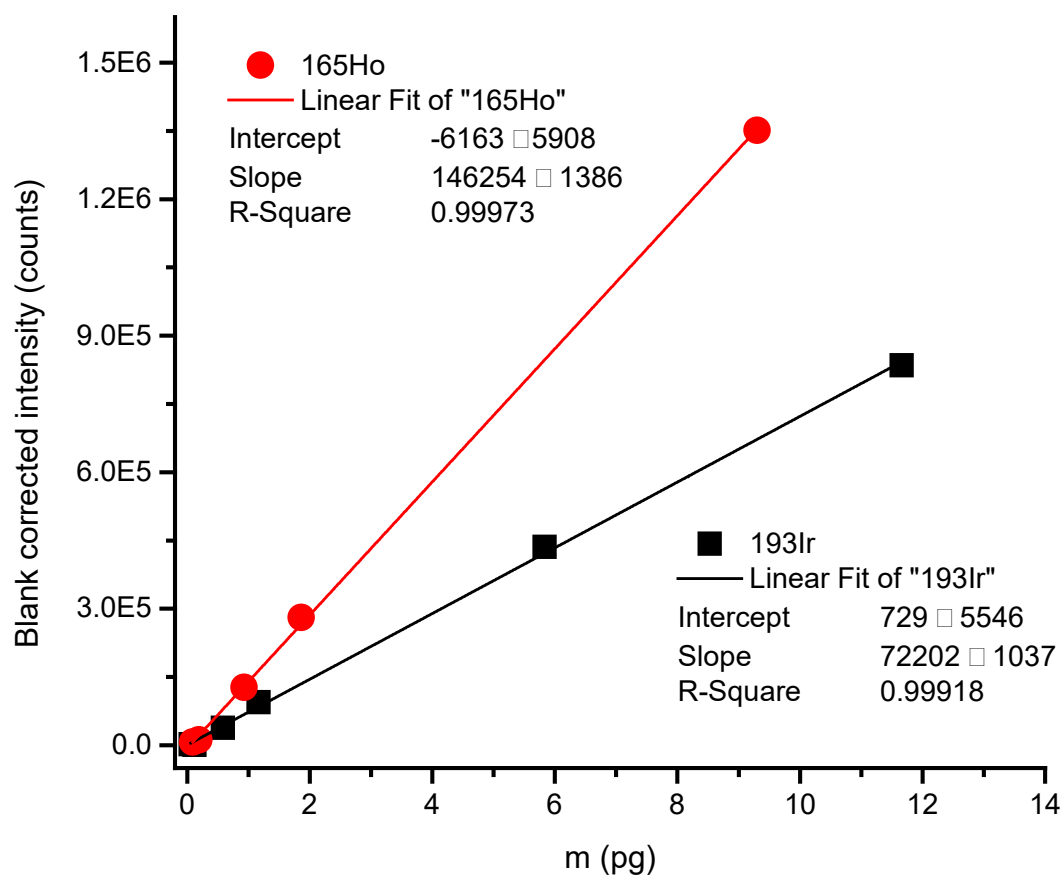


Figure 40 Calculated trend line for ^{165}Ho from 0.09 pg to 9.8 pg (the highest concentration of 18.6 pg was an outlier) and for ^{193}Ir from 0.09 pg to 18.6 pg Ir

7.2 Establishing of sc-ICP-MS using the HECIS

7.2.1 sc-ICP-MS using HECIS standard operation procedure

- Roll the wagon with sample introduction system and heating system next to Element (2 / XR)
- Connect spray chamber via ball fitting to torch and allow it to rest on the support, such that it is straight
- Take nebulizer out of bag in first drawer and insert into spray chamber
- Plug heating system to socket
 - o attention: make sure that the socket does not share one fuse with other electrical equipment, since in case of overheating all devices connected to the fuse are shut down!

It is necessary to evaporate any nebulized liquids to prevent condensation or deposition of liquids within the spray chamber: accumulating liquids finally would flow into the torch and blow out the plasma. Thus, the *Add Gas 1* flow is heated to 165-175°C within the spray chamber using the manual heating system. The start-up routine of Element 2 /XR unfortunately can't be fully automated for two reasons: (i) it is not possible to put a final *Add Gas 1* flow; (ii) and the temperature only can be controlled manually.

Start-up routine:

- a. Switch on heating system → adjust the voltage by turning to ~70 V, see display (attention: the scale starts at 50 V!)
- b. Adjust Plasma settings in Element software, see marked parameters in Table 15
- c. Switch on Plasma
- d. After the plasma is on (~15min), open the tune window, make sure *Add Gas 1* and *Sample Gas* flow is set to 0.0 L min⁻¹, press the play button
 - i. Carefully ramp up the *Add Gas 1* to 0.65 L min⁻¹;
 - ii. Carefully ramp up the *Sample Gas* to 0.2 L min⁻¹
 - ➔ Always have an eye on the plasma; it will be flickering, if it the gas flows were ramped too fast.
- e. The system is now ready for tuning. The temperature (displayed on the temperature safety switch) may change during tuning as gas flows and liquid flows into the ICP change. For measurements the temperature must be kept stable.

Table 15 Settings for Element 2/XR start-up routine. Parameters which need to be adjusted are marked in bold.

Plasma Start Parameters		
Cool Gas Flow	16	L/min
Auxiliary Gas Flow	0.9	L/min
Flush Sample Gas Flow	0.2	L/min
Flush Add Gas1 Flow	0.65	L/min
Flush Add Gas2 Flow	0	L/min
Flush Time	180	s
Z-Position during Ignition	3	mm
Delay before Ignition	15	s
Ignition Power	1000	W
Operation Power	1200	W
Final Sample Gas Flow	0	L/min
Sample Gas Ramp Time	60	s

Switching-off routine:

Before shutting down the system, turn off the sample gas first (slowly), and the Add Gas1 afterwards. Otherwise liquid could condensate within the spray chamber, which could blow out the plasma.

7.2.2 sc-ICP-MS data acquisition

In sp-ICP-MS relatively short integration times are chosen, whereby the actual choice is a tradeoff: the integration time is proportional to the background (noise) and indirect proportional to the possible throughput, favoring shorter integration times of 3 ms and less, but short integration times increase the chance of incompletely detected particles, favoring longer integration times. Despite the herein used integration time of 10 ms is already relatively long, the magnet settling time of 1 ms still accounts for about 10% of the whole measurement time, i.e. the maximum observable transport efficiency would be limited to 90% by the instrument. Since biological samples are quite costly and tedious to produce, it was decided to avoid the magnet settling time by measuring only within flat top of mass peaks in E-Scan mode, compare Shigeta *et al.*⁸² The parameters were adapted to sp-ICP-MS measurements, see Table 5. The ‘settling time’ between measuring two sampling times of a mass peak is expected to be negligible, since no magnet settling time must be waited. Unfortunately, the software is not able to export the ‘raw data’ of the different samples of the mass peak directly as a time-resolved chromatogram. The chromatogram data contains the beforehand averaged 1000 samples of the

60% mass window, equaling 600 samples. The measured time between two data points, i.e. between two measurement segments, is 6.0033 ± 0.0005 s. To make use of every acquired sample time, the raw data must be exported manually as consecutively acquired mass spectrograms. Surprisingly, such a mass spectrogram consists of only 598 instead of 600 samples, meaning 5.980 s true sampling time per segment. Compared with a measured segment duration of 6.0033 s from the chromatogram, this results in 99.6% of the segment time being used for measuring and 0.4% of the time being instrument overhead. To allow for sp-ICP-MS evaluation, the acquired raw data (a serial measurement of mass spectrograms) must be transformed into a time-resolved measurement. As this data transformation is too laborious to be done manually, this process was automated using a Labtalk[®] script in combination with automated visualization of data as histograms in Originlab[®].

7.3 High throughput Laser Ablation ICP-TOF-MS and isotopic fingerprinting

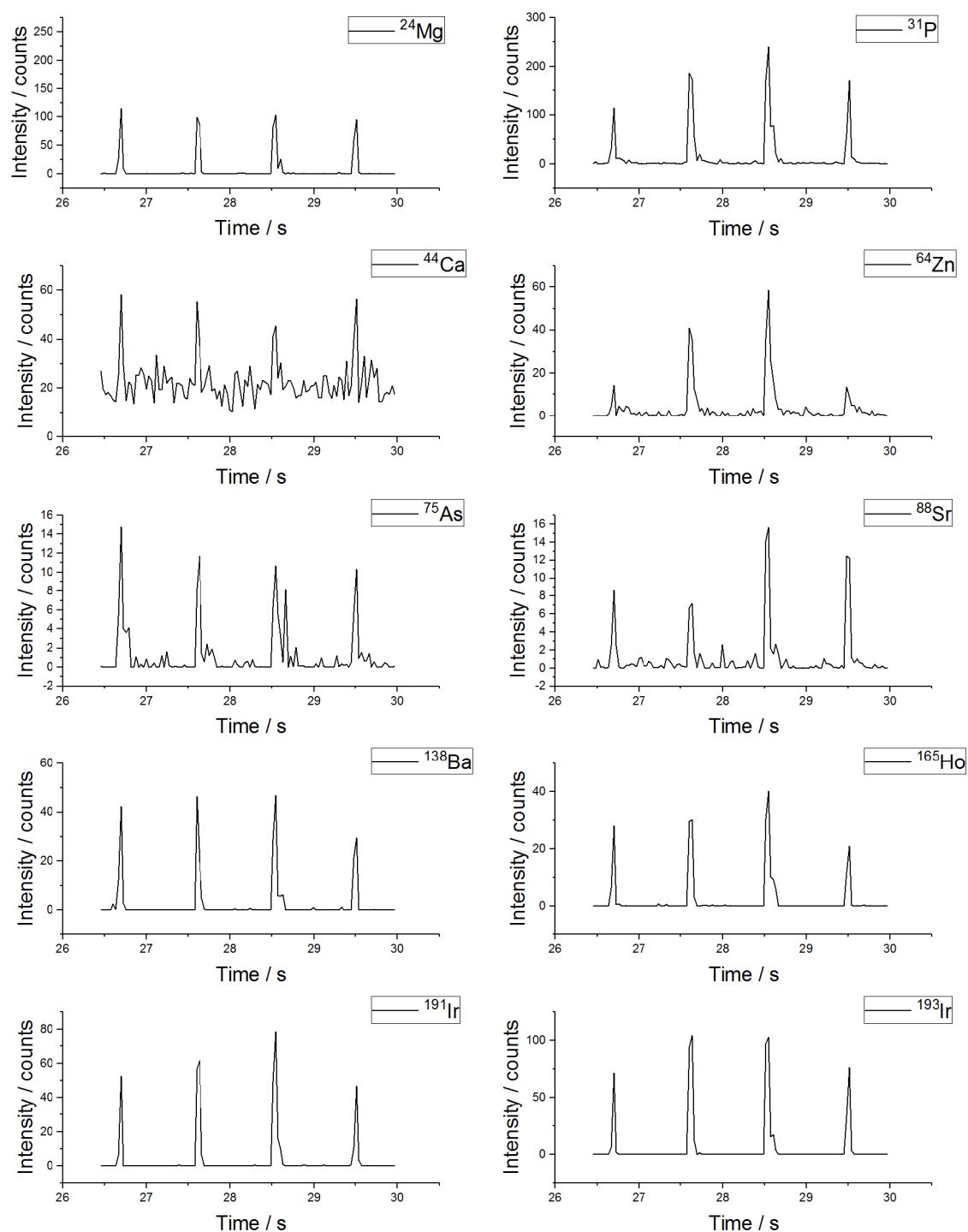


Figure 41 Transient signals of selected naturally occurring isotopes and metal-dyes measured by LA-TOF-ICP-MS from four individual single cells as shown in Figure 41 in detail.

7.3.1 Background correction

Remark: Spots of dried cell suspension supernatant are not recognizable visually. Thus, for ablation of dried cell suspension supernatant it had to be relied on sufficient positioning accuracy of the array and the LA-system. However, accurate positioning could be confirmed, due to accurate positioning of several cells, which were spotted together with the cell suspension supernatant and were observed at expected positions within the array. Figure 42 shows the time resolved blank measurement of several selected elements.

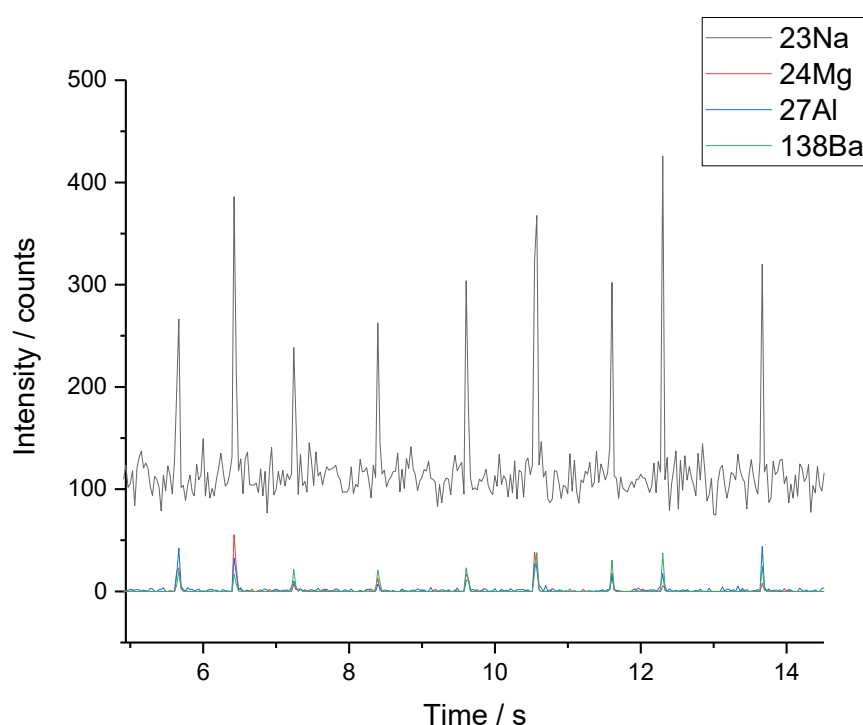


Figure 42 Ablation of dried droplets from cell suspension supernatant spotted onto a superforst+ glass slide with the same settings used for the ablation of the cell array. From this measurement the so-called “drop blank” in Table 13 was calculated.

Determination of limits of detection

The RSD of the drop blank was expected to approximate the droplet-to-droplet volume RSD of the spotter (<0.5%) plus the measurement uncertainty of LA-ICP-TOF-MS. Surprisingly, the drop blank for ^{23}Na had an RSD of 41% (4939 ± 2036 counts), which appeared as too high. Looking at a box plot of 61 blanks, few outliers could be identified using the Grubbs outliers

($\alpha = 0.05$; normality was confirmed by Lilliefors test, $\alpha = 0.05$), see Figure 43, left. These few outliers are thought to have their origin in particulate matter (e.g. dust) and were discarded for all elements. After correction, this led to an RSD of 15% for Na (4332 ± 657 counts), which was still high compared to our experiences made with ablation of spotted homogeneous solutions (see e.g. RSDs found for the ablation of calibration standards below). This is probably a consequence of randomly distributed particulate matter. Usually, outliers did not correlate with blank intensities of other elements, only blank #41 gave significantly elevated intensities for both, ^{23}Na and ^{24}Mg , see Figure 43 (right) and Figure 44, suggesting that one particle containing both elements was ablated at this spot.

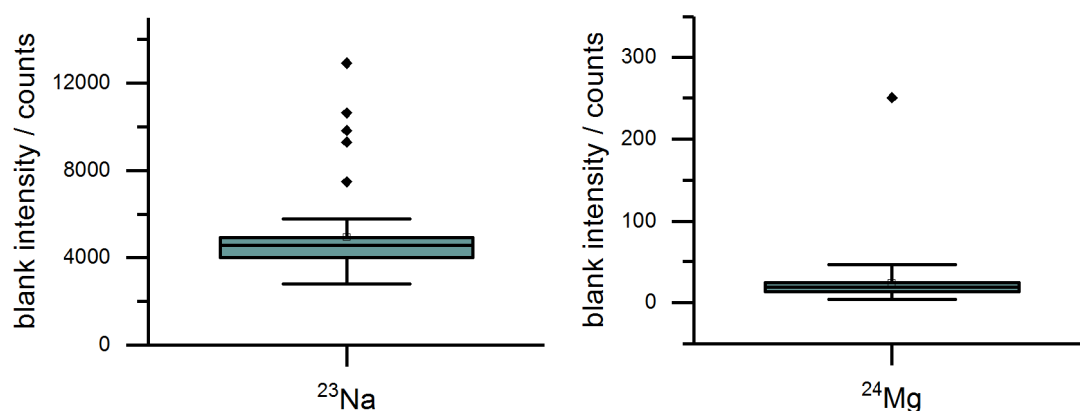


Figure 43 Box plot for background intensities of ^{23}Na and ^{24}Mg from measurements of spotted cell suspension supernatant. Data was not significantly drawn from a normally distributed population at the 0.05 level for both elements according to Lilliefors test for normality. Data points that lie outside of the whiskers are outliers (Grubbs outliers test at 0.05 level).

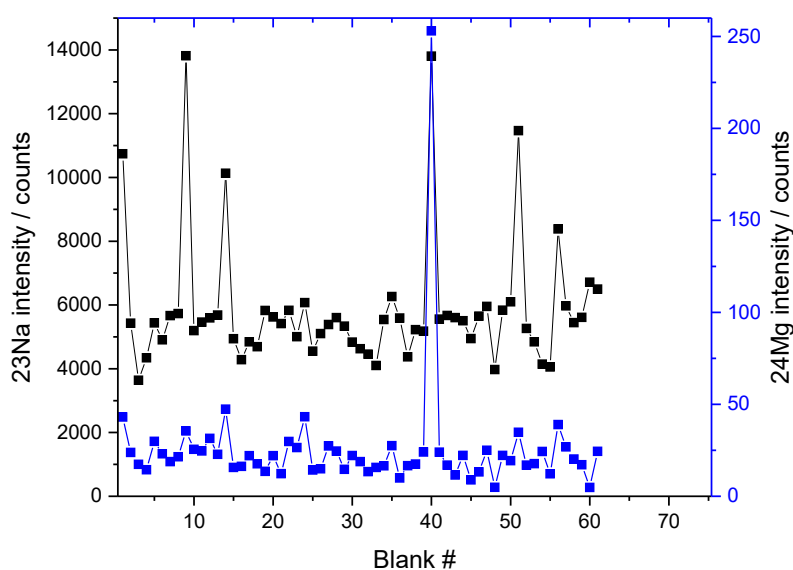


Figure 44 Comparison of Na and Mg blank intensities from different drop blanks.

Determination of limits of detection

Measured intensities of both, blank and cells, had low count numbers. For signals having low count numbers, the usually used approach to calculate LODs ($3 \times \text{SD}$) is not correct, as this approach assumes a normally distributed blank. Thus, the herein measured blank was tested for normality for all elements using the Lilliefors test ($\alpha=0.05$), and indeed for most elements a significant deviation from normality could be confirmed. ‘Counting experiments’ are known to show a Poisson distribution, which require a specific procedure to calculate the limits of detection.⁹⁷ Herein we used an approach derived by Currie, which is based on the simple calculation for a normally distributed blank, addressing the deviation from normality by the introduction of a constant ($\text{LOD} = 3.29 \times \text{SD} + 2.71$). This approximation for Poisson distributed blanks is also part of the IUPAC recommendations.⁸⁸

Potential mass interferences of detected isotopes

Several elements like Al, Ba, S, Ca, Sr, and As are not expected to be present in detectable amounts ($\sim \text{fg/cell}$ range) in cells. Mass interferences could be a potential source for several of

these elements. The mass resolving power of the used icpTOF (~ 3000) enabled the (partial) resolution of several major interferences. For ^{32}S , the $^{32}\text{O}_2$ interference was partially separated, see Figure 45, left. The signals which were assigned to the ^{32}S peak show as a distinguishable shoulder of the $^{32}\text{O}_2$ peak and are distinguishable elevated compared to the ablation of droplet blanks (dark lines). For ^{44}Ca , the major $^{44}\text{CO}_2$ interference was found to be almost baseline separated and to ^{56}Fe a distinguishable shoulder on the peak of its major interference ^{56}ArO could be assigned. While peaks of interferences remained relatively constant if blank and cell signals are compared, for all three elements a significant signal increase can be seen cells. This allowed for background correction and detection of the three isotopes ^{32}S , ^{44}Ca , and ^{56}Fe .

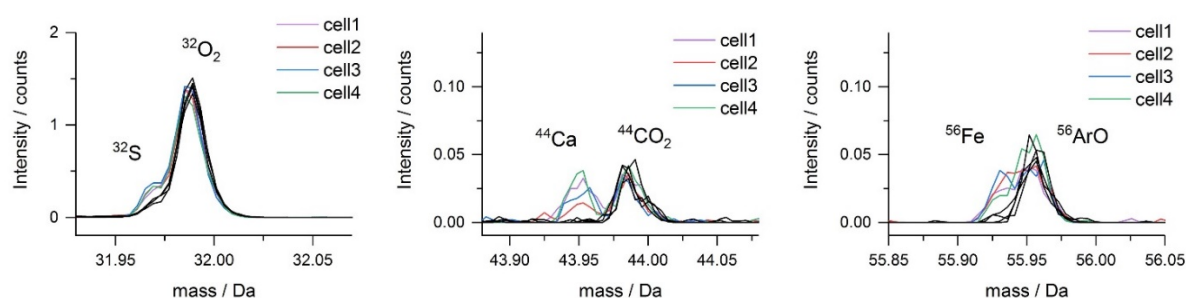


Figure 45 ICP-TOF-MS mass spectra of potentially interfered elements for the peak maxima of the four cells ablated in Figure 41 and for four peak maxima from ablating four randomly selected droplet blanks (dark lines). Intensities are average intensities of 1000 TOF extractions (equaling 30 ms integration time).

The main mass interference complicating the detection of ^{75}As is $^{75}\text{ArCl}$, which cannot be resolved with the used ICP-TOF-MS instrument. Cl naturally can be found as ^{35}Cl ($\sim 76\%$) and ^{37}Cl ($\sim 24\%$). Since $^{75}\text{ArCl}$ and $^{77}\text{ArCl}$ should be formed proportionally in the plasma, there should be an about three times decreased signal for $^{77}\text{ArCl}$ if compared to the signal observed at mass 75. As can be seen in Figure 46, this is not the case. Thus, signals on mass 75 were assigned to ^{75}As .

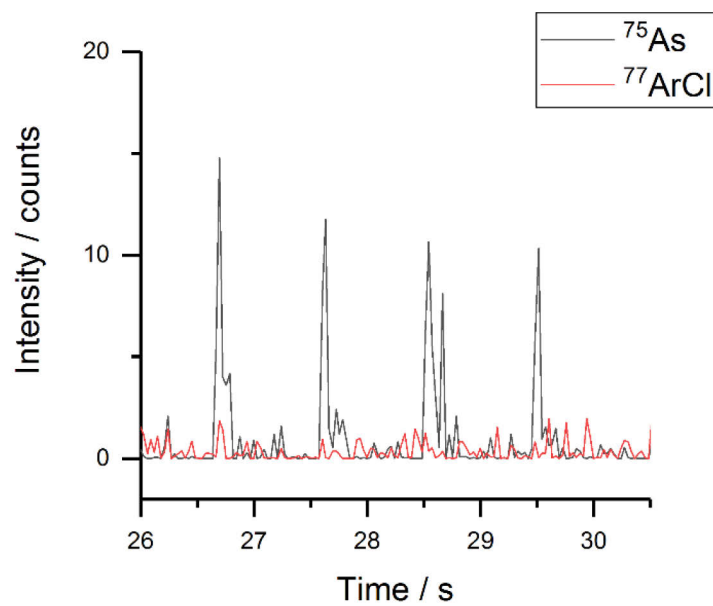


Figure 46 Time resolved signals from ablation of the same four cells as in Figure 41 on masses 75 Da and 77 Da.

7.3.2 Quantification of cell dyes

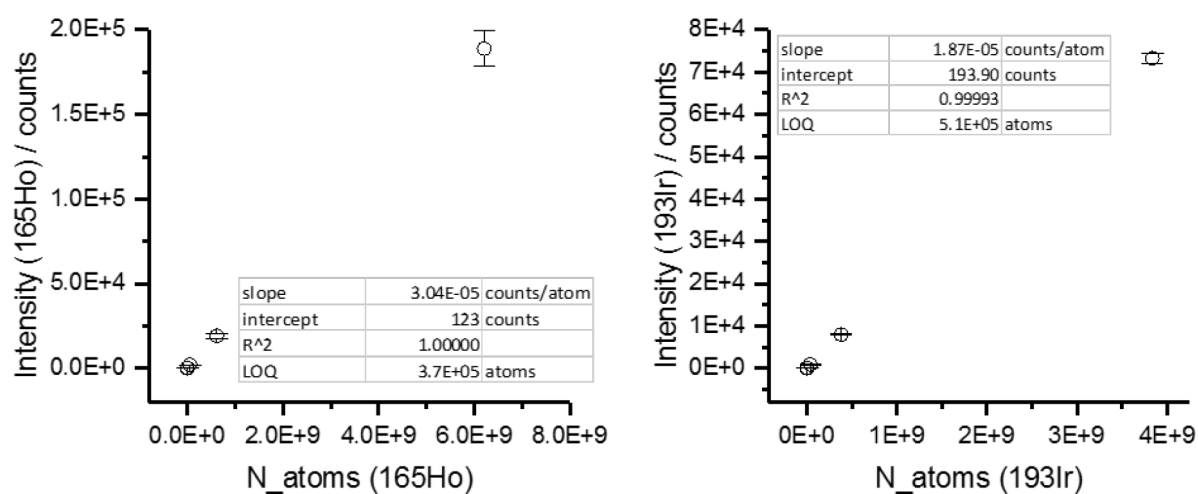


Figure 47 Fitting of calibration curves for matrix matched calibration of LA-ICP-TOF-MS single-cell measurements.

Table 16 Measured calibration data for ^{165}Ho .

N_{atoms}	Intensity counts	SD counts	RSD
$6.2\text{E+}09$	$1.9\text{E+}05$	$1.0\text{E+}04$	5.6%
$6.2\text{E+}08$	$1.9\text{E+}04$	$1.4\text{E+}03$	7.2%
$6.2\text{E+}07$	$2.0\text{E+}03$	$7.9\text{E+}01$	3.9%
$6.2\text{E+}06$	$2.4\text{E+}02$	43	18.4%
0E+00	2.5	1	44.5%

Table 17 Measured calibration data for ^{193}Ir .

$N_{\text{atoms_Ir}}$	$N_{\text{atoms_}^{193}\text{Ir}}$	Intensity counts	SD counts	RSD
$6.2\text{E+}09$	$3.8\text{E+}09$	$7.3\text{E+}04$	$1.2\text{E+}03$	1.7%
$6.2\text{E+}08$	$3.8\text{E+}08$	$8.0\text{E+}03$	$1.5\text{E+}02$	1.8%
$6.2\text{E+}07$	$3.8\text{E+}07$	$8.6\text{E+}02$	$3.5\text{E+}01$	4.1%
$6.2\text{E+}06$	$3.8\text{E+}06$	97.2	8.2	8.5%
0E+00	0.0E+00	1.5	1.0	63.2%

Literature

1. Engels, F. L. J. W.; Lottspeich, F. J. M., *Bioanalytik*. 2006; Vol. 979, p 995.
2. Basiji, D. A.; Ortyn, W. E.; Liang, L.; Venkatachalam, V.; Morrissey, P., Cellular image analysis and imaging by flow cytometry. *Clin. Chem. Lab. Med.* **2007**, 27 (3), 653-70, viii.
3. Brown, M.; Wittwer, C., Flow Cytometry: Principles and Clinical Applications in Hematology. *Clin. Chem.* **2000**, 46 (8), 1221-1229.
4. Roederer, M., Spectral compensation for flow cytometry: Visualization artifacts, limitations, and caveats. *Cytometry* **2001**, 45 (3), 194-205.
5. Baranov, V. I.; Quinn, Z.; Bandura, D. R.; Tanner, S. D., A sensitive and quantitative element-tagged immunoassay with ICPMS detection. *Anal. Chem.* **2002**, 74 (7), 1629-1636.
6. Waentig, L.; Roos, P. H.; Jakubowski, N., Labelling of antibodies and detection by laser ablation inductively coupled plasma mass spectrometry. *J. Anal. At. Spectrom.* **2009**, 24 (7), 924-933.
7. Mueller, L.; Traub, H.; Jakubowski, N.; Drescher, D.; Baranov, V. I.; Kneipp, J., Trends in single-cell analysis by use of ICP-MS. *Anal. Bioanal. Chem.* **2014**, 406 (27), 6963-6977.
8. Wang, H.; He, M.; Chen, B.; Hu, B., Advances in ICP-MS based techniques for trace elements and their species analysis in cells. *J. Anal. At. Spectrom.* **2017**, 32, 1650-1659.
9. Gilston, B. A.; O'Halloran, T. V., Metals in Cells: Control of Cellular Metal Concentration. *Encycl. Inorg. Bioinorg. Chem.* **2011**, 1-12.
10. Drescher, D.; Giesen, C.; Traub, H.; Panne, U.; Kneipp, J.; Jakubowski, N., Quantitative Imaging of Gold and Silver Nanoparticles in Single Eukaryotic Cells by Laser Ablation ICP-MS. *Anal. Chem.* **2012**, 84 (22), 9684-9688.
11. Managh, A. J.; Edwards, S. L.; Bushell, A.; Wood, K. J.; Geissler, E. K.; Hutchinson, J. A.; Hutchinson, R. W.; Reid, H. J.; Sharp, B. L., Single Cell Tracking of Gadolinium Labeled CD4(+) T Cells by Laser Ablation Inductively Coupled Plasma Mass Spectrometry. *Anal. Chem.* **2013**, 85 (22), 10627-10634.
12. Profrock, D.; Prange, A., Inductively Coupled Plasma-Mass Spectrometry (ICP-MS) for Quantitative Analysis in Environmental and Life Sciences: A Review of Challenges, Solutions, and Trends. *Appl. Spectrosc.* **2012**, 66 (8), 843-868.
13. Houk, R. S.; Fassel, V. A.; Flesch, G. D.; Svec, H. J.; Gray, A. L.; Taylor, C. E., Inductively Coupled Argon Plasma as an Ion-Source for Mass-Spectrometric Determination of Trace-Elements. *Anal. Chem.* **1980**, 52 (14), 2283-2289.
14. Montaser, A., *Inductively coupled plasma mass spectrometry*. John Wiley & Sons: 1998.

15. Thomas, R., *Practical guide to ICP-MS: a tutorial for beginners*. CRC press: 2013.
16. Sharp, B. L., Pneumatic Nebulizers and Spray Chambers for Inductively Coupled Plasma Spectrometry - a Review .2. Spray Chambers. *J. Anal. At. Spectrom.* **1988**, 3 (7), 939-963.
17. Sharp, B. L., Pneumatic Nebulizers and Spray Chambers for Inductively Coupled Plasma Spectrometry - a Review .1. Nebulizers. *J. Anal. At. Spectrom.* **1988**, 3 (5), 613-652.
18. Degueldre, C.; Favarger, P. Y., Colloid analysis by single particle inductively coupled plasma-mass spectroscopy: a feasibility study. *Colloids Surf., A* **2003**, 217 (1-3), 137-142.
19. Meermann, B.; Nischwitz, V., ICP-MS for the analysis at the nanoscale - a tutorial review. *J. Anal. At. Spectrom.* **2018**, 33 (9), 1432-1468.
20. Nomizu, T.; Kaneco, S.; Tanaka, T.; Ito, D.; Kawaguchi, H.; Vallee, B. T., Determination of Calcium Content in Individual Biological Cells by Inductively-Coupled Plasma-Atomic Emission-Spectrometry. *Anal. Chem.* **1994**, 66 (19), 3000-3004.
21. Ornatsky, O.; Bandura, D.; Baranov, V.; Nitz, M.; Winnik, M. A.; Tanner, S., Highly multiparametric analysis by mass cytometry. *J. Immunol. Methods* **2010**, 361 (1-2), 1-20.
22. Miyashita, S.; Groombridge, A. S.; Fujii, S.; Minoda, A.; Takatsu, A.; Hioki, A.; Chiba, K.; Inagaki, K., Highly efficient single-cell analysis of microbial cells by time-resolved inductively coupled plasma mass spectrometry. *J. Anal. At. Spectrom.* **2014**, 29 (9), 1598-1606.
23. Rodriguez, M. C.; Garcia, R. A. F.; Blanco, E.; Bettmer, J.; Montes-Bayon, M., Quantitative Evaluation of Cisplatin Uptake in Sensitive and Resistant Individual Cells by Single-Cell ICP-MS (SC-ICP-MS). *Anal. Chem.* **2017**, 89 (21), 11491-11497.
24. Amable, L.; Smith, S.; Stephan, C.; Shelton, C., New Research Evaluating Cisplatin Uptake in Ovarian Cancer Cells by Single Cell ICP-MS. *Perkin Elmer Application Note* **2017**.
25. Asperon™ Spray Chamber: Delivering “Intact Individual Cells” to the ICP-MS Plasma. *Perkin Elmer Technical Note* **2017**.
26. Verboket, P. E.; Borovinskaya, O.; Meyer, N.; Gunther, D.; Dittrich, P. S., A New Microfluidics-Based Droplet Dispenser for ICPMS. *Anal. Chem.* **2014**, 86 (12), 6012-6018.
27. Shigeta, K.; Koellensperger, G.; Rampler, E.; Traub, H.; Rottmann, L.; Panne, U.; Okino, A.; Jakubowski, N., Sample introduction of single selenized yeast cells (*Saccharomyces cerevisiae*) by micro droplet generation into an ICP-sector field mass spectrometer for label-free detection of trace elements. *J. Anal. At. Spectrom.* **2013**, 28 (5), 637-645.
28. Wang, H.; Chen, B. B.; He, M.; Hu, B., A Facile Droplet-Chip-Time-Resolved Inductively Coupled Plasma Mass Spectrometry Online System for Determination of Zinc in Single Cell. *Anal. Chem.* **2017**, 89 (9), 4931-4938.
29. Van Malderen, S. J. M.; Vergucht, E.; De Rijcke, M.; Janssen, C.; Vincze, L.; Vanhaecke, F., Quantitative Determination and Subcellular Imaging of Cu in Single Cells via

Laser Ablation-ICP-Mass Spectrometry Using High-Density Microarray Gelatin Standards. *Anal. Chem.* **2016**, 88 (11), 5783-5789.

30. Meyer, S.; Lopez-Serrano, A.; Mitze, H.; Jakubowski, N.; Schwerdtle, T., Single-cell analysis by ICP-MS/MS as a fast tool for cellular bioavailability studies of arsenite. *Metallomics* **2018**, 10 (1), 73-76.

31. Li, F. M.; Armstrong, D. W.; Houk, R. S., Behavior of bacteria in the inductively coupled plasma: Atomization and production of atomic ions for mass spectrometry. *Anal. Chem.* **2005**, 77 (5), 1407-1413.

32. Becker, J. S.; Matusch, A.; Wu, B., Bioimaging mass spectrometry of trace elements - recent advance and applications of LA-ICP-MS: A review. *Anal. Chim. Acta* **2014**, 835, 1-18.

33. Pozebon, D.; Scheffler, G. L.; Dressler, V. L.; Nunes, M. A. G., Review of the applications of laser ablation inductively coupled plasma mass spectrometry (LA-ICP-MS) to the analysis of biological samples. *J. Anal. At. Spectrom.* **2014**, 29 (12), 2204-2228.

34. Giesen, C.; Wang, H. A. O.; Schapiro, D.; Zivanovic, N.; Jacobs, A.; Hattendorf, B.; Schuffler, P. J.; Grolimund, D.; Buhmann, J. M.; Brandt, S.; Varga, Z.; Wild, P. J.; Gunther, D.; Bodenmiller, B., Highly multiplexed imaging of tumor tissues with subcellular resolution by mass cytometry. *Nat. Methods* **2014**, 11 (4), 417-422.

35. Perdian, D. C.; Bajic, S. J.; Baldwin, D. P.; Houk, R. S., Time-resolved studies of particle effects in laser ablation inductively coupled plasma-mass spectrometry. *J. Anal. At. Spectrom.* **2008**, 23 (3), 336-341.

36. Wang, H. A.; Grolimund, D.; Giesen, C.; Borca, C. N.; Shaw-Stewart, J. R.; Bodenmiller, B.; Günther, D., Fast chemical imaging at high spatial resolution by laser ablation inductively coupled plasma mass spectrometry. *Anal. Chem.* **2013**, 85 (21), 10107-10116.

37. Van Acker, T.; Van Malderen, S. J.; Van Heerden, M.; McDuffie, J. E.; Cuyckens, F.; Vanhaecke, F., High-resolution laser ablation-inductively coupled plasma-mass spectrometry imaging of cisplatin-induced nephrotoxic side effects. *Anal. Chim. Acta* **2016**, 945, 23-30.

38. ESI NWR-Image system for bio-imaging. <http://www.nwrlasers.com/laserablation/nwrimage/> (accessed 20.11.2017).

39. Chang, Q.; Ornatsky, O. I.; Siddiqui, I.; Loboda, A.; Baranov, V. I.; Hedley, D. W., Imaging Mass Cytometry. *Cytometry Part A* **2017**, 91A (2), 160-169.

40. Van Malderen, S. J.; Managh, A. J.; Sharp, B. L.; Vanhaecke, F., Recent developments in the design of rapid response cells for laser ablation-inductively coupled plasma-mass spectrometry and their impact on bioimaging applications. *J. Anal. At. Spectrom.* **2016**, 31 (2), 423-439.

41. Wang, M.; Zheng, L. N.; Wang, B.; Chen, H. Q.; Zhao, Y. L.; Chai, Z. F.; Reid, H. J.; Sharp, B. L.; Feng, W. Y., Quantitative Analysis of Gold Nanoparticles in Single Cells by Laser Ablation Inductively Coupled Plasma-Mass Spectrometry. *Anal. Chem.* **2014**, 86 (20), 10252-10256.

42. Zhai, J.; Wang, Y. L.; Xu, C.; Zheng, L. N.; Wang, M.; Feng, W. Y.; Gao, L.; Zhao, L. N.; Liu, R.; Gao, F. P.; Zhao, Y. L.; Chai, Z. F.; Gao, X. Y., Facile Approach To Observe and Quantify the $\alpha(\text{IIb})\beta(3)$ Integrin on a Single-Cell. *Anal. Chem.* **2015**, *87* (5), 2546-2549.
43. Hineman, A.; Stephan, C., Effect of dwell time on single particle inductively coupled plasma mass spectrometry data acquisition quality. *J. Anal. At. Spectrom.* **2014**, *29* (7), 1252-1257.
44. Bandura, D. R.; Baranov, V. I.; Ornatsky, O. I.; Antonov, A.; Kinach, R.; Lou, X.; Pavlov, S.; Vorobiev, S.; Dick, J. E.; Tanner, S. D., Mass cytometry: technique for real time single cell multitarget immunoassay based on inductively coupled plasma time-of-flight mass spectrometry. *Anal. Chem.* **2009**, *81* (16), 6813-6822.
45. Bendall, S. C.; Simonds, E. F.; Qiu, P.; El-ad, D. A.; Krutzik, P. O.; Finck, R.; Bruggner, R. V.; Melamed, R.; Trejo, A.; Ornatsky, O. I., Single-cell mass cytometry of differential immune and drug responses across a human hematopoietic continuum. *Science* **2011**, *332* (6030), 687-696.
46. Giesen, C.; Mairinger, T.; Khoury, L.; Waentig, L.; Jakubowski, N.; Panne, U., Multiplexed Immunohistochemical Detection of Tumor Markers in Breast Cancer Tissue Using Laser Ablation Inductively Coupled Plasma Mass Spectrometry. *Anal. Chem.* **2011**, *83* (21), 8177-8183.
47. Hendriks, L.; Gundlach-Graham, A.; Günther, D., Fundamental plasma investigation using microdroplets with ICP-TOFMS. *EWCPS Book of Abstracts* **2017**.
48. Armbrrecht, L.; Dittrich, P. S., Recent Advances in the Analysis of Single Cells. *Anal. Chem.* **2017**, *89* (1), 2-21.
49. Murphy, T. W.; Zhang, Q.; Naler, L. B.; Ma, S.; Lu, C., Recent advances in the use of microfluidic technologies for single cell analysis. *Analyst* **2018**, *143* (1), 60-80.
50. Urban, P. L.; Jefimovs, K.; Amantonico, A.; Fagerer, S. R.; Schmid, T.; Madler, S.; Puigmarti-Luis, J.; Goedecke, N.; Zenobi, R., High-density micro-arrays for mass spectrometry. *Lab Chip* **2010**, *10* (23), 3206-3209.
51. Ibanez, A. J.; Fagerer, S. R.; Schmidt, A. M.; Urban, P. L.; Jefimovs, K.; Geiger, P.; Dechant, R.; Heinemann, M.; Zenobi, R., Mass spectrometry-based metabolomics of single yeast cells. *Proc. Natl. Acad. Sci. U. S. A.* **2013**, *110* (22), 8790-8794.
52. Xie, W. Y.; Gao, D.; Jin, F.; Jiang, Y. Y.; Liu, H. X., Study of Phospholipids in Single Cells Using an Integrated Microfluidic Device Combined with Matrix-Assisted Laser Desorption/Ionization Mass Spectrometry. *Anal. Chem.* **2015**, *87* (14), 7052-7059.
53. Krismer, J.; Sobek, J.; Steinhoff, R. F.; Fagerer, S. R.; Pabst, M.; Zenobi, R., Screening of *Chlamydomonas reinhardtii* Populations with Single-Cell Resolution by Using a High-Throughput Microscale Sample Preparation for Matrix-Assisted Laser Desorption Ionization Mass Spectrometry. *Appl. Environ. Microbiol.* **2015**, *81* (16), 5546-5551.

54. Yang, T.; Gao, D.; Jin, F.; Jiang, Y. Y.; Liu, H. X., Surface-printed microdot array chips coupled with matrix-assisted laser desorption/ionization mass spectrometry for high-throughput single-cell patterning and phospholipid analysis. *Rapid Commun. Mass Spectrom.* **2016**, *30*, 73-79.
55. Huang, L.; Chen, Y.; Weng, L. T.; Leung, M.; Xing, X. X.; Fan, Z. Y.; Wu, H. K., Fast Single-Cell Patterning for Study of Drug-Induced Phenotypic Alterations of HeLa Cells Using Time-of-Flight Secondary Ion Mass Spectrometry. *Anal. Chem.* **2016**, *88* (24), 12196-12203.
56. Eyer, K.; Kuhn, P.; Hanke, C.; Dittrich, P. S., A microchamber array for single cell isolation and analysis of intracellular biomolecules. *Lab Chip* **2012**, *12* (4), 765-772.
57. Eyer, K.; Stratz, S.; Kuhn, P.; Kuster, S. K.; Dittrich, P. S., Implementing Enzyme-Linked Immunosorbent Assays on a Microfluidic Chip To Quantify Intracellular Molecules in Single Cells. *Anal. Chem.* **2013**, *85* (6), 3280-3287.
58. Stratz, S.; Eyer, K.; Kurth, F.; Dittrich, P. S., On-Chip Enzyme Quantification of Single Escherichia coli Bacteria by Immunoassay-based Analysis. *Anal. Chem.* **2014**, *86* (24), 12375-12381.
59. Stratz, S.; Verboket, P. E.; Hasler, K.; Dittrich, P. S., Cultivation and quantitative single-cell analysis of *Saccharomyces cerevisiae* on a multifunctional microfluidic device. *Electrophoresis* **2018**, *39* (3), 540-547.
60. Eyer, K.; Kuhn, P.; Stratz, S.; Dittrich, P. S., A Microfluidic Chip for the Versatile Chemical Analysis of Single Cells. *J. Visualized Exp.* **2013**, (80).
61. Rodushkin, I.; Axelsson, M. D.; Malinovsky, D.; Baxter, D. C., Analyte- and matrix-dependent elemental response variations in laser ablation inductively coupled plasma mass spectrometry Part 1. The roles of plasma and ion sampling conditions. *J. Anal. At. Spectrom.* **2002**, *17* (10), 1223-1230.
62. Zhang, S. D.; He, M. H.; Yin, Z. B.; Zhu, E. Y.; Hang, W.; Huang, B. L., Elemental fractionation and matrix effects in laser sampling based spectrometry. *J. Anal. At. Spectrom.* **2016**, *31* (2), 358-382.
63. Limbeck, A.; Galler, P.; Bonta, M.; Bauer, G.; Nischkauer, W.; Vanhaecke, F., Recent advances in quantitative LA-ICP-MS analysis: challenges and solutions in the life sciences and environmental chemistry. *Anal. Bioanal. Chem.* **2015**, *407* (22), 6593-6617.
64. Russo, R. E.; Mao, X.; Gonzalez, J. J.; Zorba, V.; Yoo, J., Laser ablation in analytical chemistry. *Anal. Chem.* **2013**, *85* (13), 6162-6177.
65. Herrmann, A. J.; Techritz, S.; Jakubowski, N.; Haase, A.; Luch, A.; Panne, U.; Mueller, L., A simple metal staining procedure for identification and visualization of single cells by LA-ICP-MS. *Analyst* **2017**, *142* (10), 1703-1710.

66. Mueller, L.; Herrmann, A. J.; Techritz, S.; Panne, U.; Jakubowski, N., Quantitative characterization of single cells by use of immunocytochemistry combined with multiplex LA-ICP-MS. *Anal. Bioanal. Chem.* **2017**, *409* (14), 3667-3676.
67. Latkoczy, C.; Gunther, D., Enhanced sensitivity in inductively coupled plasma sector field mass spectrometry for direct solid analysis using laser ablation (LA-ICP-SFMS). *J. Anal. At. Spectrom.* **2002**, *17* (10), 1264-1270.
68. Prohaska, T.; Irrgeher, J.; Zitek, A.; Jakubowski, N., *Sector Field Mass Spectrometry for Elemental and Isotopic Analysis*. Royal Society of Chemistry: 2014.
69. Darzynkiewicz, Z.; Juan, G.; Bedner, E., Determining cell cycle stages by flow cytometry. *Curr. Protoc. Cell Biol.* **2001**, 8.4. 1-8.4. 18.
70. Longerich, H. P.; Jackson, S. E.; Gunther, D., Laser ablation inductively coupled plasma mass spectrometric transient signal data acquisition and analyte concentration calculation. *J. Anal. At. Spectrom.* **1996**, *11* (9), 899-904.
71. van Elteren, J. T.; Selih, V. S.; Sala, M.; Van Malderen, S. J. M.; Vanhaecke, F., Imaging Artifacts in Continuous Scanning 2D LA-ICPMS Imaging Due to Nonsynchronization Issues. *Anal. Chem.* **2018**, *90* (4), 2896-2901.
72. Jochum, K. P.; Weis, U.; Stoll, B.; Kuzmin, D.; Yang, Q. C.; Raczek, I.; Jacob, D. E.; Stracke, A.; Birbaum, K.; Frick, D. A.; Gunther, D.; Enzweiler, J., Determination of Reference Values for NIST SRM 610-617 Glasses Following ISO Guidelines. *Geostand. Geoanal. Res.* **2011**, *35* (4), 397-429.
73. Hösl, S., Laserablation mit induktiv gekoppelter Plasma-Massenspektrometrie für die medizinische Diagnostik. **2017**.
74. http://www.menzel.de/Microscope_Slides.687.0.html?L=1 (accessed 2015-07-24).
75. Melin, J.; Quake, S. R., Microfluidic large-scale integration: The evolution of design rules for biological automation. *Annu. Rev. Biophys. Biomol. Struct.* **2007**, *36*, 213-231.
76. Arima, V.; Bianco, M.; Zacheo, A.; Zizzari, A.; Perrone, E.; Marra, L.; Rinaldi, R., Fluoropolymers coatings on polydimethylsiloxane for retarding swelling in toluene. *Thin Solid Films* **2012**, *520* (6), 2293-2300.
77. Sotebier, C. A.; Kutscher, D. J.; Rottmann, L.; Jakubowski, N.; Panne, U.; Bettmer, J., Combination of single particle ICP-QMS and isotope dilution analysis for the determination of size, particle number and number size distribution of silver nanoparticles. *J. Anal. At. Spectrom.* **2016**, *31* (10), 2045-2052.
78. Sotebier, C. A.; Weidner, S. M.; Jakubowski, N.; Panne, U.; Bettmer, J., Separation and quantification of silver nanoparticles and silver ions using reversed phase high performance liquid chromatography coupled to inductively coupled plasma mass spectrometry in combination with isotope dilution analysis. *J. Chromatogr. A* **2016**, *1468*, 102-108.

79. Ramkorun-Schmidt, B.; Pergantis, S. A.; Esteban-Fernandez, D.; Jakubowski, N.; Gunther, D., Investigation of a Combined Microdroplet Generator and Pneumatic Nebulization System for Quantitative Determination of Metal-Containing Nanoparticles Using ICPMS. *Anal. Chem.* **2015**, *87* (17), 8687-8694.
80. Wang, H. L.; Wang, M.; Wang, B.; Zheng, L. N.; Chen, H. Q.; Chai, Z. F.; Feng, W. Y., Interrogating the variation of element masses and distribution patterns in single cells using ICP-MS with a high efficiency cell introduction system. *Anal. Bioanal. Chem.* **2017**, *409* (5), 1415-1423.
81. <https://www.wur.nl/en/show/Single-Particle-Calculation-tool.htm> (accessed 31.01.2019).
82. Shigeta, K.; Traub, H.; Panne, U.; Okino, A.; Rottmann, L.; Jakubowski, N., Application of a micro-droplet generator for an ICP-sector field mass spectrometer - optimization and analytical characterization. *J. Anal. At. Spectrom.* **2013**, *28* (5), 646-656.
83. Ornatsky, O. I.; Lou, X.; Nitz, M.; Schafer, S.; Sheldrick, W. S.; Baranov, V. I.; Bandura, D. R.; Tanner, S. D., Study of cell antigens and intracellular DNA by identification of element-containing labels and metallointercalators using inductively coupled plasma mass spectrometry. *Anal. Chem.* **2008**, *80* (7), 2539-2547.
84. Bodenmiller, B.; Zunder, E. R.; Finck, R.; Chen, T. J.; Savig, E. S.; Bruggner, R. V.; Simonds, E. F.; Bendall, S. C.; Sachs, K.; Krutzik, P. O.; Nolan, G. P., Multiplexed mass cytometry profiling of cellular states perturbed by small-molecule regulators. *Nat. Biotechnol.* **2012**, *30* (9), 858-889.
85. Zhu, X. F.; Lever, S. Z., Formation kinetics and stability studies on the lanthanide complexes of 1,4,7,10-tetra-azacyclododecane-N,N',N'',N''' tetraacetic acid by capillary electrophoresis. *Electrophoresis* **2002**, *23* (9), 1348-1356.
86. Behbehani, G. K.; Thom, C.; Zunder, E. R.; Finck, R.; Gaudilliere, B.; Fragiadakis, G. K.; Fantl, W. J.; Nolan, G. P., Transient Partial Permeabilization with Saponin Enables Cellular Barcoding Prior to Surface Marker Staining. *Cytometry Part A* **2014**, *85a* (12), 1011-1019.
87. Zunder, E. R.; Finck, R.; Behbehani, G. K.; Amir, E. D.; Krishnaswamy, S.; Gonzalez, V. D.; Lorang, C. G.; Bjornson, Z.; Spitzer, M. H.; Bodenmiller, B.; Fantl, W. J.; Pe'er, D.; Nolan, G. P., Palladium-based mass tag cell barcoding with a doublet-filtering scheme and single-cell deconvolution algorithm. *Nat. Protoc.* **2015**, *10* (2), 316-333.
88. Currie, L. A., Nomenclature in evaluation of analytical methods including detection and quantification capabilities (IUPAC Recommendations 1995). *Anal. Chim. Acta* **1999**, *391* (2), 105-126.
89. Wang, H. L.; Wang, B.; Wang, M.; Zheng, L. N.; Chen, H. Q.; Chai, Z. F.; Zhao, Y. L.; Feng, W. Y., Time-resolved ICP-MS analysis of mineral element contents and distribution patterns in single cells. *Analyst* **2015**, *140* (2), 523-531.

90. Limpert, E.; Stahel, W. A.; Abbt, M., Log-normal distributions across the sciences: Keys and clues. *Bioscience* **2001**, *51* (5), 341-352.
91. Schulz, A. R.; Stanislawiak, S.; Baumgart, S.; Grutzkau, A.; Mei, H. E., Silver nanoparticles for the detection of cell surface antigens in mass cytometry. *Cytometry Part A* **2017**, *91a* (1), 25-33.
92. Behbehani, G. K.; Bendall, S. C.; Clutter, M. R.; Fantl, W. J.; Nolan, G. P., Single-cell mass cytometry adapted to measurements of the cell cycle. *Cytometry Part A* **2012**, *81A* (7), 552-566.
93. Darzynkiewicz, Z., Cycling into future: Mass cytometry for the cell-cycle analysis. *Cytometry Part A* **2012**, *81A* (7), 546-548.
94. Wang, Y. C.; Ma, L. N.; Wang, C. M.; Sheng, G. Y.; Feng, L.; Yin, C. Y., Autocrine motility factor receptor promotes the proliferation of human acute monocytic leukemia THP-1 cells. *Int. J. Mol. Med.* **2015**, *36* (3), 627-632.
95. Lau, W. Y.; Chun, K. H.; Chan, W. T., Correlation of single-cell ICP-MS intensity distributions for the study of heterogeneous cellular responses to environmental stresses. *J. Anal. At. Spectrom.* **2017**, *32* (4), 807-815.
96. Zhou, Y.; Li, H. Y.; Sun, H. Z., Cytotoxicity of arsenic trioxide in single leukemia cells by time-resolved ICP-MS together with lanthanide tags. *Chem. Commun.* **2017**, *53* (20), 2970-2973.
97. Currie, L. A., Nomenclature in Evaluation of Analytical Methods Including Detection and Quantification Capabilities (Iupac Recommendations 1995). *Pure Appl. Chem.* **1995**, *67* (10), 1699-1723.

Selbstständigkeitserklärung

„Ich erkläre, dass ich die Dissertation selbständig und nur unter Verwendung der von mir gemäß § 7 Abs. 3 der Promotionsordnung der Mathematisch-Naturwissenschaftlichen Fakultät, veröffentlicht im Amtlichen Mitteilungsblatt der Humboldt-Universität zu Berlin Nr. 17/2012 am 27.06.12 angegebenen Hilfsmittel angefertigt habe.“

Berlin, den 24.06.2019

Konrad Löhr

Scientific Contributions

Publications:

1. “Arraying of single cells for high throughput LA-ICP-TOF-MS”, Konrad Loehr, Olga Borovinskaya, Guilhem Tourniaire, Ulrich Panne, Norbert Jakubowski; submitted to *Anal. Chem.*
2. “Quantitative LA-ICP-MS of single cells: Comparison of single spot ablation and imaging”, Konrad Loehr, Antje Herrmann, Heike Traub, Ulrich Panne, Norbert Jakubowski; *J. Anal. At. Spectrom.*, no. 33 (2018), 1579-1587

Presentations:

1. “Towards quantitative high throughput single cell LA-ICP-TOF-MS”, Konrad Loehr, Olga Borovinskaya, Guilhem Tourniaire, Ulrich Panne, Norbert Jakubowski; Single Cell Proteomics 2019, 2019-06-11, Boston, Massachusetts, USA
2. “Towards single cell arraying for LA-ICP-MS”, Konrad Loehr, Olga Borovinskaya, Guilhem Tourniaire, Ulrich Panne, Norbert Jakubowski; DIAGNOSTICS 8.0, 2018-09-06, Berlin, Germany
3. “Towards quantitative high throughput single cell LA-ICP-MS: microarraying of single cells and calibration standards via piezo based non-contact dispensing”, Konrad Loehr, R. Wellhausen, U. Panne, N. Jakubowski; Metallomics, 2017-08-17, Vienna, Austria
4. “Quantitative LA-ICP-MS of single cells: Comparison of single spot ablation and imaging”, Konrad Loehr, Antje Herrmann, Norbert Jakubowski; EWCP2017, 2017-02-23, St. Anton, Austria

Acknowledgements

I am deeply thankful to my colleagues, cooperation partners and friends for their support, lab assistance, and our fruitful discussions throughout the years. The research I performed at BAM would not have been possible without you.

I would like to express my gratitude to my PhD supervisor Prof. Ulrich Panne for his ongoing support, Dr. Norbert Jakubowski and Prof. Petra Dittrich for giving me the possibility to work on this interesting subject, as well as Prof. Michael Linscheid for officiating as my second referee.

I would like to thank Andreas Schulz for his technical support at the LA-ICP-MS system and the construction of the manual pressure control system for microfluidic experiments, as well as the construction of the heating device for the HECIS for sc-ICP-MS; Wolfram Bremser for his support in statistical data evaluation; Kevin Bethke (HU Berlin, Rademann group) for the Au/Cu sputtered glass slides; Larissa Müller for providing cell samples and fruitful discussions; Heike Traub for introducing me to LA-ICP-MS and for thoroughly reviewing my writings; the Dittrich group for introducing me to single cell microfluidics (Simone Stratz, Pascal Verboket, Bernhard Sebastian, Dominik Haidas); Timm Schwaar for his support in all bead-related questions and MALDI assistance; Kristin Hoffmann for support in flow cytometry; Daniel Moldenhauer, Thomas Behnke and Ute Resch-Genger for the cooperation regarding the swelling of Eu-based dyes into polystyrene beads to produce a perspective matrix matched standard for LA single cell measurements; Kathrin Hoffmann for assistance in fluorescence microscopy; Sabine Flemig for excellent and enduring support in cell culturing and for MALDI assistance; the colleagues from Scienion AG and cellenion SAS for their support in applying their novel single cell arraying technology (Robert Wellhausen, Guido Bared, Illia Glavatskyi, Guilhem Tourniaire); Olga Borovinskaya from TOFWERK for the collaboration regarding the icpTOF measurements as well as for a few great days in Thun; my coffee and lunch group for the stimulating discussions (Lena Ascher, Zhengchao You, Nora Lemke, Carlos Abad Andrade, Jessica Saatz, Ioana Abbas); the German Initiative of Excellence and my graduate school SALSA (DFG GSC 1013) and Bundesanstalt für Materialforschung und -prüfung (BAM) for funding this project.

Finally, I would like to thank my girlfriend Nora for her endless support and accompanying me throughout this journey.